Development of AAV-mediated Gene Therapy for Autosomal Recessive Bestrophinopathy

Shaun Roger Wood
Merton College
Nuffield Laboratory of Ophthalmology
Nuffield Department of Clinical Neurosciences

Thesis submitted for the degree of
Doctor of Philosophy in Clinical Neurosciences

September 2017

Table of Contents

List of Abbreviations

AAV	Adeno-Associated Virus
ABCA4	ATP Binding Cassette Subfamily A Member 4
ADVIRC	Autosomal Dominant Vitreoretinochoroidopathy
AMD	Age-related Macular Degeneration
ARB	Autosomal Recessive Bestrophinopathy
AVMD	Adult-onset Vitelliform Macular Dystrophy
BEST1	Bestrophin-1
bFGF	Basic Fibroblast Growth Factor
BGH	Bovine Growth Hormone
BSA	Bovine Serum Albumin
BVMD	Best Vitelliform Macular Dystrophy
C57BL/6J	Wild-type mouse strain
CaCC	Calcium-activated Chloride Channel
CAG	Cytomegalovirus early enhancer and chicken β-actin promoter with rabbit β-globulin intron/exon
CBA	Chicken β-actin
CDS	Coding Sequence
CF	Cystic Fibrosis
CFH	Complement Factor H
CFTR	Cystic Fibrosis Transmembrane Regulator
ClC-2	Chloride Channel-2
CMR	Canine Multifocal Retinopathy
CMV	Cytomegalovirus
CNGA1/3	Cyclic Nucleotide Gated Channel Alpha 1/ Alpha 3
CNGB3	Cyclic Nucleotide Gated Channel Beta 3
CNTF	Ciliary Neurotrophic Factor
CNV	Choroidal Neovascularisation
CRB1	Crumbs 1
CRX	Cod-Rod Homeobox

DAPI	4,6-Diamidine-2-Phenylindoledihydochloride
DNA	Deoxyribonucleic Acid
dNTP	Deoxyribonucleoside Triphosphate
DMEM	Dulbecco's Modified Eagle Medium
EDTA	Ethylenediaminetetraacetic Acid
EGTA	Ethyleneglycoltetraacetic Acid
EOG	Electrooculogram
ERG	Electroretinogram
FA	Formic Acid
FBS	Fetal Bovine Serum
GAPDH	Glyceraldehyde 3-Phosphate Dehydrogenase
GFP	Green Fluorescent Protein
GPCR	G-protein Coupled Receptor
GNAT2	Guanine Nucleotide Binding Protein, Alpha Transducing Activity Polypeptide 2
HEK293	Human Embryonic Kidney 293 Cell Line
HEK293T	Human Embryonic Kidney 293 Cell Line with T Antigen
HEPES	N-(2-Hydroxyethyl)piperazine-N'-(2-ethanesulfonic acid)
HPLC	High Performance Liquid Chromatography
HRP	Horse Radish Peroxidase
HUGO	Human Genome Organisation
ICC	Immunocytochemistry
IHC	Immunohistochemistry
IL	Interleukin
INL	Inner Nuclear Layer
IP	Immunoprecipitation
IPM	Interphotoreceptor Matrix
iPSC	Induced Pluripotent Stem Cell
IRBP	Interphotoreceptor Retinoid-Binding Protein
IRD	Inherited Retinal Disorder
IRES	Internal Ribosome Entry Sequence

ITR	Inverted Terminal Repeat
LCA	Leber's Congential Amaurosis
LC MS/MS	Liquid Chromatography Tandem Mass Spectrometry
LEDGF	Lens Epithelium-Derived Growth Factor
LRAT	Lecithin-Retinol Acyltransferase
LV	Lentivirus
MCP	Monocyte Chemotactic Protein
MEM	Minimum Essential Media
MERTK	C-MER Proto-Oncogene Tyrosine Kinase
mRNA	Messenger Ribonucleic Acid
NRL	Neural Retina Leucine Zipper
OCT	Optical Coherence Tomography
OLM	Outer Limiting Membrane
OMIM	Online Mendelian Inheritance in Man
ONL	Outer Nuclear Layer
OPL	Outer Plexiform Layer
PBS	Phosphate Buffered Saline
PCR	Polymerase Chain Reaction
PDE6	Phosphodiesterase 6
PEDF	Pigment Epithelium-Derived Factor
PEI	Polyethylenimine
POS	Photoreceptor Outer Segments
PROM1	Prominin 1
PRPF	Pre-mRNA Processing Factor
PVDF	Polyvinylidene Difluoride
qPCR	Quantitative Polymerase Chain Reaction
rAAV	Recombinant Adeno-Associated Virus
RDH	Retinol Dehydrogenase
REP1	Rab-escort Protein 1
RGC	Retinal Ganglion Cell
RHO	Rhodopsin

RIPA	Radioimmunoprecipitation Assay
RLBP1	Retinaldehyde Binding Protein 1
RNA	Ribonucleic Acid
ROM1	Retinal Outer Segment Membrane Protein 1
RP	Retinitis Pigmentosa
RP2	Retinitis Pigmentosa 2
RPGR	Retinitis Pigmentosa GTPase Regulator
RPM	Revolutions/Minute
RPE	Retinal Pigment Epithelium
RPE65	Retinal Pigment Epithelium-Specific 65 kDa Protein
SDS-PAGE	Sodium Dodecyl Sulfate Polyacrylamide Gel Electrophoresis
SEM	Standard Error of the Mean
TAE	Tris-Acetate-Ethylenediaminetetraacetic Acid
TBS	Tris Buffered Saline
TCEP	Tris(2-carboxyethyl)phosphine
TIMP	Tissue Inhibitor of Matrixmetalloprotease Protease
TOPORS	Topoisomerase I Binding, Arginine/Serine-Rich
UHPLC	Ultra-high performance liquid chromatography
USH2A	Usherin
VA	Visual Acuity
VMD2	Vitelliform Macular Dystrophy Type 2
VRAC	Volume Regulated Anion Channel
WB	Western Blot
WPRE	Woodchuck Hepatitis Virus Post-transcriptional Regulatory Element

List of Figures

List of Tables

Declaration of Authorship

The work contained in this thesis has not previously been submitted for a degree or diploma at the University of Oxford or any other higher education institution. All figures or tables reproduced or adapted from journal articles and other sources are referenced in the text. The contents of this thesis are all my own work, with the exception of the material described below:

1. The LC-MS/MS analysis was done by Dr Monika Stegmann at the Department of Biochemistry, University of Oxford.

Page Count = 189

Word Count = 34,920

Acknowledgements

First of all I want to thank my supervisor, Professor Robert MacLaren, for giving me the opportunity to study for a DPhil in his laboratory and providing me with guidance and support throughout this adventure. I would like to thank Dr Michelle McClements for her guidance in the laboratory and her endless patience and Drs Alun Barnard and Maria Patricio for their help and advice. Thanks must also go to my co-supervisor, Dr Forbes Manson for his help and advice and for allowing me to use his facilities for the completion of the patch-clamping experiments detailed in this thesis. To the past and present members of the MacLaren research group (in no particular order, Professor Dominik Fischer, Dr Daniyar Dauletbekov, Dr Doron Hickey, Dr Mark Hassall, Dr Jasmin Balmer, Dr Harry Orlans, Dr Cristina Martinez, Miss Caroline Peddle, Miss Laurel Chandler, Dr Alona Cramer, Dr Mandeep Singh, Ms Jasleen Jolly, Dr Thomas Edwards, Dr Kanmin Xue, Dr Matthew Simunovic, Dr Paola Salvetti, Dr Anna Buchberger and Dr Marco Bellini) and the Manson research group at the University of Manchester (Dr Carolina Uggenti and Dr Jingshu Liu) I thank them for their help, support, friendship and shared love of coffee. I'd also like to thank Dr Sumathi Sekaran for allowing me to use her equipment and Dr Alexandre Mathy for showing me how to operate it. Thanks to Dr Steven Hughes for always taking the time to answer questions. Thanks to the proteomics facility, in particular Dr Monika Steggman, for their assistance and Professor Richard Baines (University of Manchester) for allowing use of his facilities. Thanks to Fight for Sight, UK for funding this research. My family deserve special mention as without their support, this work would never have been completed. Thanks to my Mum for constant support and occasional nagging (which was crucial to the completion of my work), my Dad for his support and shared love of rugby and to my Grandpa, without whom I would never have been able to enrol on the Master's programme that preceded my DPhil. My sister, Laura, deserves thanks, though I highly doubt she'll ever read this. Finally I must thank my partner Miss Eleanor Quinn. Without her undying love and support I would have crumbled a long time ago and she will never know just how important she has been and will continue to be to me, particularly as we set out on the new adventure of parenthood.

Dedication

This thesis is dedicated to all the people who are responsible for me being where I am today but who are no longer here to see the results of their labour. Nanna, Grandad, Nanna Enid, Uncle David and Nanna Lily, you are gone but not forgotten.

Yours,

Shaun Roger Wood

Abstract

The bestrophinopathies are a set of inherited retinal degenerations caused by mutations in *BEST1*, and include Best vitelliform macular dystrophy (BVMD), autosomal dominant vitreoretinochoroidopathy (ADVIRC) and autosomal recessive bestrophinopathy (ARB). The corresponding protein, bestrophin-1, is localised to the basolateral membrane of the retinal pigment epithelium (RPE), where it is thought to function as a Ca^{2+}-activated Cl^- channel. Currently, there are no treatments for these conditions. In recent years, gene therapy has emerged as an exciting treatment option for inherited retinal disorders (IRDs). Gene delivery to retinal cells using a recombinant adeno-associated virus (rAAV) has produced positive results in several IRDs. Given the recessive nature of ARB, this thesis proposes that the rAAV-mediated delivery of bestrophin-1 to the RPE could represent a potential therapy. The aims of this thesis were to produce and compare rAAV vectors *in vitro* and *in vivo* for protein expression, localisation following transduction, restoration of chloride conductance *in vitro* and safety following sub-retinal injection *in vivo*. Following the production of two rAAV vectors expressing bestrophin-1, western blots confirmed bestrophin-1 protein expression following transduction of HEK293 cells *in vitro*. Immunocytochemistry (ICC) revealed bestrophin-1 expression that was localised to the cytosol. Whole-cell patch-clamping revealed a significant increase in chloride conductance in HEK293 cells transduced with AAV-BEST1 vectors which was then ablated upon the removal of chloride from the buffers. Liquid Chromatography Tandem Mass Spectrometry (LC-MS/MS) indicated that the bestrophin-1 protein was successfully transcribed and translated from the BEST1 coding sequence (CDS). Sub-retinal injections of AAV-BEST1 produced bestrophin-1 expression in the RPE of wild-type C57BL/6 mice however significant retinal thinning was seen at higher doses of vector. In conclusion, rAAV-mediated transfer of bestrophin-1 to the RPE has potential to be a future therapy for ARB, however safety issues need to be addressed and an RPE-specific promoter could be more suitable.

Chapter 1. General Introduction

1.1 The Human Eye

Sight is one of the fundamental senses that allow human beings to perceive their environment, and it is the human eye that allows the conversion of light into chemical signals that can then be transmitted to the human brain. The gross anatomy of the eye is depicted in figure 1. The eye is made up of 3 layers: the external layer (the sclera and cornea), the intermediate layer (containing iris and choroid) and the internal layer (containing the retina). The internal area of the eye can be further divided into 3 chambers: the anterior chamber (located between the cornea and the iris), the posterior chamber (located between the iris and the lens) and the vitreous chamber (located between the lens and the retina) (*1*).

Light enters the eye through the cornea, a transparent tissue consisting of an outer corneal epithelium, Bowman's layer, the corneal stroma, Descemet's membrane and the corneal endothelium (*2*). The cornea's highly regular structure allows it to direct light through the pupil. The light then passes through the iris and lens which, together with the cornea, refract and focus the light onto the retina. The aqueous humour provides nutrients to the iris and cornea (two areas of the eye with limited blood supply) and is secreted from the ciliary body, a continuation of the choroid located between the retina and iris. The ciliary body also contains the muscles that focus the lens (*2*). The vitreous chamber contains the vitreous humour, which is more viscous than the aqueous humour that fills the anterior and posterior chambers. The vitreous humour is involved in protecting the eye from trauma and excluding 'floaters' from the eye to maintain transparency (*3*). It's >98% water and contains unbranched collagen fibrils and

glycosaminoglycans, in particular hyaluronan. The vitreous provides an important scaffold to support the blood vessels that supply the lens during development (tunica vasculosa lentis) but has little if any known role in the adult eye, despite changing composition throughout adult life (*4*).

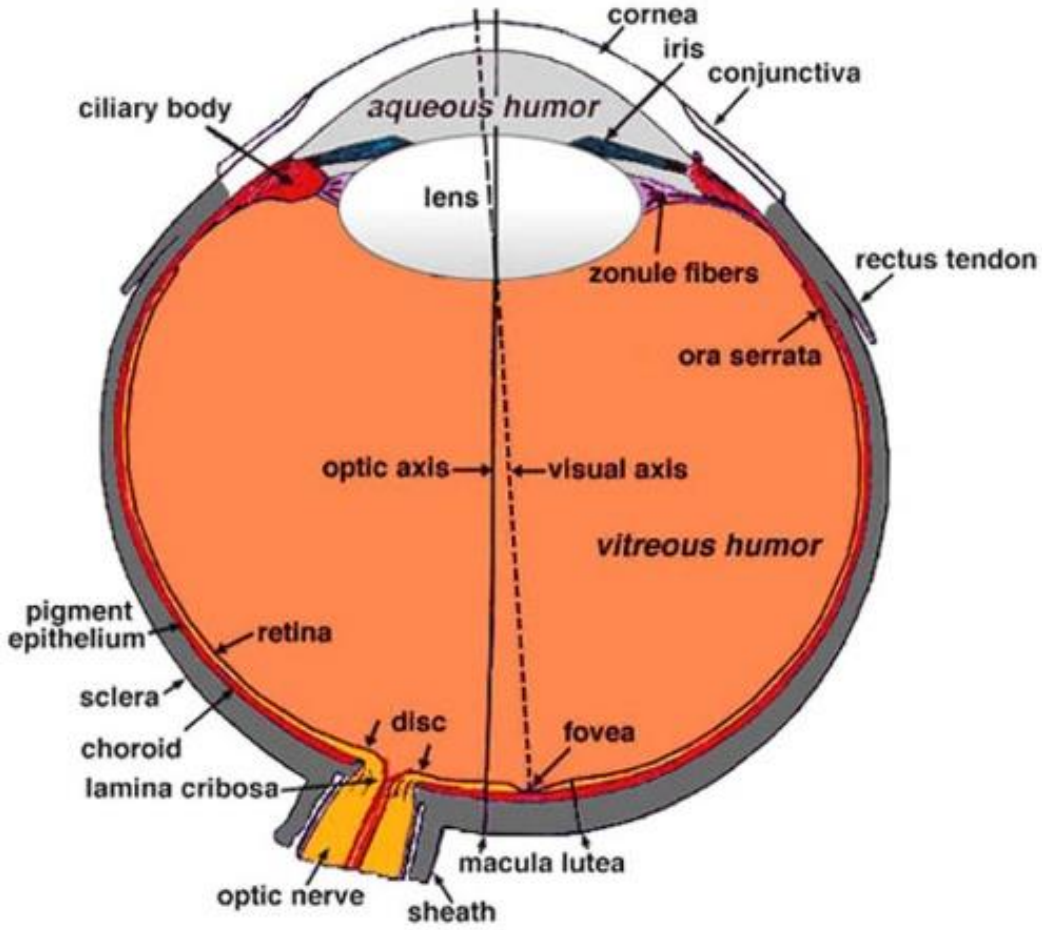

Figure 1.1. The Gross Anatomy of the Eye. Image taken from Kolb et al, 1995 (*1*)

1.2 The Retina

The retina is a multi-layered neurosensory tissue present at the back of the eye and is depicted in figure 2. Light passes through a transparent layer containing the inner limiting membrane, nerve fibre layer, retinal ganglion cells (RGCs), amacrine cells, bipolar cells and horizontal cells. The light is detected by the rod and cone photoreceptors in the outer nuclear layer (ONL) and converted into an electro-chemical signal that can be detected by the brain. Photo-pigments found in the photoreceptor outer segments (POS), consisting of a G protein-coupled receptor (GPCR) called an opsin and a chromophore called 11-cis-retinal, are responsible for this conversion, through a process known as the visual cycle (*5*) and is explained in more detail in section 1.3.1.

The thick, central area of the retina, known as the macula, is cone dense. Cone photoreceptors are responsible for colour vision and in humans and Old World primates contain 3 types of opsin which allow detection of a broad range of light wavelengths. The 'L-cones' contain L-opsin, a cone photo-pigment that detects longer wavelengths of light and has an absorption maxima of ~560 nm. The so-called 'M-cones' contain M-opsin, which has an absorption maxima of ~530 nm and the 'S-cones' contain S-opsin, with an absorption maxima of -425 nm (*6*). The peripheral retina contains a higher proportion of rod photoreceptors, which contain a single opsin called 'rhodopsin'. Rhodopsin has a absorption maxima at ~500 nm and is responsible for low-light vision (*6*). In conditions such as retinitis pigmentosa (RP), degeneration of the rods causes loss

of peripheral vision whilst leaving an ‘island’ of central vision until the very late stages, when the central cones also degenerate (*7*).

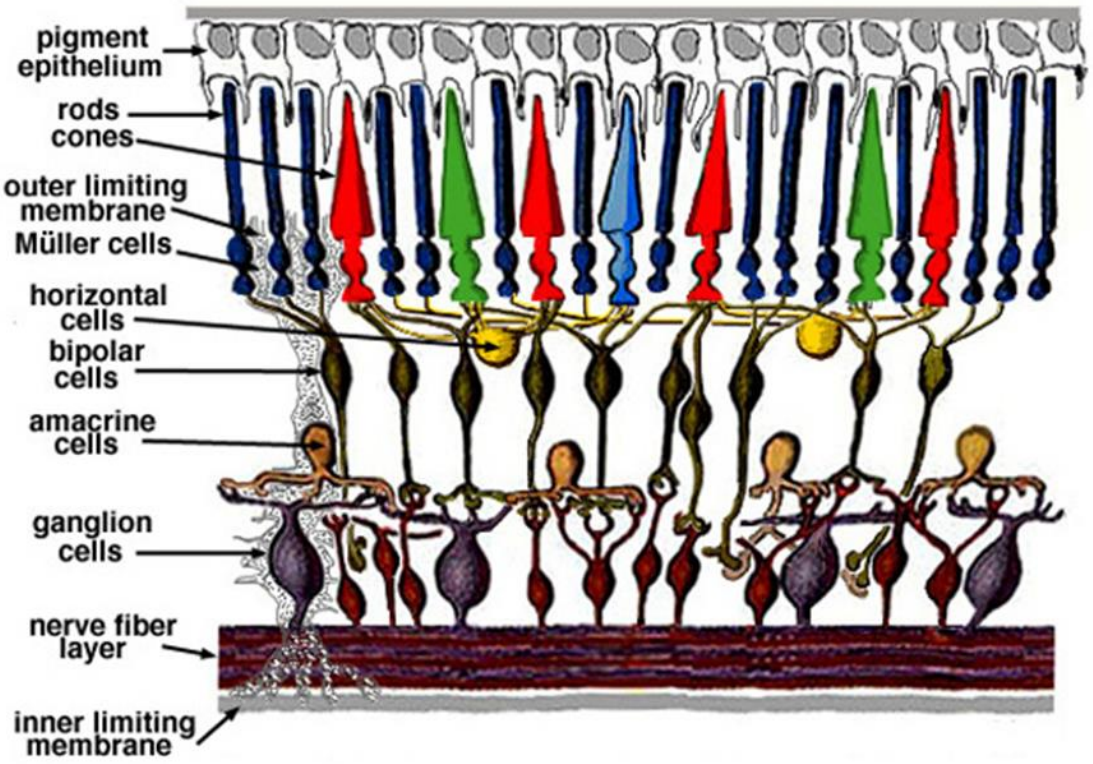

Figure 1.2. The Gross Anatomy of the Retina. Image taken from Kolb et al, 1995.

1.3 The Retinal Pigment Epithelium

The retinal pigment epithelium (RPE) is a cuboidal layer of cells that sits behind, and supports, the retina. The RPE plays a pivotal role in the visual cycle, converting all-trans retinol into 11-cis-retinal. The RPE is also involved in a number of other important retinal processes, which are summarised below and in figure 1.3.

1.3.1 The Visual Cycle

The visual cycle is initiated in the photoreceptors. Upon absorption of a photon of light 11-cis-retinal is isomerised to all-trans-retinal, which is released from the opsin and transported to the cytosolic face of the membrane discs by ATP Binding Cassette Subfamily A Member 4 (ABCA4). All-trans-retinal is reduced by all-trans-retinol dehydrogenase (RDH) to all-trans-retinol and is then transported out of the photoreceptors and into the RPE by interphotoreceptor retinoid-binding protein (IRBP). In the RPE, an enzyme cascade converts all-trans-retinol back into 11-cis-retinal. Firstly, all-trans-retinol is esterified by lecithin-retinol acyltransferase (LRAT) and is then converted into 11-cis-retinol by retinal pigment epithelium-specific 65 kDa protein (RPE65). Other RDH enzymes convert 11-cis-retinol into 11-cis retinal, which is then transported back into the photoreceptors where it re-associates with an opsin molecule.

1.3.2 Phagocytosis of Photoreceptor Outer Segments

As mentioned in chapter 1.2, the photoreceptor outer segments (POS) house the photopigments responsible for the detection of light. In order to maximise the surface area of cell membrane containing photosensitive pigments, the outer segments comprise of hundreds of stacked discs per cell. This arrangement makes it virtually impossible to maintain cell membrane homeostasis via the normal mechanisms of endocytosis and recycling and instead the discs are shed and phagocytosed by the RPE (*8*). Three receptors, present on the apical surface of the RPE, are required for the recognition and phagocytosis of POS. $\alpha_v\beta_5$ integrin is required for the recognition and binding of the POS, CD36 is required for the internalisation of POS and MERTK is required for the activation of phagocytosis (*9-12*). Mutations in genes that code for these proteins lead to the inhibition of POS phagocytosis and have been shown to be a cause of retinitis pigmentosa (*13, 14*) and choroidal degeneration (*15*).

1.3.3 Secretion

The RPE secretes a number of factors from both its apical and basal surfaces. At the apical surface it secrets neurotrophic factors such as pigment epithelium-derived factor (PEDF), basic fibroblast growth factor (bFGF) and ciliary neurotrophic factor (CNTF), which are released in response to damage to the retina and have been shown to have a neuroprotective effect on the retina and, in the case of PEDF, inhibit apoptosis (*16-18*). Vascular endothelium growth factor (VEGF) is secreted, at low levels, from the basal surface of the RPE and supports the growth and maintenance of the choriocapillaris

(*19*). Other factors secreted from the RPE include: tissue inhibitor of matrix metalloproteases (TIMP-1 and TIMP-3) (*20*) and other growth factors such as lens epithelium-derived growth factor (LEDGF) (*21*). The RPE also secretes interleukin-8 (IL-8), complement factor H (CFH) and monocyte chemotactic protein-1 (MCP-1) (*22-24*), allowing it to regulate the immune response and maintain the immune privilege of the eye.

1.3.4 Transepithelial Transport

The RPE forms a polarised epithelial sheet, connected by tight junctions, that is responsible for the transport of ions from the blood supply in the choriocapillaris to the retina and vice versa (*25*). The RPE takes up glucose from both the sub-retinal space and the choriocapillaris via GLUT1 and GLUT3 transporters (*26*). From the basal surface it can take up fatty acids for use in the recycling of POS (*27*) and all-trans-retinol for use in the visual cycle (*28*). Water build-up in the sub-retinal space can be caused by the high metabolic turnover of the retina and is further magnified by the intraocular pressure which can move water from the vitreous body into the retina (*29*). Removal of the excess water is a function of the RPE and is achieved by the transport of Cl^- that causes the movement of water from the sub-retinal space to the choriocapillaris. Transport of cations from the sub-retinal space into the RPE is carried out by Na^+/K^+ ATPase transporters present in the apical membrane of the RPE (*30*). These transporters exchange $3Na^+$ (inward) for $2K^+$ (outward) and cause an accumulation of positive charge which facilitates Cl^- uptake from the sub-retinal space via $Na^+/K^+/2Cl^-$ co-

transporters (*31*). Recycling of Na^+ through the Na^+/K^+ ATPase transporters leads to an accumulation of Cl^- in the RPE which is eliminated by transport through the basolateral membrane to the blood. This transport is driven by several anion channels present in the basolateral membrane, Cl- channel-2 (ClC-2) (*32*), the cystic fibrosis transmembrane regulator (CFTR) (*33*) and the Ca^{2+}-activated Cl^- channel known as bestrophin-1 (BEST1) (*34*). The movement of ions across the RPE is summarised in figure 1.4 (*35*).

1.3.5 Spatial Buffering of Ions

Normal transepithelial transport of ions is not enough to compensate for the changes in the composition of the sub-retinal space due to photoreceptor and second-order neuron activity (*36*). For example, the RPE expresses inwardly rectifying K^+ channels, at the apical membrane, which can compensate for changes in K^+ levels in the sub-retinal space following light-induced uptake of K^+ into the inner segments (*36, 37*). Light-induced changes in the neural retina also lead to sudden, transient increases in the movement of water across the sub-retinal space (*38*). Along with the transport mechanisms described in 1.3.3, the RPE is able to compensate for these sudden changes. Hyperpolarisation of the apical membrane, causing an increase in intracellular acidity, leads to increased Cl^- transport at the basolateral membrane, via a HCO_3^-/Cl^- exchanger (*39*). The movement of ions across the RPE is summarised in figure 1.4.

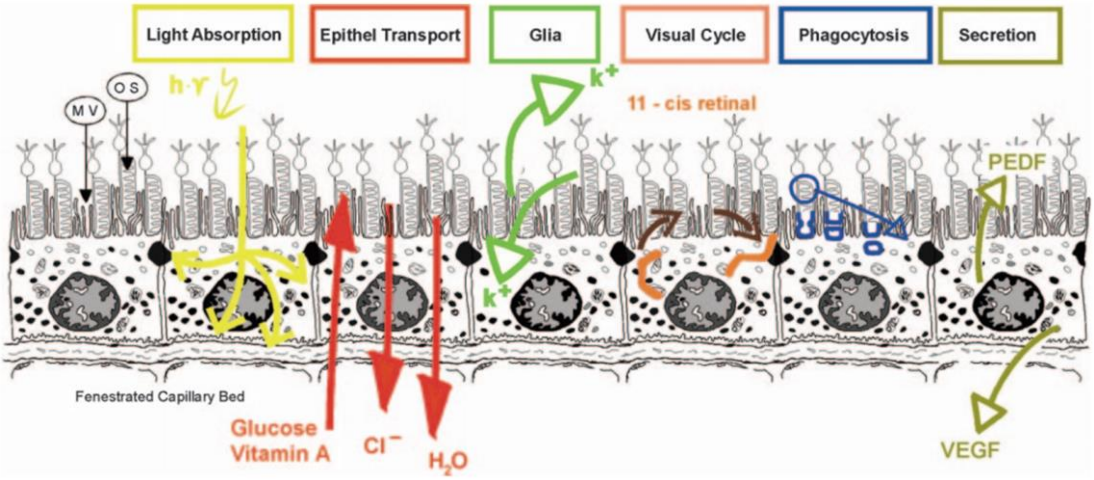

Figure 1.3. The Functions of the Retinal Pigment Epithelium. The RPE is essential for maintaining the health and homeostasis of the retina. At its apical side it takes in all-trans-retinol from the visual cycle, transports 11-cis-retinal back to the photoreceptors, exchanges K^+ for Na^+, secretes growth factors and absorbs light. At its basal side it takes in glucose and vitamin A, transports Cl^- out and secretes growth factors such as VEGF. Figure is taken from Strauss, 2005.

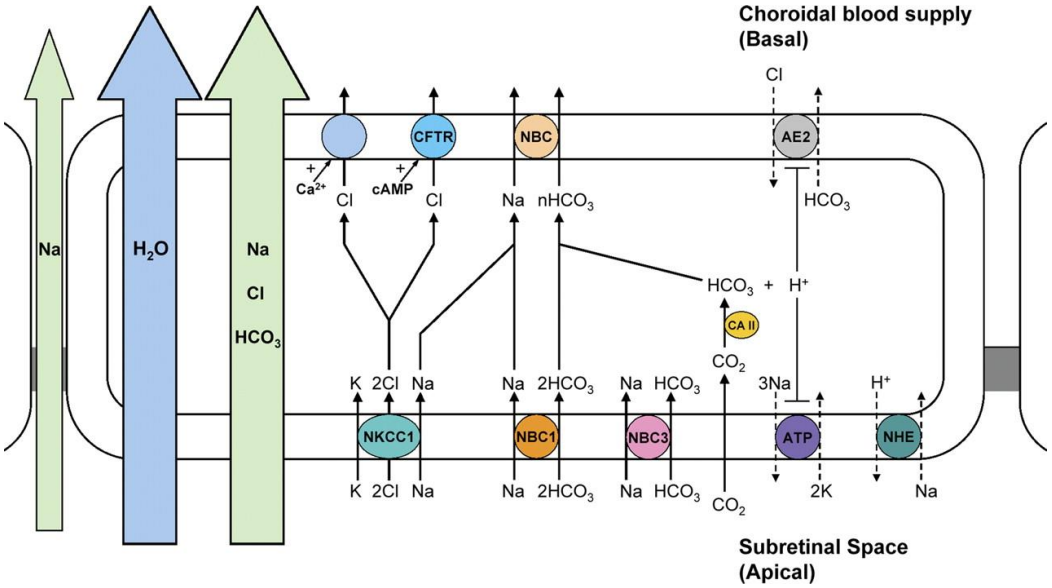

Figure 1.4. Ion Movement Across the RPE. Apical membrane transporters include Na/K ATPase, Na/K/2Cl cotransporter (NKCC1), Na/H exchanger (NHE), and Na/2HCO3 cotransporter (NBC1) and transport ions to and from the sub-retinal space. Basolateral membrane transporters include Ca2+-activated Cl channels (Bestrophin-1), cAMP-sensitive CFTR, Cl/HCO3 exchanger (AE2), and Na/nHCO3 cotransporter (NBC) and transport ions to and from the choriocapillaris. This transport influences movement of ions and water across the RPE and retina. This figure was taken from Adijanto et al, 2009.

1.4 Inherited Retinal Diseases (IRDs)

Inherited retinal diseases (IRDs) are predominantly caused by mutations in retinal-specific genes, of which more than 200 have been identified (*40*). At the time of writing, more than 200 IRD causative genes have been identified (*41*). The majority of mutations are found in genes expressed in the photoreceptors (e.g. RHO, RPGR and ABCA4) or the RPE (e.g. BEST1, RPE65 and MERTK) (*42*). Some IRDs are caused by mutations in single genes (e.g. Best vitelliform macular dystrophy), whereas others can be caused by mutations in multiple genes (e.g. retinitis pigmentosa [RP]). Excluding age-related macular degeneration (AMD), RP is the most common form of inherited retinal degeneration and can be caused by mutations in genes present in either the photoreceptors or the RPE (*43*). RP causes primary loss of rod photoreceptors and, therefore, leads to degeneration of the peripheral retina. Mutations in over 120 genes have been associated with RP, ranging from proteins important in phototransduction (e.g. *RHO*, *PDE6A*, *PDE6B*, *PDE6G* and *CNGA1*), retinal metabolism (e.g. *RPE65*, *LRAT* and *RLBP1*), retinal development (*NRL*, *CRX*, *CRB1* and *RP2*), splicing (e.g. *PRPF3/4/6/8/31*), maintenance of cellular structure (e.g. *USH2A*, *ROM1* and *PROM1*), POS phagocytosis (e.g. *MERTK*), intraflagellar transport (*RPGR*) and ubiquitination (*TOPORS*) (*44*).

Where RP causes degeneration of the peripheral retina, many other IRDs cause death of cone photoreceptors and hence the degeneration of the cone-dense macula, resulting in the loss of colour perception and visual acuity. These are commonly known as macular dystrophies. Achromatopsia is an example of a cone dystrophy that can be caused by

mutations in a number of different genes, many of which encode subunits of important components in the phototransduction cascade and visual cycle. *CNGA3* and *CNGB3* encode subunits of cGMP-gated channels, located in the cone photoreceptors. *GNAT2* encodes a subunit of a cone photopigment called transducin. *PDE6C* and *PDE6H* encode subunits of proteins involved in the conversion of cGMP to 5'-GMP in the visual cycle *(44).*

Single-gene IRDs include Stargardt's macular dystrophy, a juvenile onset disorder caused by mutations in *ABCA4*. The ABCA4 protein is involved in the trafficking of all-trans-retinal out of the POS and into the RPE. This leads to a build-up of lipofuscin and a severe, progressive macular dystrophy. Other single-gene IRDs include Leber congenital amaurosis (Type 2 = *RPE65*) and Best vitelliform macular dystrophy (*BEST1*).

IRDs represent a clinically and genetically heterogenous group of diseases with a range of presentations and inheritance patterns. As such, very few therapies exist for patients suffering from these conditions.

1.5 The Bestrophinopathies

1.5.1 Clinical Features of the Bestrophinopathies

Best disease was first described in 1905 by a German ophthalmologist, Freidrich Best. In 1998 the gene responsible (originally named *VMD2*) was mapped to the long arm of chromosome 11 (11q12) and was found to span ~15 kDa of DNA including 10 exonic regions (*45, 46*). *VMD2* has since been renamed as *BEST1* by the HUGO nomenclature committee. To date, over 200 mutations have been described in the *BEST1* gene, leading to a class of ocular phenotypes called 'bestrophinopathies' (*47*). These conditions present with phenotypes that vary in inheritance pattern, severity and clinical presentation.

Best vitelliform macular dystrophy (BVMD; OMIM no.153700) was the first of the bestrophinopathies to be described. Reported symptoms can vary however the condition is often characterised by autosomal dominant inheritance, juvenile onset, a yellowing ('egg-yolk') appearance of the macula and an abnormal light-peak in the electro-oculogram (EOG) (*47*). The ratio of 'light-peak' to 'dark trough' in the EOG (also known as the Arden Ratio) is often <1.5 in BVMD patients, as opposed to >2.0 in healthy individuals. Despite the changes in the EOG, the full-field ERG is often normal. The condition passes through several distinct stages of progression. The 'pre-vitelliform' stage is characterised by an abnormal EOG response with little to no changes in the appearance of the macula on the ophthalmoscope. This is followed by a

‘vitelliform’ stage, where a macular lesion can be seen on the ophthalmoscope and the yellow material known as ‘Lipofuscin’, a waste product of the phagocytosis of photoreceptor outer segments, can be seen in the RPE. This is often referred to as an ‘egg-yolk’ lesion. Following this is the ‘vitelliruptive’ stage (sometimes referred to as the ‘scrambled egg’ stage), where the lipofuscin starts to break up. This leaves a lesion with a ‘scrambled’ appearance. In the ‘pseudohypopyon’ stage, lipofuscin gathers in the inferior half of the macular lesion, leaving a distinct layer of clear liquid at the superior half. The ‘atrophic’ stage is characterised by choroidal atrophy and the final stage is the ‘neovascular’ stage, characterised by choroidal neovascularisation (CNV). This progression is depicted in figure 1.5. It is important to note that, allow this is the common progression, these stages can sometimes present in a different order (*47*). There have also been reports of patients presenting with different stages of the disease in each eye (*48*).

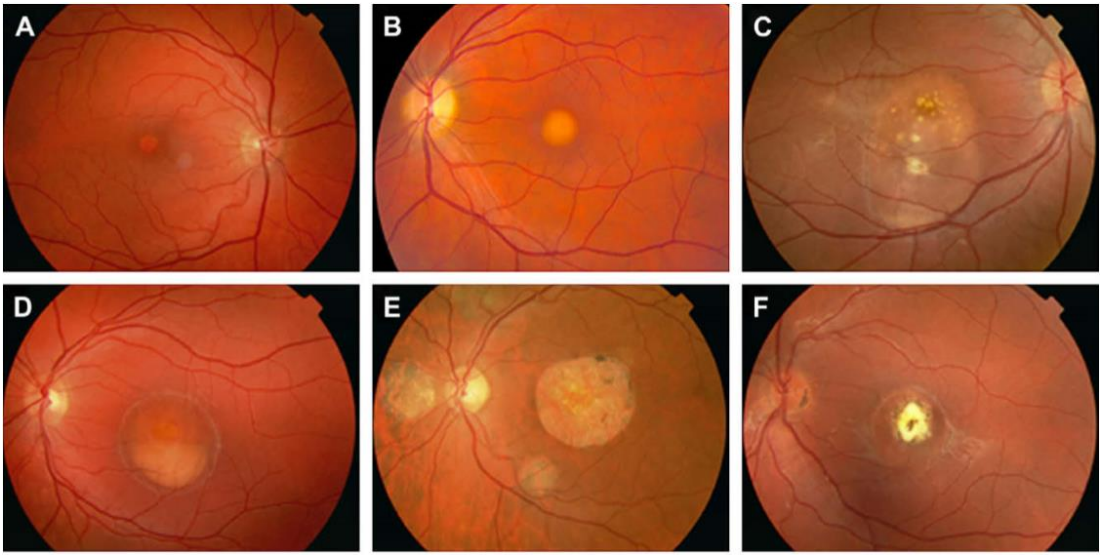

Figure 1.5. The Different Stages of Best Disease. '**A**' The 'pre-vitelliform' stage shows little change in the macula. '**B**' The 'vitelliform' stage shows a yellow 'egg-yolk' lesion. '**C**' The 'vitelliruptive' stage as the yellow lipofuscin breaks up. '**D**' The 'pseudohypopyon' stage shows a separation in the lesion with the lipofuscin gathering in the inferior half. '**E**' The 'atrophic' stage is characterised by choroidal atrophy. '**F**' The 'neovascular' stage is characterised by choroidal neovascularisation (CNV). These images were adapted from Boon et al, 2009.

In recent years, several cases of uni-lateral Best disease have also been reported (*49*).

The image in figure 1.6 shows a patient carrying a S16F mutation in *BEST1*.

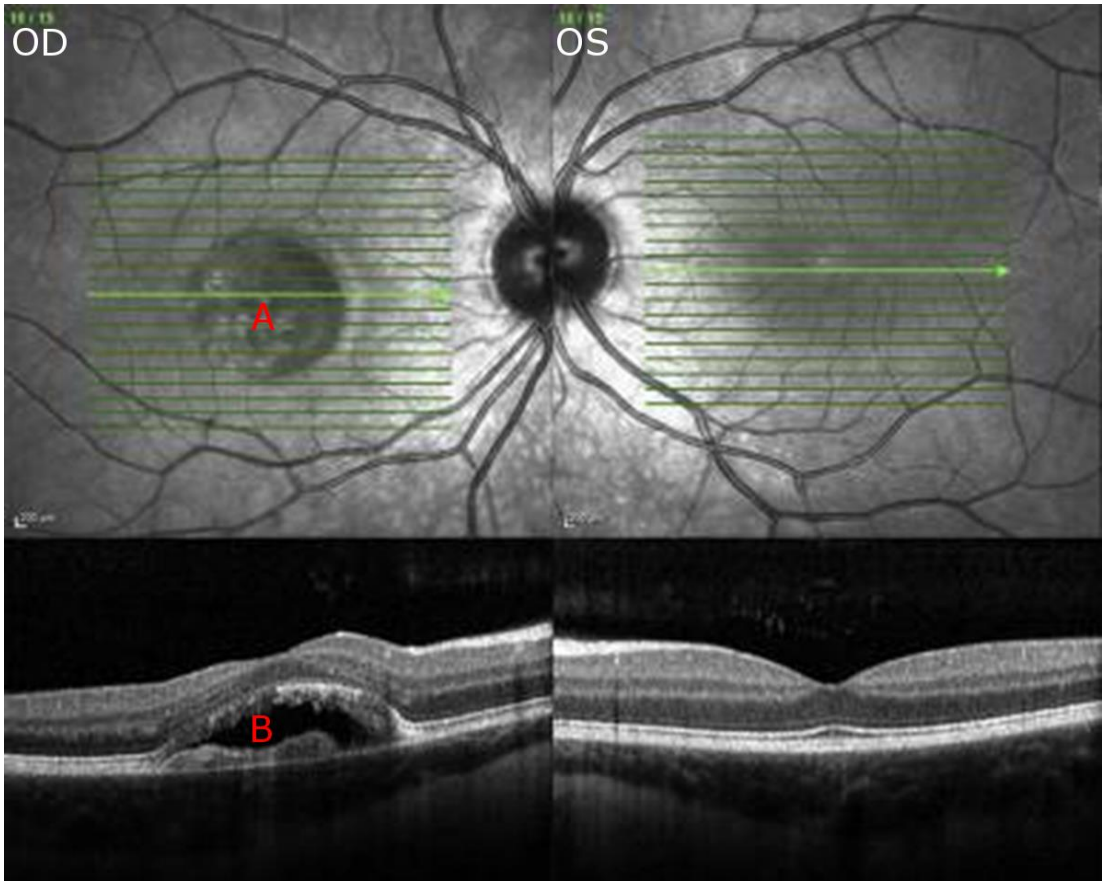

Figure 1.6. OCT Imaging of a Patient with Unilateral Best Disease. In'A' the central lesion is shown in the retina of the right eye (OD). 'B' shows the retinal detachment. The image was taken from Arora et al, 2016.

Autosomal dominant vitreoretinochoroidopathy (ADVIRC; OMIM no. 193220) was first described in 1982 (*50*) and was later found to be caused by mutations in *BEST1* in 2004 (*51*). ADVIRC patients show absent EOG light peaks and progressive choroidal atrophy. In addition patients can display a range of different ocular phenotypes not seen in other bestrophinopathies including circumferential peripheral retinal hyperpigmentation, angle-closure glaucoma, early-onset cataract, microcornea with shallow anterior chambers, iris dysgenesis and optic nerve dysplasia (*50, 52*). Studies have suggested that the mutations identified in ADVIRC result in exon skipping by

disrupting exonic splice enhancers (ESE) present in the *BEST1* mRNA (*51, 53*). To date, mutations resulting in the skipping of exon 4 (c.256G>A), exon 6 (c.707A>G, c.704T>C) and exon 7 (c.715G>A) have been described (*51, 53*). However, a recent study found no evidence of this in iPS-RPE derived from ADVIRC patients (*54*). The authors found bestrophin-1 localised to both the basolateral and apical membranes of patient-derived iPS-RPE (compared to basolateral membrane only in iPS-RPE derived from healthy individuals). RT-PCR and western blotting revealed no evidence of the presence of splice variants in patient-derived iPS-RPE. As the initial degeneration of the retina in ADVIRC occurs in the periphery (*55*) and it's known that bestrophin-1 is expressed predominantly in the peripheral retina (*56*), the author's hypothesise that mislocalisation of bestrophin-1 protein during development may be a root cause of ADVIRC.

Autosomal recessive bestrophinopathy (ARB; OMIM no. 611809) was first described in 2008 (*57*). ARB presents, clinically, with central vision loss and EOG analysis often shows the loss of the light peak (similar to BVMD). Patients also show a central serous detachment (with mild autofluorescence), subretinal scarring and visual acuity can degenerate from 20/20 in the early stages of the condition to less than 20/60 (*47*). The main differences between ARB and BVMD is the abnormal ERG responses (severe photorecpeptor abnormalities often indicated by full-field ERG), the often earlier diagnosis (sometimes as early as the first decade of life, although the mean age-of-onset is 23) and the white, autofluorescent, sub-retinal deposits that are seen predominantly in the mid-periphery and macula (*47*). Some patients can also develop cystoid macular edema and choroidal neovascularisation (*58*). ARB arises when both *BEST1* alleles

carry a mutation, with most patients presenting as compound heterozygotes carrying a different mutation in each allele. Burgess et al identified seven different mutations (six missense and one nonsense) present in 5 families, that segregated throughout the family in a manner consistent with a recessive disease and showed no inhibition of wild-type BEST1 function when co-transfected into HEK293 cells (*57, 59*). Analysis of the localisation of these mutants revealed that some were able to localise to the cell membrane (L41P and, the subsequently described, A195V), whereas others were diffuse throughout the cytosol (R141H, P152A, R202W, V317M and M325T) (*59*). However these studies were performed in MDCKII cells and not a native RPE cell model, therefore it's possible that they could localise differently in the RPE. There is one report of an ARB-associated mutation leading to the alteration of pre-mRNA splicing of *BEST1* (*60*) as well as reports of ARB patients displaying symptoms more commonly associated with ADVIRC, such as shallow anterior chambers and angle-closure glaucoma (*61*). It is hypothesised that ARB represents the *BEST1* null phenotype in humans and has a comparable condition in dogs known as canine multifocal retinopathy (see chapter 1.7.2). It may also be highly amenable to a gene replacement therapy strategy as will be explored in this thesis.

Adult-onset vitelliform macular dystrophy (AVMD) is a condition similar to BVMD in its presentation and inheritance. Like BVMD, AVMD patients present with a vitelliform lesion, however the condition is often less severe than BVMD, with CNV a rare feature in late stages (*47*). AVMD's similarity to BVMD have lead some groups to hypothesise that it represents a more mild form of BVMD and should be re-classified as such (*62*). There have also been some reports of clinically diagnosed retinitis pigmentosa (RP)

resulting from mutations in *BEST1*. Four bestrophin-1 mutants were identified in patients diagnosed with RP: L140V (recessively inherited), I205T, Y227C and D228N (all dominantly inherited) (*63*). *BEST1*-asscociated RP presented with panretinal dystrophy, severely reduced ERG responses (no EOG testing was performed in this study), flecks localised to the mid-periphery, retinal gliosis and vascular attenuation. Dalvin et al describe a further *BEST1* mutant (I366fsX384) associated with RP (*64*), however there is a possibility that these dominant mutations represent miss-diagnosed ADVIRC (*62*).

Mutation	Associated Bestrophinopathy	Reference
T6P	BVMD	Sun et al, 2002
A10V	BVMD	Sun et al, 2002
S16F	BVMD	Marchant et al, 2001
L41P	ARB	Davidson et al, 2011
I73N	BVMD	Milenkovic et al, 2007
Y85H	BVMD	Sun et al, 2002
V86M	ADVIRC	Yardley et al, 2004
R92C	BVMD	Sun et al, 2002
R92S	BVMD	Sun et al, 2002
W93C	BVMD	Sun et al, 2002
N99K	BVMD	Sun et al, 2002
D104E	BVMD	Sun et al, 2002
L140V	ARB and RP	Davidson et al, 2009
R141H	ARB	Burgess et al, 2008
A146K	AVMD	Yu et al, 2007
P152A	ARB	Burgess et al, 2008
A195V	ARB	Davidson et al, 2011
R202W	ARB	Davidson et al, 2011
R218S	BVMD	Sun et al, 2002
R218C	BVMD	Rosenthal et al, 2006
G222E	BVMD	Yu et al, 2007
Y227N	BVMD	Sun et al, 2002
A243T	BVMD	Sun et al, 2002
A243V	BVMD	Yu et al, 2006
V235A	ADVIRC	Yardley et al, 2004
Y236C	ADVIRC	Yardley et al, 2004
F281del	BVMD	Milenkovic et al, 2007
E293H	BVMD	Marchant et al, 2007
E293K	BVMD	Sun et al, 2002
I295del	BVMD	Yu et al, 2007
G299R	BVMD	Yu at al, 2008
G299E	BVMD	Sun et al, 2002
E300D	BVMD	Sun et al, 2002
D301E	BVMD	Sun et al, 2002
T307I	BVMD	Sun et al, 2002
D312N	AVMD and ARB	Yu et al, 2007
V317M	ARB	Davidson et al, 2011
M325T	ARB	Davidson et al, 2011

Table 1. Identified Mutations in BEST1 (not exhaustive).

1.6 Bestrophin-1 Structure and Function

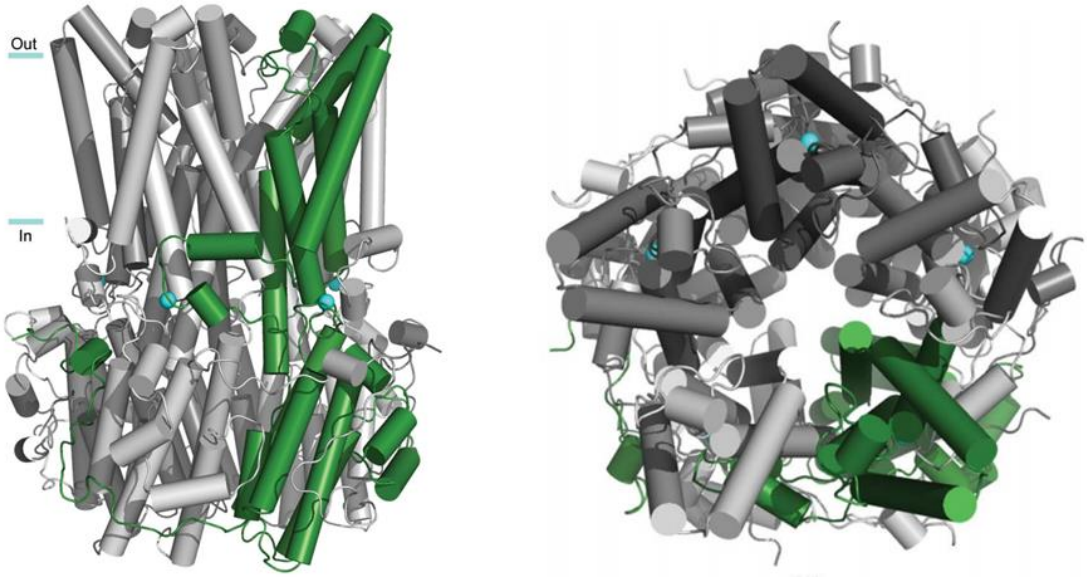

Figure 1.7. Cartoon of Bestrophin-1 Structure. Structure of chicken bestrophin-1 as seen from the membrane plane (**A**) and above (**B**). Figure is adapted from Dickson, 2016.

Bestrophin-1 (*BEST1*) was the first member of the family of bestrophins (the others being *BEST2* (*VMD2L1*), *BEST3* (*VMD2L3*) and *BEST4* (*VMD2L2*)) to be described (*46*). Bestrophin-1 is a 67.5 kDa (585 amino acids) protein that localises to the basolateral membrane of the RPE (figure 1.8), where it functions in the transport of chloride ions (Cl^-) (*65*). Bestrophins are evolutionarily conserved (particularly the first ~350 amino acids) and have orthologues present in nearly all vertebrate and invertebrate species (*66*). Studies using x-ray crystallography have revealed that both eukaryotic (chicken) and prokaryotic (*Klebsiella pneumoniae*) bestrophin-1 monomers form a pentameric channel in the basolateral membrane (*67, 68*). This channel has a central ion conduction pore, ~20 Å across and ~95 Å long, that carries a net positive charge,

indicating that it is for anion conductance (although the prokaryotic channel is negatively charged, indicating cation conductance). Figure 1.7 shows a cartoon of bestrophin-1 structure as determined by x-ray crystallography (*69*). The majority of the bestrophin-1 protein is found intracellularly, including both N and C termini. In eukaryotes, bestrophin-1 carries a conversed arginine-phenylalanine-proline (RFP) motif, within which lie a number of disease-causing mutations (*70*). A Ca^{2+}-binding region is present on one of the intracellular transmembrane domains, located near to the pore. Ca^{2+} binding has recently been shown to induce conformational changes in bestrophin-1 protein structure via Fourier transform infared (FITR) spectroscopy, Brewster angle microscopy (BAM) and atomic force microscopy (AFM) (*71*). Evidence from these studies also confirms that Bestrophin-1 oligomerises and forms pentameric channels (*72*).

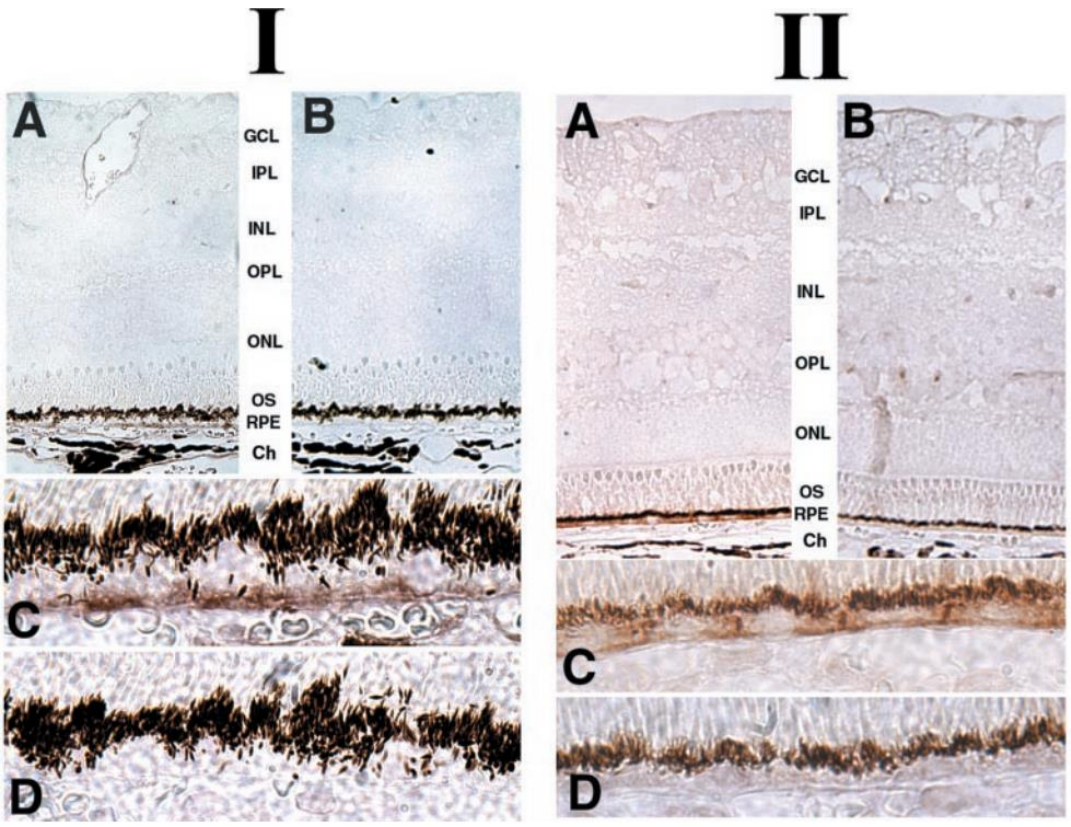

Figure 1.8. Bestrophin-1 Localisation in the Retina. Bestrophin-1 is detected at the basal membrane of the RPE in both Macaque (I-A) and Porcine (II-A) eyes probed with an anti-Bestrophin-1 antibody. Staining is not seen in control eyes (I-B and II-B respectively). 'C' and 'D' show close-up images of the RPE and this staining is seen more clearly. Figure is taken from Marmorstein et al, 2000.

Evidence for the chloride channel function of bestrophin-1 comes from both the structural data afore mentioned and from whole-cell patch-clamping studies of human embryonic kidney (HEK) 293 cells transfected with *BEST1* compared to non-transfected controls. Transfected cells showed large changes in current when patched with a free Ca^{2+} containing intracellular solution when compared to controls (*65*). Also, mutations in the hBEST1 protein have been shown, in vitro, to alter the Cl^- conductance, by transfecting HEK293 cells with various hBEST1 mutants. More recent studies in RPE cells have provided further evidence for this. IPS-RPE derived from

BVMD patients and healthy controls was used to show that volume-regulated anion conduction in healthy cells is ablated in BVMD (*73*). In another study, treatment of IPS-RPE with the Ca^{2+} ionophore A23187 (to stimulate Ca^{2+} release from the endoplasmic reticulum) lead to transport of intracellular chloride out of the cell as measured with live cell imaging with a fluorescent Cl^- biosensor (*74*). IPS-RPE derived from BVMD patients showed retention of chloride within the cell. This and the structural data revealing the Ca^{2+} binding region within the protein (see above) provides strong evidence that bestrophin-1 is both a volume regulated anion channel (VRAC) and a Ca^{2+}-activated Cl^- channel (CaCC). Replacement of Cl^- with gluconate ablated volume regulated anion conductance in healthy IPS-RPE (*73*) and reduced transepithelial potential in fetal-human (fh)RPE overexpressing WT bestrophin-1 (*75*). The regulation of bestrophin-1 via volume would suggest that it is also involved in the transport of water across the RPE via the removal of excess Cl^-, along with the HCO_3^-/Cl^- exchanger described in chapter 1.3.5 and figures 1.3 and 1.4. Bestrophin-1 has also been shown to influence calcium movement and release in the RPE by physically interacting with the β subunit of L-type voltage-dependent Ca^{2+} channels (*57, 75-77*). Bestrophin-1 also appears to regulate the release of Ca^{2+} from the endoplasmic reticulum in response to ATP stimulation (*78, 79*). There is evidence that disease causing mutations can disrupt calcium signalling in the RPE (*57, 75, 80*).

Given the number of conditions that have been associated with mutations in *BEST1*, and the varying clinical phenotypes that arise from these mutations, the 'bestrophinopathies' represent a very complex class of IRDs (table 1.) (*51, 57, 59, 60, 63, 65, 76, 81-85*). The mechanism by which BEST1 mutations cause disease is presently unknown. Given the

wide variation in phenotype and inheritance patterns seen in the bestrophinopathies, it is likely that multiple disease mechanisms are involved. Loss of anion conductance has been shown for BVMD, ARB, AVMD and RP mutants (but presently, not ADVIRC) and the potential disruption of Ca^{2+} conductance (as mentioned above) are the most probable causes, but how this disruption occurs is unclear. Studies have suggested that many bestrophin-1 mutants fail to effectively traffic to the basolateral membrane, implicating impaired protein trafficking in the disease pathogenesis (*54, 57, 63, 86, 87*). This would prevent bestrophin-1 from being able to influence Cl^- and Ca^{2+} movement across the RPE. These studies have been predominantly performed in MDCKII, with very few being performed in RPE cells. Johnson and colleagues also demonstrate that a mutant that mislocalised in MDCKII (W93C) was properly localised when expressed in fhRPE (*87*). It is possible that *BEST1* mutations could affect the ability of the protein to oligomerise and form a pentameric channel. Co-immunoprecipitation and confocal microscopy studies have shown that this is unlikely as 32 mutants (from ARB, BVMD, ADVIRC and RP patients) were shown to associate with wild-type bestrophin-1 in MDCKII cells (*88*). Furthermore, studies in IPS-RPE confirmed that several ARB mutants co-immunoprecipitated with wild-type bestrophin-1 (*89*). A presently unexplored possibility is that mutations could affect the interactions between besrophin-1 and associated proteins such as protein phosphatase 2A, which has been shown to phosphorylate bestrophin-1 (*90*).

Within the eye, bestrophin-1 expression is restricted to the RPE; however expression has also been reported in other tissues such as the brain and the spinal cord in mice (*91, 92*). Bestrophin-1 expression within the brain seems to be limited to neurons and

astrocytes, particularly in the hippocampus, where it appears to be involved in the transport of gluconate, glutamate, isethionate and GABA (*91, 93*). The release of glutamate and GABA from the astrocytes appears to be dependent on Ca^{2+} concentration (*91, 94*). An interesting observation is the contribution of mBest1 in impairing synaptic plasticity and spatial memory in a mouse model of Alzheimer's disease (*94*). Here the distribution of mBest1 changes to become more localised to the soma than the synaptic distal microdomain in the hippocampus and seems to release GABA. Expression of bestrophin-1 in the dorsal root ganglia and spinal cord has been described in mice (*95*). Here it appears to have a role in nociceptive processing and, potentially, in the regeneration of injured sensory neurons and the maintenance of neuropathic pain (*96*).

At the time of writing, bestrophin-1 expression has been reported at the mRNA level in human brain and spinal cord however not at the protein level (*62*). No pathology has been described in the brains of BVMD, ARB or ADVIRC patients. The role of bestrophin-1 outside of the eye is only just being described and it's possible that more information on this topic will elucidate more about the mechanisms of bestrophin-1 in the RPE.

1.7 Models of Best Disease

1.7.1 Rodent Models

Given the absence of a macula in rodents, it is questionable just how well macular dystrophies can be modelled by mice and rats. The mouse Best1 protein also shows just 63% homology with the human protein, making it difficult to produce accurate knock-in models (*97*). Despite this, both mice and rat models of the bestrophinopathies do exist, with varying levels of usefulness.

In mice, Best1 knock-in and knock-out mice have both been produced. Knock-in models of the Best1 W93C mutation have been used to model the autosomal dominant condition BVMD. This model shows retinal lesions and sub-retinal lipofuscin accumulation similar to that seen in BVMD in humans, in both homozygous and heterozygous mice (*79*). This probably indicates that the W93C mutation is a gain-of-function mutation (discussed in chapter 7) and, as such, this model was judged unsuitable for this study. ARB is considered to be the *BEST1* null phenotype in humans, however, $Best1^{-/-}$ mice show no pathology reminiscent of ARB. Photopic and scotopic ERG profiles are the same between $Best1^{-/-}$ mice and wild-type controls (*78*). Whole-cell patch-clamping also revealed no difference in the Cl^- conductance of primary RPE taken from $Best1^{-/-}$ and $Best1^{+/+}$ mice (*78*), indicating that the function of bestrophin-1 may be redundant in murine RPE. Expression studies in mice have detected murine bestrophin-1 in the RPE at the mRNA level but found no expression at the protein level. However, bestrophin-1 was detected in the testis of wild-type mice and this could

explain the sub-fertility phenotype seen in Best1$^{-/-}$ mice (*73*). The lack of bestrophin-1 in the RPE of mice suggests that Cl^- conductance is being regulated by other channels in these cells, possibly CFTR and ClC-2 or maybe Best-2 (*78*).

Modelling of BVMD mutants (W93C and R218C) in rats showed a decrease in the amplitude of the ERG 'c-wave' (analogous to the human EOG light peak) (*98*). These mutants were modelled via transient overexpression using replication-deficient adenoviruses. To the author's knowledge no *BEST1* knock-out or knock-in rat models of BVMD or ARB have been produced.

1.7.2 Canine Model

Canine multifocal retinopathy (CMR) is a naturally occurring inherited retinal condition in dogs that has been identified in ~11 breeds worldwide. The condition is inherited in an autosomal recessive manner and was shown to be caused by canine Best1 (cBest1) mutations in 2007 (*99*). Unlike the rodent retina, the canine retina has a cone dense central region called the *area centralis*. This means that it can serve as a more accurate model of the human retina than the rodent retina. To date, 3 forms of CMR have been described, cmr1 can be present in multiple breeds and is caused by a R25X mutation in cBest1, cmr2 has been identified only in the Coton de Tulear breed and is caused by a G161D mutation. More recently, cmr3 was described in Lapponian herder dogs caused by either a P463*fs* or G489V mutation (*100*). Like ARB in humans, CMR causes retinal detachment (normally limited to the *area centralis*), multifocal lesions, accumulation of

lipofuscin and abnormal ERG responses (*101, 102*). Like the human condition, disease progression can also be divided into stages. Stage 1 is analogous to the 'pre-vitelliform' stage in humans, with little to no fundus changes. Stage 2 is characterised by the appearance of a vitelliform lesion, similar to the 'vitelliform' stage in humans. Stage 3 is similar to the 'pseudohypopyon' stage, with separation of the lipofuscin seen in the lesion. Stage 4 is the 'vitelliruptive' or 'scrambled-egg' stage and stage 5 is characterised by choroidal atrophy (the 'atrophic' stage) (*62*). As cmr recapitulates a number of the characteristics of ARB, including its mode of inheritance, dogs presenting with one of this mutations could be the best *in vivo* model available for the development of novel treatments for human ARB, including gene replacement therapy (*103*). Recent studies in the dog model have increased our understanding of pathology of Best's disease. The gradual increase in lipofuscin granules with age was shown to be equivalent between CMR and human BVMD and ARB. An increase in cholesterol-esters in the photoreceptors of the canine retina in CMR was shown, suggesting degeneration of the interphotoreceptor matric (IPM). The authors also hypothesis that the bestrophinopathies (in particular BVMD and ARB) could be caused by compromised RPE-photoreceptor interactions evidenced by retraction of RPE apical microvilli seen in the CMR dog (*104*). These could offer new endpoints to analyse following any treatment tested in the dog model.

1.7.3 *In Vitro* Model Systems

The production of cell lines that stably express wild-type and mutant bestrophin-1 offer model systems that allow *in vitro* studies to elucidate function and test therapeutics.

Recent studies with Madin-Darby Canine Kidney 2 (MDCKII) cells, that were stably transfected with WT *BEST1* and ARB-associated mutants, allowed the visualisation of mislocalised bestrophin-1 protein the cytosol. Treatment of the cells with proteosomal inhibitors (Bortezomib and 4-phenylbutyrate) restored bestrophin-1 localisation to the basolateral membrane of the MDCKII cells and hence represent a potential treatment for ARB (*105*).

In recent years, induced pluripotent stem cells (iPSC) have gained a lot of traction in the modelling of various inherited conditions. Studies in iPS-RPE generated from BVMD patients allowed the testing of valproic acid and rapamycin as potential treatments. Singh et al identified that BVMD mutations interfered with the ability of IPS-RPE to phagocytose POS, which was reversed by valproic acid treatment (*106*). Whole-cell patch-clamping in iPS-RPE derived from ARB patients and controls allowed Milenkovic et al to analyse the volume regulation of bestrophin-1 and show that this regulation is ablated in ARB (*73*).

1.8 Gene Therapy for IRDs

1.8.1 Gene Replacement Therapy

Gene therapy is a branch of medicine which is rapidly gathering pace in many fields of modern medicine. There are two broad approaches: replacement of a mutated gene with a functional copy or introduction of a gene, the product of which could confer a therapeutic effect. The earliest mentions of the prospect of gene therapy date back to the mid-1960's and following the cloning and identification of CFTR as the causative gene of the autosomal recessive condition cystic fibrosis in the 1980's (*107*, *108*), it was hypothesised that the condition could be treated by replacing the CFTR gene in CF patients.

1.8.2 Gene Therapy and Ophthalmology

There are several clinical trials currently ongoing for inherited ocular conditions such as Leber Congenital Amaurosis (LCA), Choroideremia and MERTK-associated Retinitis Pigmentosa (*109-112*). Several trials for LCA have been conducted in the USA and UK. Results of the UK trial showed some temporary improvement in vision but the authors concluded that the level of expression given by their AAV2/2 vector was not sufficient to correct the condition (*113*). The group have since reported the testing of an optimised construct, with an altered promoter, that was reported to give up to 300-fold greater RPE65 expression in mice (*114*). Trials in the USA have reported improvements in

visual function several years post-treatment, possibly because of the use of stronger promoters in the constructs (*115-117*).

As of the time of writing, gene therapy trials for choroideremia (CHM) are taking place in the UK, Germany, Canada and USA. In the UK, patients injected with an AAV2/2 vector expressing *REP1* showed sustained increases in visual acuity 2 years post-treatment (*111*). Improvements in sensitivity (as measured by dark-adapted microperimetry) and night vision were also reported (*110*).

Phase 1 dose escalation trials have also been undertaken for *MERTK*-associated RP using an AAV2/2 vector expressing *MERTK* under the control of the RPE-specific *VMD2* (*BEST1*) promoter (*112*). 3 out of 6 patients showed signs of improvement in VA however these improvements were lost by 2 years post-treatment. Like the aforementioned UK LCA trial, this may be due to low expression being driven by the RPE-specific promoter.

A recent phase I trial for X-linked retinitis pigmentosa (XLRP) has been initiated at the Oxford Eye Hospital in the UK. This trial utilises an AAV2/8 vector to transfer *RPGR*, under the control of the rhodopsin kinase (RK) promoter, to the photoreceptors of patients suffering from XLRP. At the time of writing no data has been published from this trial. The trial is based on pre-clinical data showing rescue of disease phenotype (via restoration of the phototopic and scotopic ERG) in *Rpgr*$^{-/-}$ mice at 6 months post sub-retinal injection (*118*). Recent pre-clinical studies in America have also shown similar results in *RPGR*-deficient dogs using an AAV2/5 vector (*119*).

Gene therapy is also making an impacted in ocular conditions that are not considered to be inherited degenerations. In Australia, Constable et al recently published results from a phase 2 clinical trial for wet age-related macular degeneration (AMD) (*120*). The authors report improved VA in 12 twelve patients treated with a rAAV vector expressing Soluble fms-like tyrosine kinase-1 (*sFLT-1*), an anti-VEGF inhibitor.

All the trials mentioned utilised a rAAV vector to deliver the relevant transgene to the RPE/photoreceptors. In all cases the doses of rAAV were well tolerated with no adverse effects seen other than those associated with the surgery. Although anti-AAV antibodies were found to be increased in some patients there was no inflammation or abnormal T-cell responses following treatment. Vector shedding studies showed no spread of the rAAV genome outside of the eye.

Autosomal recessive bestrophinopathy (ARB) could be highly amenable to a gene therapy treatment strategy for several reasons. Firstly, the autosomal recessive nature of the condition means that expression of the wild-type protein in the RPE of ARB patients should restore bestrophin-1 function. Secondly, the *BEST1* coding sequence (CDS) is ~1.7 kb in size, small enough to be packaged into a rAAV capsid (alongside a promoter and regulatory sequences, it should still fit neatly inside the 4.7 kb packaging limit). Thirdly, the characteristic retinal detachment could make the surgery far simpler to perform as the sub-retinal space is already exposed to the surgical needle with no need to induce a detachment.

1.9 Vector Choice in Gene Therapy

1.9.1 Adeno-associated Virus

Most gene therapy strategies for IRDs have involved the use of an AAV vector, predominantly because AAV vectors have been shown in multiple studies to efficiently transduce both the RPE and the photoreceptors (*121*). AAV was initially discovered in 1965 as a contaminant in adenovirus preparations and has since been characterised as a member of the *parvoviridae* family of viruses (*122*). AAV is a non-enveloped virus, ~25 nm in diameter, which contains a single-stranded DNA genome containing ~4.7 kb of DNA. The AAV genome contains two sequences required for the virus's replication, named 'Rep' (encoding important virus life-cycle proteins Rep78, Rep68, Rep52 and Rep40) and 'Cap' (coding for the capsid proteins VP1, VP2 and VP3). These sequences are flanked by two inverted-terminal repeats (ITRs) that hybridise to allow second strand synthesis from the ssDNA genome (*123*). AAV is unable to replicate by itself and requires the assistance of 'helper' viruses (such as the adenovirus), an attractive feature for use in gene therapy. The adenovirus supplies the E4, E2a and VA genes that help to mediate replication (*124*). When producing recombinant AAV for gene transfer, the relevant transgene is contained on one plasmid, flanked by the AAV ITRs and the Rep, Cap and helper genes are supplied on additional plasmids *in trans* (*125*). This process is depicted in figure 1.9 (*126*).

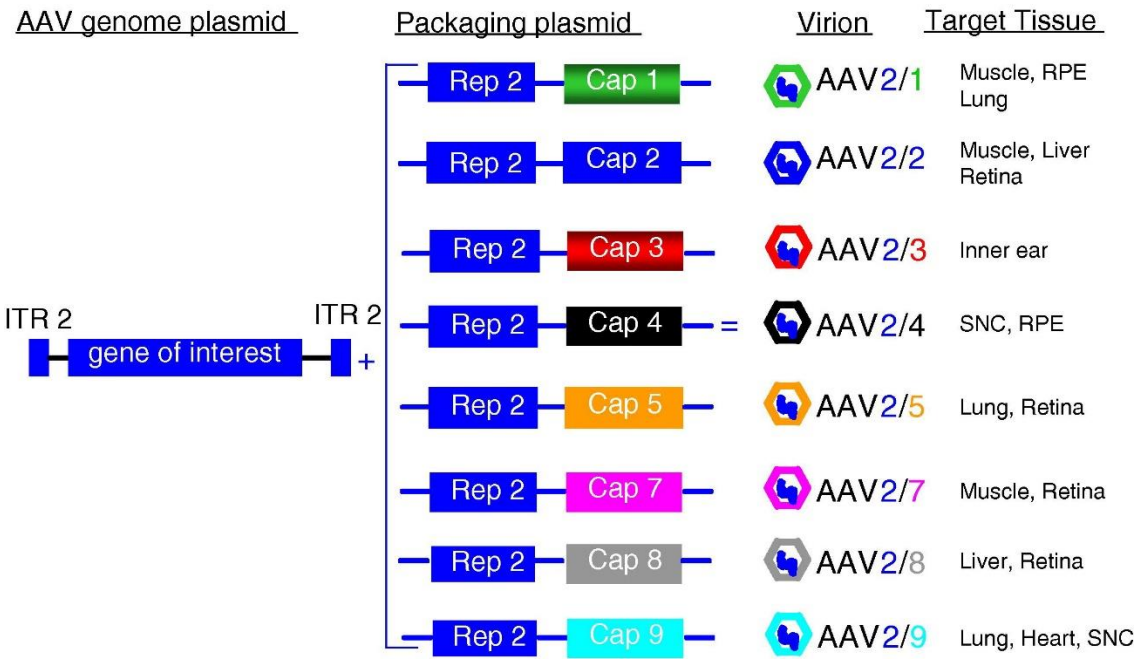

Figure 1.9. Production of rAAV Serotypes and Tissue Specificity. The 'gene-of-interest' is supplied on a plasmid flanked by the AAV ITRs. The Rep and Cap genes are supplied on a second plasmid, the combination of these determines the AAV serotype. Different serotypes transduce cells throughout the body with varying efficiency. Figure is taken from Surace et al, 2008.

AAV binds to glycan receptors and co-receptors on the cell surface and is internalised into endocytic vesicles (*127*), a process that was thought to be dependent on clathrin (*128*), but has since been shown to be independent of clathrin (*129*). Co-receptors are known to include $\alpha_v\beta_5$ integrins, $\alpha_v\beta_1$ integrins, hepatocyte and fibroblast growth factor receptors and laminin receptors. The presence of $\alpha_v\beta_5$ integrins on the apical surface of the RPE (required for POS phagocytosis, see chapter 1.3.1) might explain the high efficiency at which AAV transduces the RPE. Until recently, the receptor that facilitates AAV cellular internalisation was unknown. In 2016, Pillay et al identified a receptor which is essential for the uptake of AAV, which they termed 'AAVR' (*130*). Having

identified the gene *KIAA0319L* (AAVR) as enriched in cells with high tropism for AAV compared to controls, the authors show that inhibition of AAVR ablates AAV transduction *in vitro* and *in vivo*. Following uptake, AAV is trafficked through endosomal vesicles to the trans-Golgi network, where it is processed prior to nuclear import. Nuclear import is facilitated by importin. The AAV capsid uncoats in the nucleus and releases the AAV genome which exists episomally, without integrating into the host cell genome. For this reason, AAV is often used to transduce 'quiescent' cell types such as neurons, as multiple cell divisions can cause loss of the episomal AAV genome. The process of AAV uptake and uncoating is summarised in figure 1.10.

Cell-specific tropism is an important consideration when using AAV to transduce the retina. Different serotypes have different specificities for cells within the retina, for example, following sub-retinal injection AAV2/2, AAV2/5, AAV2/7, AAV2/8 and AAV2/9 transduce both the photoreceptors and the RPE (although each show different specificities for each of these two cell types). AAV2/1, AAV2/4 and AAV2/6 predominantly transduce the RPE with little to no transduction of the photoreceptors. Following intravitreal delivery, AAV2/2 and AAV2/8 were able to transduce retinal ganglion cells (RGCs) (*131-133*). The differences seen in cell tropism may depend on the cell surface glycans present on the RPE and photoreceptors, which also differ between species (*134*). Recent advances in capsid engineering have improved the efficiency of transducing various retinal cells such as RGCs and bipolar cells (*135, 136*). The conversion of tyrosine to phenylalanine in the AAV2/8 Y733F and AAV2/2 Y444F mutant capsids is thought to inhibit the degradation of AAV capsids following endocytosis by preventing tyrosine phosphorylation and subsequent ubiquitination-

mediated degradation via the proteosome (*137*). Recent studies have shown the efficacy of these vectors for gene transfer into the retina of mouse models of end-stage retinal disease (*138*).

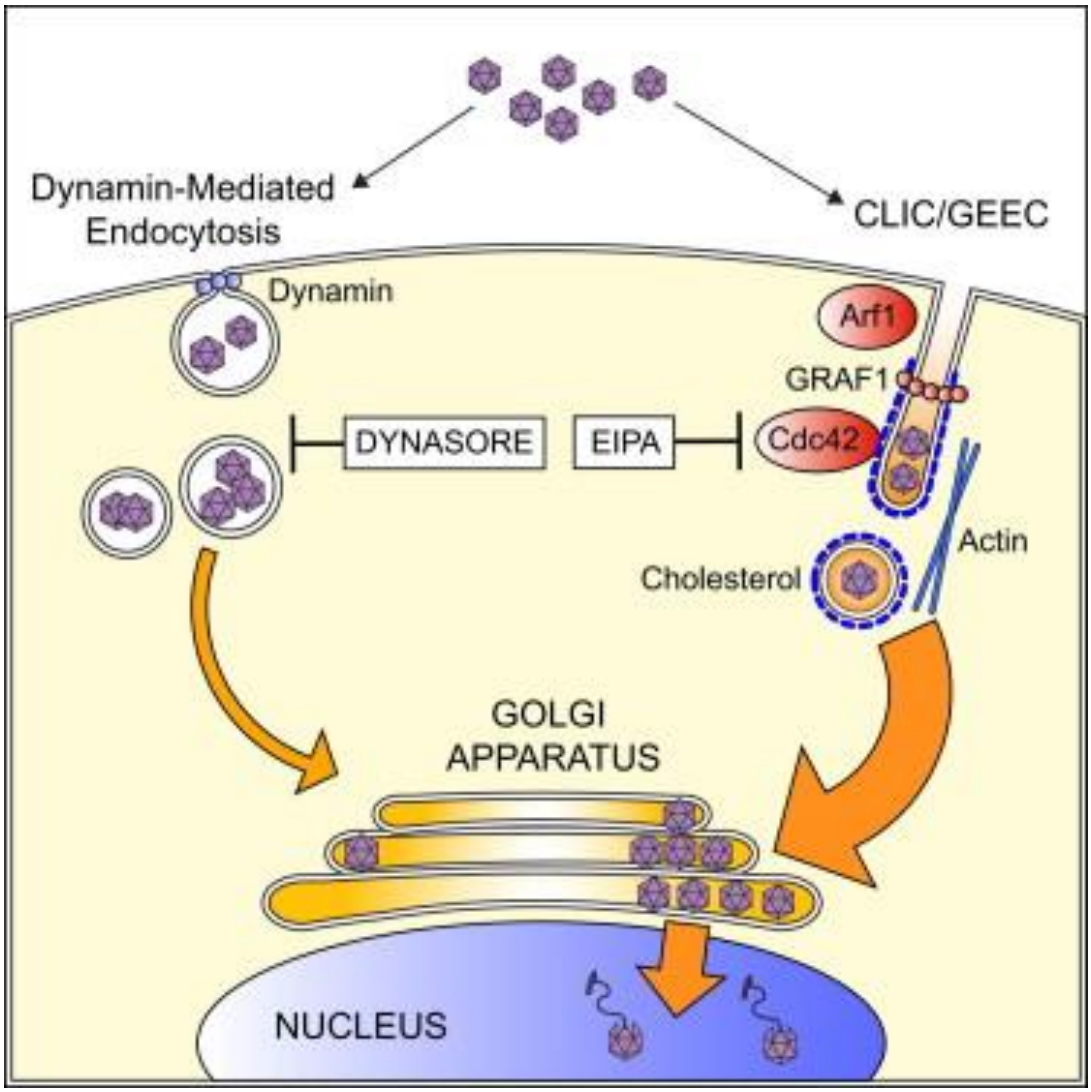

Figure 1.10. Cellular Uptake and Processing of AAV. AAV uptake is independent of clathrin and mediated by either dynamin or CLIC/GEEC pathways. Figure is adapted from Nonnenmacher et al, 2011.

Despite its success in ocular gene transfer, AAV does have some drawbacks, the primary one being its relatively small packaging capacity (< 4.7 kb). This makes the

treatment of some IRDs, such as Stargardt's disease, more challenging (*ABCA4* CDS is ~6.8 kb, exceeding the packaging capacity even before the addition of the promoter and polyadenylation sequences). For ARB, proof-of-principle for the use of rAAV vectors to transfer human bestrophin-1 to the RPE was demonstrated by Guziewicz et al, 2013 in the CMR dog model. Sub-retinal injection of both human and canine bestrophin-1 was performed with AAV2/1 and AAV2/2 serotypes delivering *BEST1* under the control of the *hVMD2* promoter, demonstrating safety in both cmr1 dogs and wild-type controls (*103*).

Widely considered to be the principle rate-limiting step in AAV-transduction is the synthesis of the second DNA strand from the single-stranded AAV genome (*139*). Self-complementary AAV vectors contain both forward and reverse copies of the relevant transgene that are linked by a third inverted terminal repeat. Following capsid unfolding, the self-complementary vector hybridises to itself, bypassing the need for second-strand synthesis. This allows for a faster onset of transgene expression, with one study in mice showing high expression of GFP in the RPE following sub-retinal injection of scAAV2/2-GFP 3 days post-injection which was only matched by the single-stranded AAV2/2-GFP after 14 days (*140*). This has also been seen when using other AAV capsids such as AAV2/8 (*141*).

AAV is not known to cause any human disease, however studies using AAV to transfer genetic material to the liver have indicated that a strong immune response could ensue following systemic administration (*142*). The isolation and 'immune-privilege' of the human eye may avoid the systemic spread of the AAV vector. The innate immune

response to AAV may be mediated by toll-like receptor 9 (TLR9), which responds to AAV infection by activating the inflammatory NF-κB pathway (*143*). Innate immune responses to AAV are far lower than for other viruses (*144*).

1.9.2 Retrovirus and Lentivirus

Retroviruses are enveloped viruses, containing a single-stranded RNA genome, that integrate their genomes into the host cell genome, producing stably-transduced cells. Stable integration of genetic material into the host genome gives long-lasting expression when compared with other vectors and also means that the introduced genes will be replicated and passed on to daughter cells. However the integration of the retroviral genome raises some potential issues with insertional mutagenesis. Retroviruses have a much larger packaging capacity than AAV does and can accommodate around 10 Kb of DNA. However, retroviruses can only transduce dividing cells, as they have no mechanism of entering the nucleus without the breakdown of the nuclear envelope. This means that their use in the, predominantly neuronal, retina is limited (*145*).

Lentiviruses (LV) are members of the *retroviridae* family and are based on the HIV-1 retrovirus. LV are enveloped, contain a single-stranded RNA genome and integrate their genome into the host cell genome, with a packaging capacity of ~8kb. Unlike the retroviruses that they are based on, LVs are able to transduce quiescent cells as they do not require the breakdown of the nuclear envelope during mitosis to enter the nucleus. This is achieved via a pre-integration complex which uses the host cell machinery to

transport itself into the nucleus (*146*). Like the traditional retroviruses, the integration of the LV genome can cause issues with insertional mutagenesis.

There has been some pre-clinical success at using lentivirus gene transfer to treat IRDs, in particular with Stargardt's disease, due to the larger packaging capacity of LV when compared to AAV. Pre-clinical studies in the *Abca4*$^{-/-}$ mouse showed reduction in lipofuscin following LV-mediated transfer of human *ABCA4* to the photoreceptors (*147*). However, <20% of photoreceptors within the injection site were successfully transduced, which is consistent with previous work in LV-mediated retinal gene transfer.

1.9.3 Adenovirus

The adenovirus is a common, naturally occurring human pathogen that was first identified in 1953 (*148*). Adenoviruses range from 90-100nm in size (dependent on serotype), are non-enveloped icosahedral viruses and contain a 30-40kb linear double-stranded DNA genome. This large packaging capacity makes adenovirus very attractive for the transfer of large genes to target cells. They are capable of infecting both dividing and non-dividing cells, do not integrate into the host cell genome and have a broad tropism, so can be used for gene transfer into multiple cell types in the body (*149*). In the retina, adenovirus has been shown to elicit efficient gene transfer and long-term transgene expression in the RPE following sub-retinal injection (*150*), however transduction of the photoreceptors is far less efficient (*151*). A major drawback with the use of adenovirus is it's tendency to elicit a far greater immune response than either

AAV or lentivirus, possibly due to many adults having high antibody titres of the main adenoviral serotypes, such as serotype 5 (*152*). Adenovirus also has been shown to elicit a strong innate immune response in the eye, with upregulation of IFN-associated genes even at low MOI (0.5) (*153*).

There have been some pre-clinical studies published that have used adenovirus to transfer genetic material to the retina. Adenovirus-mediated transfer of complement Factor H reduced endothelial proliferation and RPE atrophy by 91% and 69% respectively in a murine model of AMD (*154*). Another recent study used adenovirus-mediated transfer of calreticulin anti-angiogenic domain to treat choroidal neovascularisation in rats, showing a reduction in CNV lesions (51%) compared to un-treated controls (*155*). To the author's knowledge there have been no clinical trials using adenovirus to transfer genetic material to the retina/RPE.

1.9.4 Non-Viral

Viral vectors such as AAV and LV are currently the preferred methods of gene transfer into the cells of the retina. However, the use of these has several drawbacks including immunogenicity, insertional mutagenesis (LV) and reduced packaging capacity (AAV). One way of overcoming these obstacles would be to use non-viral forms of gene transfer. There are two broad ways of transferring DNA into cells without the use of a virus, chemical transfer and physical transfer. LacZ expression was detected in the RPE of Balb/C mice following sub-retinal injection of plasmid DNA contained in a cationic

liposomal formulation (*156*). However, no LacZ expression was detected in the photoreceptors and there was some evidence of toxicity as assessed by ERG. Another chemical method would be the use of cationic polymers such as polyethylenimine (PEI), which has been shown to successfully transfect inner retinal cells following intravitreal injection but not sub-retinal injection (*157*). Physical transfer of plasmid DNA often takes the form of electroporation, whereby the membrane of target cells are stimulated by electrodes into taking up the plasmid DNA. Electroporation has been used to transfect the retina previously however, expression dropped off 1 month post-procedure and therefore it may not be useful for clinical gene therapy (*158*). The use of ballistic gene transfer, or 'gene-guns' involves the use of high-voltage discharges devices to 'fire' particles, coated with DNA, into cells and tissues (*159*). Whilst this technology has been used to transfer genetic material to the cornea, to the author's knowledge, it has not been successfully used in retinal gene transfer (*160*).

1.10 Promoter Choice

The preferential targeting of different cell types can also be achieved by the use of different promoters to drive transgene expression. There are two broad classes of promoter, ubiquitous (will drive transgene expression in most, if not all, cell-types) and cell-specific. The most commonly used ubiquitous promoters are the chicken β-actin (CBA) promoter and Cytomegalovirus (CMV) enhancer promoter (*161*). A very common variant of these is the hybrid CBA promoter with CMV enhancer (also known as the 'CAG' promoter) (*162*). The CAG promoter has been used successfully in clinical trials for the retinal condition known as choroideremia (*110*).

Strong ubiquitous promoters, such as CAG, may not be desirable for use when the relevant transgene is not ubiquitously expressed. Other clinical trials have utilised cell-specific promoters, which have the advantage of limiting gene expression to specific cells and tissues and may, subsequently, lead to less toxicity as a result of off-target expression. The RPE-specific promoters *RPE65* and *VMD2* have both been used in clinical trials to drive expression of *RPE65* and *MERTK* respectively (*112, 113*). Other cell-specific promoters could include the Rhodopsin promoter (*RHO*) and human Rhodopsin kinase 1 (*hGRK1* or *RK*) for targeting the rod photoreceptors (*118, 163, 164*). Cone-specific promoters have also been developed, such as the human red opsin (pR2.1) promoter (*165*).

One drawback of cell-specific promoters is that they tend to drive lower levels of protein expression than their ubiquitous counterparts, in some cases only achieving ~10% expression when compared to the CMV promoter (*166, 167*). The RPE65 promoter was also shown to be ineffective in older *RPE65*$^{-/-}$ Briard dogs, highlighting a potential issue with the downregulation of cell-specific promoters in the disease state (*166*). However, it is possible that using a gene-specific promoter could elicit similar levels of transgene expression to the none-diseased state. The use of photoreceptor-specific promoters has had some success in giving more efficient photoceptor transduction than the CMV and CAG promoters. The rhodopsin kinase promoter has been used in pre-clinical studies for IRDs such as XLRP, AIP1-associated RP and RPGRIP1-associated LCA (*118, 119, 168-171*) with promising results.

1.11 Aims and Hypothesis

The overall aim of this project was to produce an adeno-associated virus vector capable of transferring functional bestrophin-1 to RPE of patients suffering from ARB. To achieve these aims we will:

- Produce rAAV vectors expressing *BEST1* and evaluate bestrophin-1 expression *in vitro* via western blot and immunocytochemistry (ICC).
- Evaluate changes in chloride conductance *in vitro* via whole-cell patch-clamping.
- Confirm *BEST1* transgene integrity using mass spectrometry.
- Evaluate human bestrophin-1 expression *in vivo* via western blot and immunohistochemistry (IHC).
- Evaluate retinal toxicity using optical coherence tomography (OCT)

As AAV2/2 has been used successfully in clinical trials for other IRDs, our hypothesis is that transferring the *BEST1* CDS, under the control of a ubiquitous CAG promoter, to cells *in vitro* and RPE *in vivo* will give sufficient expression to restore the chloride transport function lost in ARB.

Chapter 2. Materials and Methods

2.1 Primer Design

Primers were designed using Primer3 (via Geneious R7, Biomatters Ltd). GC content was kept to between 40-60% and melting temperatures ranged from 55 °C to 70 °C. Primer sequences are shown in table 6.

2.2 Polymerase Chain Reaction

Polymerase Chain Reactions (PCRs) were performed using KOD Hot Start Master Mix (Millipore, Cat#71842). 10 ng of plasmid was added to 0.6 µl of each primer, 10 µl of KOD Hot Start Master Mix and was made up to 20 µl with molecular grade water (Sigma Aldrich, Cat#RNDB0544). Reactions were performed on a Bio-Rad T100 Thermal Cycler as follows: 95 °C for 2 minutes, followed by 40 cycles of 95 °C for 20 seconds, lowest primer Tm °C for 10 seconds, 70 °C for 20 seconds/kbp.

2.3 Restriction Digestion

Restriction digests were performed using enzymes from New England Biolabs. 1000 ng of plasmid was added to 2 µl of NEB 10x buffer and 1 µl restriction enzyme. Reactions were made up to 20 µl with sterile water and were incubated at 37 °C for 1 hour in a water bath. Samples were analysed by agarose gel electrophoresis (see section 2.7).

2.4 Ligation

Ligations were performed using T4 Ligase (Promega, Cat#M0202L). 3:1 ratios of insert:backbone were calculated using the following equation:

$$\frac{\text{ng of vector x kb size of insert}}{\text{kb size of vector backbone}} \text{ x molar ratio of } \frac{\text{insert}}{\text{vector backbone}} = \text{ng of insert}$$

Insert and vector backbones were mixed with 1 µl 10x Buffer, 1 µl T4 Ligase and were made up to 10 µl with sterile water. Reactions were left at room temperature overnight. More details of the ligation are provided on pages 90-92.

2.5 Transformation

XL10-Gold Ultracompetent Cells (Agilent Technologies, Cat#200314) were used for transformation procedures. 2 µl of β-mercaptoethanol was added to 50 µl of XL10 cells on ice. The cells were incubated for 10 minutes on ice before 2 µl of ligation mixture was added. The cells were incubated on ice for a further 30 minutes. XL10 cells were then heat-shocked at 42 °C for 30 seconds and incubated on ice for 2 minutes. 950 µl of pre-heated (37 °C) SOC medium (Life Technologies, Cat#15544-034) was added to the cells and the cells were incubated at 37 °C, with shaking at 225 rpm, for 1 hour. LB (Luria Broth) agar plates were made up by adding 25 g of LB (Invitrogen, Cat#12795-027) and 15 g of Agar (Invitrogen, 30391-023) to 1 litre of distilled water. This was autoclaved, melted using a microwave and ~5 mL was poured into petri dishes (10 cm diameter). LB agar was allowed to dry at room temperature. 200 µl of transformed

bacterial culture was added to the LB agar plate and spread using a sterile spreader. The plates were incubated for 10-12 hours at 37 °C.

2.6 Growing Bacterial Cultures and DNA Megaprep

Single colonies, from LB agar plates, were picked and added to 5 mL of LB media (Invitrogen, Cat#12795-027) with 100 ng/ml of Ampicillin. This was incubated at 37 °C, with shaking at 225 rpm, for 8 hours (pre-incubation). 1 mL of the pre-incubated bacterial culture was then added to 499 mL of LB+Amp and incubated at 37 °C, with shaking at 225 rpm, for 10-12 hours. The bacterial cultures were centrifuged at 6,000 x g for 15 minutes and plasmid DNA was isolated using the Qiagen Plasmid Mega Kit (Qiagen, Cat#12183). Samples were eluted using sterile water and quantified using a Nanodrop Spectrophotometer (Thermo Scientific, Cat#ND-1000).

2.7 Agarose Gel Electrophoresis

1-2 g of agarose (GeneFlow, Cat#A4-0700) was added into 100 mL of distilled water and dissolved using a microwave. 5 µl of ethidium bromide (Sigma Aldrich, Cat#E1510-10ML) was added to the agarose prior to casting the gel. Samples were diluted in 10x loading buffer (Invitrogen, Cat#10816015) and an appropriate molecular ladder was loaded for reference. Agarose gels were run at 60-90 V until the bands were suitably spaced. Gels were imaged using the Syngene U:Genius Transilluminator.

2.8 Sequencing

1000 ng of plasmid DNA was diluted into 10 µl of sterile water with primers at 3.2 pmol/µl. Samples were sent to Source Bioscience for Sanger Sequencing. Results were analysed using Geneious R7 software (Biomatters, NZ).

2.9 Growth and Maintenance of HEK293T and HEK293

The respective media for each cell-type is detailed in table 2. Cells were grown in T75 flasks and passaged upon reaching ~70% confluency. HEK293 were detached from the cell culture flask by incubation with 1xTrypsin (Sigma Aldrich, Cat#T2600000) at 37 °C for ~5 minutes. HEK293 cells were collected in 10 ml of culture media and centrifuged at 300xg for 5 minutes at 20 °C. The cell pellet was resuspended in 10 ml of culture media and 1-3 ml of this was taken and added to a fresh cell culture T75 flask. The volume, in the flask, was made up to 10 ml with cell culture media.

Cells	Media and Supplements	Amount (ml)	Supplier	Catalogue Number
HEK293	Minimum Essential Media (MEM)	440	Sigma Aldrich	M2279
	Fetal Bovine Serum (FBS)	50	Life Technologies	10082-147
	L-Glutamine	5	Sigma Aldrich	G7513
	Penicillin/Streptomycin	5	Sigma Aldrich	P0781
HEK293T (Normal Culture)	Dulbecco's Modified Eagle Media (DMEM)	440	Sigma Aldrich	D6546
	Fetal Bovine Serum (FBS)	50	Life Technologies	10082-147
	L-Glutamine	5	Sigma Aldrich	G7513
	Penicillin/Streptomycin	5	Sigma Aldrich	P0781
HEK293T (Transfection Media)	Dulbecco's Modified Eagle Media (DMEM)	480	Sigma Aldrich	D6546
	Fetal Bovine Serum (FBS)	10	Life Technologies	10082-147
	L-Glutamine	5	Sigma Aldrich	G7513
	Penicillin/Streptomycin	5	Sigma Aldrich	P0781

Table 2. Cell Culture Media

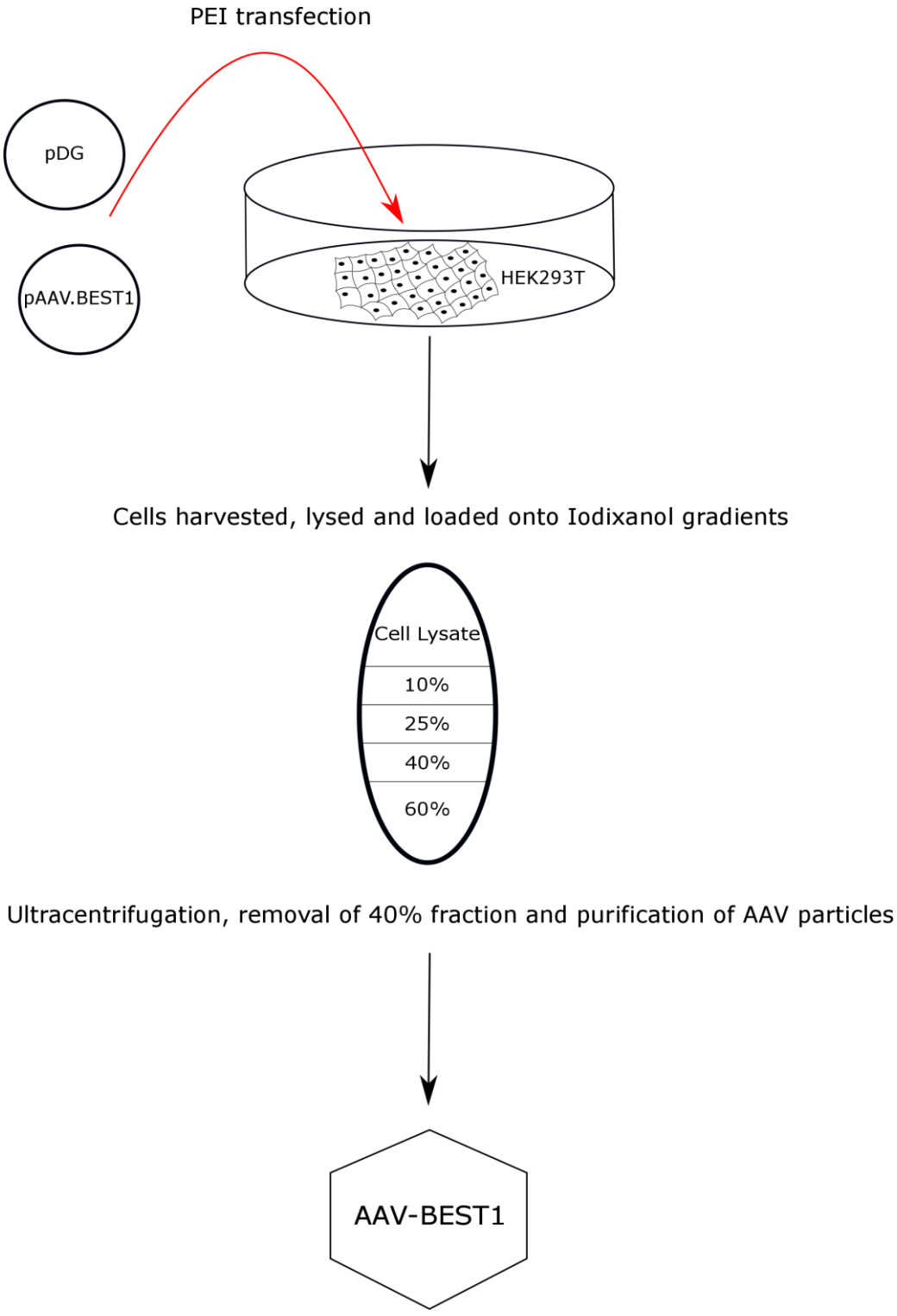

Figure 2.1. Summary of the Production of recombinant Adeno-Associated Virus (AAV) vectors for BEST1 gene therapy.

2.10 Seeding of HEK293T Cells into Hyperflasks for AAV Production

HEK293T cells were used for AAV production. 1.5 T75 flasks, at >90% confluency (|$1.7x10^6$ cells), were used to seed one Corning Hyperflask (Sigma Aldrich, Cat#CLS10012), with a 6000 cm^2 surface area. Two to four hyperflasks were used per AAV. Cells were washed with 1xPBS and re-suspended in 10 mL of normal culture media (see table 2). Clumps were dispersed, before 190 mL of media was added to the T75 flask. This was poured into the Hyperflask. The hyperflask was filled with additional culture media. HEK293T cells were incubated at 37 °C, with 5% CO_2, for ~3 days post-seeding.

2.11 Transfection of HEK293T Cells for AAV Production

The AAV2/2 helper plasmid pDG (Plasmid Factory, Cat#PF421) was mixed with pCAG.hBEST1.pA and pCAG.hBEST1.WPRE.pA (shown in figure 2.2), respectively, to a total amount of 500 µg per transfection mix, in 50 mL falcon tubes. Each transfection mix was made up to 10 mL with 150 mM NaCl. 2 separate 50 mL falcon tubes had 1,125 µl of PEI (Polysciences, Cat#23966-2) added to each, which was made up to 10 mL with 150 mM NaCl. The PEI mix was added, dropwise, to the plasmid mix and allowed to incubate at room temperature for 20 minutes. The transfection mix was added to 500 mL of HEK293T culture media. The media was removed from the Hyperflasks and the fresh media (containing the transfection mix) was added to the cells. The cells were incubated at 37 °C, with 5% CO_2, for 3 days post-transfection.

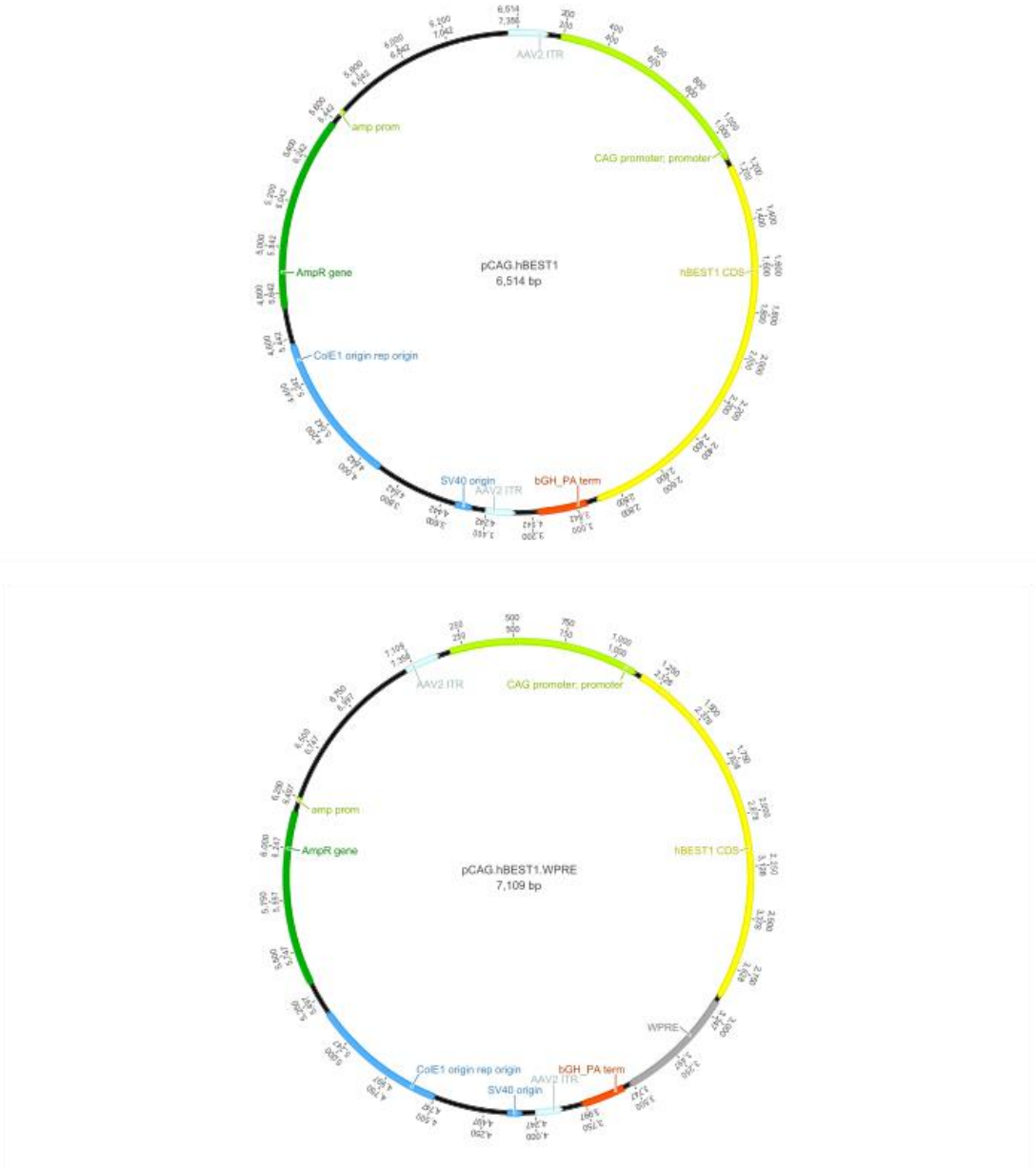

Figure 2.2. Plasmid maps for pCAG.hBEST1 and pCAG.hBEST1.WPRE. These were generated using Geneious version 7.1 created by Biomatters.

Plasmid	Size(kb)	Amount per transfection (µg)
pDG	22.00	22.00 x **R**
pBEST1	T	T x **R**
Total	K	500.00
Ratio (**R**) mass/kb	500/K	

Table 3. Preparation of Plasmids for AAV Transfection.

2.12 Harvesting HEK293T Cells for AAV Production

Cells were loosened by vigorous shaking of the hyperflask. The cell suspension was then transferred to a 500 mL flask and centrifuged at 1,000 x g for 10 minutes at 20 °C. The resultant pellet was not secure; therefore the media was removed leaving about 30 mL in the flask. This was transferred to a 50 mL falcon tube and centrifuged at 1,000 x g for 10 minutes at 20 °C. The media was removed completely, 15 mL of lysis buffer (see table 4) was added to the cell pellet and the cells were lysed using freeze-thaw fractionation

Buffer	Components	Supplier	Catalogue Number
Polyethylenimine (PEI) 10mM	Polyethylenimine, linear (MW 25,000)	Polysciences	23966-2
	Molecular Biology Grade Water	Sigma Aldrich	95284
Sodium chloride (NaCl) 150mM	Sodium chloride (NaCl)	Sigma Aldrich	S9625
	Molecular Biology Grade Water	Sigma Aldrich	95284
NaCl 5M	Sodium chloride (NaCl)	Sigma Aldrich	S9625
Lysis Buffer, pH 8.5	1M Tris(hydroxymethyl)aminomethane	VWR	103156X
	150mM NaCl	Sigma Aldrich	S9625
	Molecular Biology Grade Water	Sigma Aldrich	95284
5X PBS-MK	PBS Tablets	Life Technologies	18912-014
	5mM $MgCl_2$	Sigma Aldrich	M8266
	12.5mM KCl	Sigma Aldrich	P9333
	Molecular Biology Grade Water	Sigma Aldrich	95284

Table 4. Buffers for AAV Production

2.13 Isolation and Purification of AAV

Benzonase was added to the lysates at a final concentration of 50 U/mL and the lysates were incubated at 37 °C for 45 minutes. Following incubation, the lysates were centrifuged at 3,700 x g for 20 minutes at room temperature. Iodixanol fractions were prepared as detailed in table 5. Iodixanol fractions were layered as shown in figure 2.3. The lysates were added to the top of the iodixanol gradients and the tubes sealed. The gradients were centrifuged at 59,000 x g for 1 hour and 30 minutes at 20 °C using an Optima XE-90 Ultracentrifuge. Following centrifugation, an 18G needle was used to pierce the side of the tube and draw up the 40% iodixanol fraction (containing the AAV). The fractions were placed in 15 mL falcon tubes and stored at 4 °C until

purification. To purify the AAV, Amicon 100K filters were prepared by adding 5 mL of 1xPBS and centrifuging at 3,000 x g for 15 minutes at 20 °C. 5 mL of 1x PBS was added to each of the fractions and the fractions applied to the filter. The samples were centrifuged at 3,000 x g at 20 °C until the volume in the filter reduced to ~500 µl. 15 mL of 1xPBS was added to the filter and the samples were centrifuged at 3,000 x g at 20 °C until the volume reduced to ~500 µl. This was repeated for a total of 3 washes. On the final wash, the volume of sample was reduced to between 250 and 500 µl. This was aliquoted and the filter washed with 1xPBS to collect any residual AAV. The process of AAV production is summarised in figure 2.1. AAV was stored at -80 °C until use.

Fraction	Iodixanol	5M NaCl	5X PBS-MK	H_2O	Phenol Red
15%	4ml	3.2ml	3.2ml	5.6ml	-
25%	5ml	-	2.4ml	4.6ml	20µl
40%	6.7ml	-	2ml	1.3ml	-
60%	10ml	-	-	-	20µl

Table 5. Preparation of Iodixanol Columns.

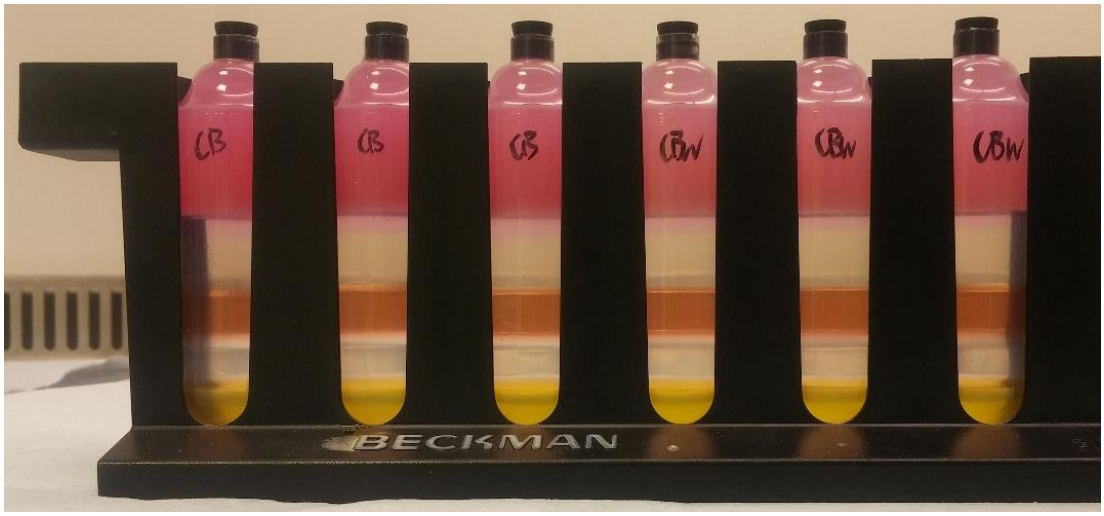

Figure 2.3. Iodixanol Columns. The prepared iodixanol gradients, with lysate loaded, prior to centrifugation. From bottom, the yellow fraction is 60% iodixanol, then 40%, 25% and 15%.

10 µl of each concentrated virus sample and each wash sample were added to 2 µl of 5X loading buffer (National Diagnostics, Cat#EC-887) and left for 30 minutes at room temperature. The samples were added to a pre-cast 10% Criterion Tris-HCl SDS-Gel (Bio-rad, Cat#345-0100) and ran at 100 V for 2 hours. 10 µl of BLUeye Pre-Stained Protein Ladder (Geneflow, UK) was loaded into one well for reference. The SDS-Gel was stained by incubation in EZBlue™ (Sigma Aldrich, Cat#G1041) for 1 hour at room temperature. Imaging of the stained gel was performed using the LiCor Odyssey FC System and Image Studio Lite Software.

2.15 Quantitative PCR

AAV titres were determined using quantitative PCR (qPCR). The primers used were directed to the bovine growth hormone polyA sequence (shown in table 1). 1 µl of AAV

sample was incubated with DNase1 for 30 minutes at 37 °C to digest any contaminating free DNA. Denaturation of the DNase1 and the AAV capsid was performed at 90 °C for 10 minutes. The DNAse1 digested sample was diluted 1:10 with molecular-grade water. 1 µl of diluted sample was added to 1 µl of forward primer (at 2 µM), 1 µl of reverse primer (at 2 µM), 2 µl of molecular-grade water and 5 µl of iTaq™ Sybr Green Mastermix (Bio-rad, Cat#1725121). Samples were run on the qPCR cycler as follows: 95 °C for 3 minutes followed by 40 cycles of 95 °C for 10 seconds, 55 °C for 30 seconds. Melt curves were generated by heating samples to 65 °C for 5 seconds then 95 °C for 5 seconds.

Primer Name	Sequence	Direction	Melting Temperature (°C)
SWClnREP1F1	5'-TTGGATCCGCGGCCGCTAGCTTGATATCGAAT-3'	Forward	72.3
SWClnREP1R1	5'-ATAAGCTTGAGCTCGATATCGAATTCGAATCGA-3'	Reverse	66
SWClnVMD2F7	5'-CAGCGGCCGCAGCTTGGTACCGCCACCATGAC-3'	Forward	78.2
SWClnVMD2R7	5'-TCGAGGAGCTCTTAGGAATGTGCTTCAT-3'	Reverse	65.5
SWSeqCAGR2	5'-CCGCCGCGCGCTTCGCTTTTT-3'	Reverse	66.6
SWSeqCAGR4	5'-GAGAGTGAAGCAGAACGT-3'	Reverse	51.8
SWSeqCAGR6	5'-CGTGTGACCGGCGGCTCTAGA-3'	Reverse	66.4
SWSeqCAGF7	5'-AATCAGAGCGGCGCGCTCCGAAAGTTT-3'	Forward	71.1
SWSeqCAGF9	5'-TGATTAACCCGCCATGCTACTTA-3'	Forward	59.7
SWSeqCAGF10	5'-GTTAATGATTAACCCGCCATGCT-3'	Forward	59.7
SWSeqCAGF11	5'-AGTTAATGATTAACCCGCCATGC-3'	Forward	59.7
SWSeqWPRER1	5'-GGGGAGGCGGCCCAAAGGGA-3'	Reverse	67.6
SWSeqWPREF2	5'-TACGCTATGTGGATACGCTGC-3'	Forward	57
PFR3	5'-CGGGAGAAGGAGCCTAAGCGG-3'	Reverse	64.6
P15	5’-GGCGGCTCTAGAGCCTCTGCTAA-3’	Forward	65.9
RC1	5'-TAGGAATGTGCTTCATCCCT-3'	Reverse	55.9
RC2	5’-TCACCTGGTCCCAAGAAGT-3’	Reverse	57.7
FW3	5'-GTCGACAGGAATTTGCAG-3'	Forward	53.8
20F	5’-CCAGCCATCTGTTGTTTGCC-3’	Forward	60
91R	5’-GAAAGGACAGTGGGAGTGGC-3’	Reverse	60.6

Table 6. Primer Sequences. All primers were designed in Geneious R7, using Primer 3 software.

2.16 Plasmid Transfection for Transgene Assessment

Plasmid transfections, for transgene assessment, were performed using LT1 Transfection Reagent (Geneflow, Cat#E7-0004). HEK293 cells were seeded in 3 ml of culture media (see table 2), at $3.0x10^5$ cells/well, in 6-well tissue culture plates. The cells were incubated at 37 °C (with 5% CO_2) for 24 hours. 7.5 µl of LT1 Transfection Reagent was added to 250 µl of serum-free media per well. 2.5 µg of plasmid DNA was added to each mix and the mixes were incubated at room temperature for 30 minutes. The media was aspirated from the HEK293 cells in the wells and 3 ml of fresh culture media was added. The transfection mix was added, dropwise, to the wells. The cells were left to incubate at 37 °C (with 5% CO_2) for 48 hours before harvesting.

2.17 AAV Transduction for Transgene Assessment

HEK293 cells were seeded in 3 ml of culture media (see table 2), at $6.0x10^5$ cells/well, in 6-well tissue culture plates. The cells were incubated at 37 °C (with 5% CO_2) for 24 hours. AAV samples were diluted to 5000 MOI in 1 ml of culture media. The media was aspirated from the HEK293 cells in the wells and the 1 ml of diluted AAV was added to the cells. 2 ml of culture media was added to the wells to make the volume up to 3 ml per well. The cells were left to incubate at 37 °C (with 5% CO_2) for 5 days before harvesting

2.18 Patch-Clamping HEK293 Cells

Media was aspirated from HEK293 cells and 100 µl of Trypsin-EDTA was added to the cells. After incubation at 37 °C (with 5% CO_2), cells were harvested in 1.4 ml of culture media (total volume of 1.5 ml). 100 µl of re-suspended cells was added to poly-L-lysine (Sigma Aldrich, Cat#P8920) coated glass coverslips and incubated at 37 °C (with 5% CO_2) for at least 8 hours to allow cells to settle onto the coverslips. Coverslips were placed in a chamber which was filled with an external recording solution. In experiments designed to analyse differences in chloride conductance between HEK293 cells transduced with AAV-*BEST1* vectors and controls, the external solution contained: 140 mM NaCl, 2 mM $CaCl_2$, 1 mM $MgCl_2$, 10 mM HEPES, 10 mM glucose and 30 mM mannitol (osmolality = 339 mOsm/kg). In experiments designed to show that conductances measured were due to movement of chloride ions, the NaCl in the external solution was replaced with 140 mM of sodium gluconate ($NaC_6H_{11}O_7$) and the osmolality was adjusted to 339 mOsm/kg with mannitol. The external solution was adjusted to pH7.4 with 2 M NaOH. Micropipettes were pulled from boroscillate glass capillaries (World Precision Instruments, Cat#1B150F-4) with a Narisage pipette puller. These were filled, via a Microfil microfilament (World Precision Instruments, Cat#MF28G67-5), with an internal solution containing: 20 mM CsCl, 10 mM EGTA, 7.2 mM $CaCl_2$, 2 mM $MgCl_2$, 10 mM HEPES, 10 mM glucose, 110 mM CsOH and 110 mM aspartic acid (osmolality = 317.6 mOsm/kg). The internal solution was adjusted to pH7.2 with 1 M CsOH. Micropipettes were attached to the headstage of patch-clamp rig and lowered into the external buffer. Micropipettes giving pipette resistances of 2.5 - 4.0 MΩ, following application of positive pressure via a mouthpiece, were lowered onto

the membrane of single cells on the coverslip. Upon the appearance of a ‘dimple’ in the cell membrane, the positive pressure was released to facilitate the formation of a ‘giga-seal’ between the micropipette and the cell membrane. Short, sharp applications of negative pressure were applied via the mouthpiece to gain access to the cell interior. The cell/micropipette was left in this configuration for ~30 seconds, to allow the internal solution to equilibrate with the cell interior, before running the voltage protocol. Cell membrane potential was held at -50 mV before being stepped from -120 mV to +80 mV in 20 mV increments. The amount of current required to change the membrane potential to each of these increments was measured. In experiments designed to analyse differences in chloride conductance between HEK293 cells transduced with AAV-*BEST1* vectors and controls, measurements were taken with pClamp 10 software, through a Dell Inspiron computer, using an Axopatch 200B amplifier and a Digidata 1440 digitiser (shown in figure 2.4). In experiments designed to show that conductances measured were due to movement of chloride ions, measurements were taken using an Axopatch Multiclamp 700B amplifier.

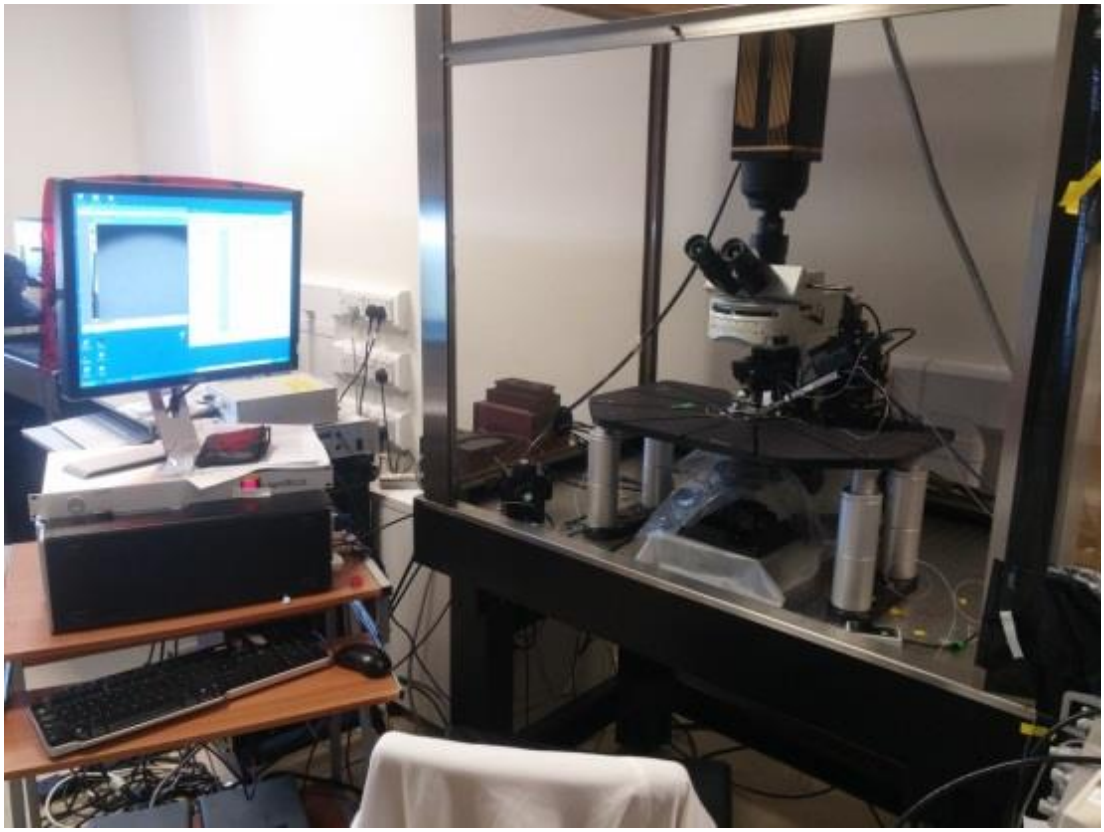

Figure 2.4. Whole-Cell Patch Clamping Set-up.

2.19 C57BL/6J Mice

All animal experiments were performed in compliance with the ARVO Statement for the Use of Animals in Ophthalmic and Vision Research and UK Home Office guidelines. C57BL/6J mice were ordered from the Jackson Laboratory. Animals were kept in individually ventilated cages in the Biomedical Services facility at the John Radcliffe Hospital, Oxford. The animals followed a 12-hour light/12-hour dark cycle, with regular food and water replacement. Animals that had undergone procedure were monitored in accordance with UK Home Office guidelines.

2.20 Sub-retinal Injections in Mice

Anaesthetic was prepared by mixing 0.8 ml Vetalar™ (100 mg/ml, Zoetis UK ltd, London, UK), 0.5 ml Rompun® (Bayer, Cat# 81099987) and 8.7 ml normal saline (Steripod, Cat#501000) in a 50 ml falcon tube (referred to as 'induction mix' from here). Mice were anaesthetised via intra-peritoneal injection with 1ml/10g of the induction mix and observed until unconscious. The following eye-drops were applied sequentially: Tropicamide, Phenylephrine Hydrochloride (both for dilation of the pupil) and Proxymetacaine Hydrochloride (for topical anaesthesia). All eye drops were bought from Bausch & Lomb. Each eye drop was left for 30 seconds before any further drops or fluids were applied. The anaesthetised mice were then placed on a foam platform and observed under a Leica operating microscope (Leica Biosystems, Newcastle Upon Tyne, UK). A drop of Viscotears® was applied to the eye, followed by a round coverslip to give a clear view of the fundus. Sub-retinal injections were performed using a Nanofil subretinal injection kit (World Precision Instruments, Hitchin, UK) with a 34 gauge metal needle.

2.21 Optical Coherence Tomography

Mice were anaesthetised, via intraperitoneal injection, using the induction mix described in section 2.20. The eyes were dilated, for 30 seconds, using a 1:1 mix of Tropicamide and Phenylephrine Hydrochloride eye drops. Hypromellose was added to the eye (to prevent the eye drying out and developing a cataract) and a round coverslip was placed over the eye to give a clear view of the fundus. The mouse was placed on an

improvised platform which was attached to a Heidelberg SPECTRALIS and OCT machine (shown in figure 2.5). The camera was aligned relative to the pupil by, an 820 nm diode laser, and brought into focus manually. Eyes were imaged using a 30 degree lens. Infared (IRAF) and Blue Autofluoresence (BAF) were taken first with the fundus camera focussed on the confocal plane of highest reflectivity. To obtain the OCT image, the focus was shifted to the vessels behind the retina. Anular, box and radial scans were taken, centred on the optic nerve. The mouse was adjusted manually when switching eyes. Segmentation of the retinal layers was performed using the Heidelberg Eye Explorer software. Retinal and outer nuclear layer (ONL) thickness measurements were taken over the whole retina and averaged.

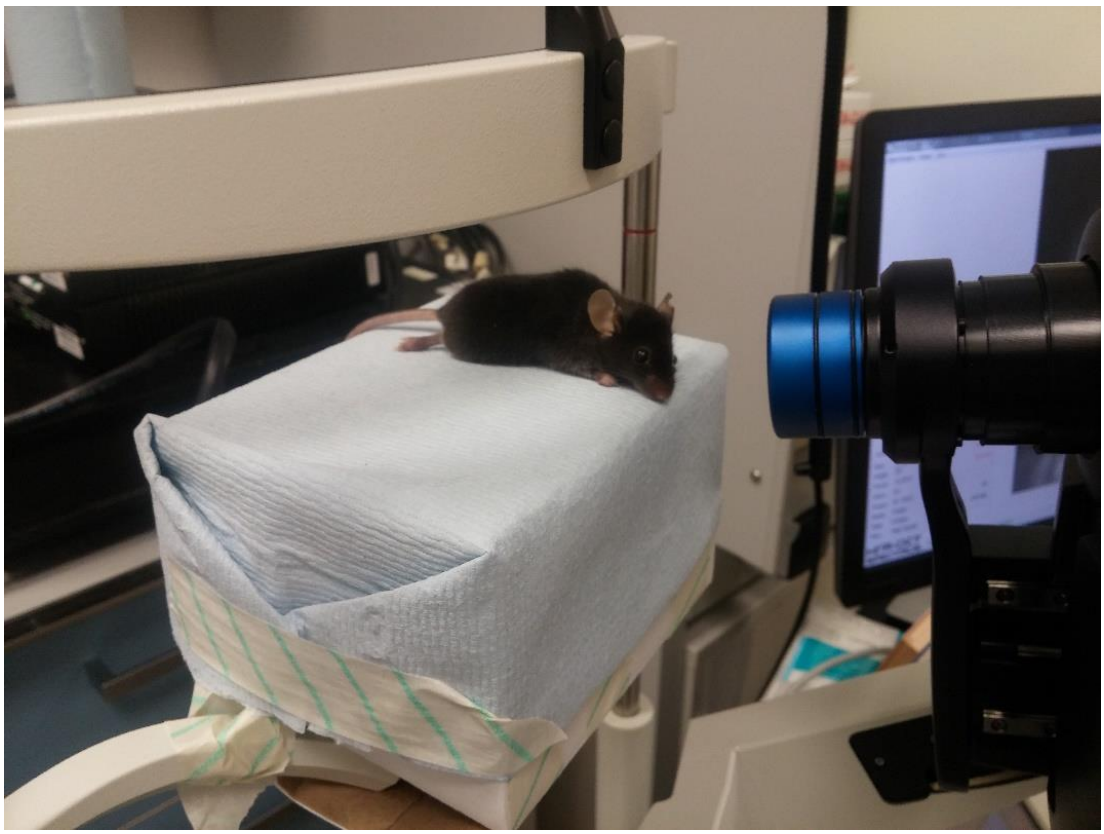

Figure 2.5. Optical Coherence Tomography Set-up.

2.22 Harvesting Mouse Eyes for Assessment

Mice were culled in accordance with schedule 1 of the Home Office Animal Welfare Act. Eyes were taken post-mortem by gripping the optic nerve and retroocular muscles at the base of the muscle cone with tweezers and performing a clean pull. The eyes were placed in a dish containing 1xPBS and viewed under a Leica EZ4 table-top dissection microscope. The cornea was punctured using a 21 gauge needle to release the intraocular pressure and provide an entry point for the dissection scissors. The cornea was excised and the lens was removed with tweezers. Excess connective tissue was removed using the dissection scissors. In cases where the eyes were taken for western blot, the protocol detailed in section 2.24 was followed. In cases where the eyes were taken for cyrosectioning and immunohistochemistry, the protocol in section 2.25 was followed.

2.23 Western Blot

For HEK293 cells in culture, cells were treated with 1xTrypsin-EDTA (Sigma Aldrich, Cat#T4549) and incubated at 37 °C for 5 minutes. Cells were then harvested in ~1.5 ml culture media in 1.5 ml tubes and centrifuged at ~1000xg for 10 minutes at 4 °C. The culture media was removed and the cell pellet was re-suspended in 1 ml of 1xPBS as a wash step. The tubes were centrifuged at ~1000xg for 10 minutes at 4 °C. The 1xPBS was removed and the cells were lysed in Radio-immunoprecipitation assay (RIPA)

buffer (Sigma Aldrich, Cat#R0278-50ML) using freeze-thaw fractionation. This consisted of three cycles where the samples were frozen at -80 °C for 15 minutes and then thawed at room temperature.

When preparing murine eyes for western blot, the eyes were added to RIPA upon removal from the animal. 125 µl of RIPA buffer was used per eye. Where the retina and the eye-cup were separated, 100 µl of RIPA was used. Samples were frozen instantly on dry ice and stored at -80 °C until use. Once thawed, the tissue was subjected to mechanical disruption using a hand-held pestle motor and pestle. Samples were then subjected to freeze-thaw fractionation as described above.

Samples were centrifuged at 14,000 g for 30 minutes at 4°C. The supernatant was transferred to fresh tubes on ice. Protein concentration was determined using the Pierce BCA Protein Assay (Thermo Scientific, Cat#23227). A total of 30 µg of each sample was denatured in protein loading buffer (National Diagnostics, Cat#EC-887) at room temperature for 30 minutes and loaded onto pre-cast Criterion® SDS gels (Bio-Rad, Cat#345-0010) and run at 100V for ~2 hours. Protein was transferred to a PVDF membrane (Bio-Rad. Cat#170-4157) using the Bio-Rad Transblot® Turbo Transfer System, via the 'Mixed Molecular Weight' programme. Membranes were blocked in 1% BSA in 1xTBS-T at room temperature for 1 hour. Membranes were incubated with primary anti-bodies, diluted in 1% BSA, at room temperature for 1 hour. The membranes were washed in 1xTBS-T and then incubated with secondary anti-bodies, diluted in 1xTBS-T, at room temperature for 1 hour. The membranes were washed in 1xTBS-T and incubated with Clarity™ Western ECL Substrate (Bio-Rad, Cat#170-

5060) at room temperature for 2 minutes. Membranes were visualised using the LiCor Odyssey-FC system and analysed using the LiCor Image Studio software.

2.24 Embedding Mouse Eyes

Dissected mouse eyes were fixed in 4% paraformaldehyde (Thermo Scientific, Cat#28906) for 1 hour at room temperature. To dehydrate the eyes, prior to freezing, the eyes were washed in 1xPBS and placed in a 10% sucrose solution (Sigma Aldrich, Cat# S0389), at room temperature, until the sample was observed to have sunk to the bottom of the container. The eye was then placed in a 20% sucrose solution, at room temperature, until the sample was observed to have suck to the bottom of the container. Finally, the sample was placed in a 30% sucrose solution, at room temperature, until the sample was observed to have sunk to the bottom of the container. The eyes were then observed under the dissection microscope, dried with some blue roll and were filled, via a 21 gauge needle, with Optimal Cutting Temperature (O.C.T) compound. A make-shift mould was made by lining a well of a 1.5 ml tube rack with aluminium foil. The eye was placed at the bottom of this mould and the mould was filled with O.C.T. The dissection microscope was used to observe that the eye was in a ‘C’ orientation in the mould. A beaker of isopentane was super-cooled on dry ice and the O.C.T moulds were held in the isopentane with forceps to snap-freeze the eye and reduce the formation of crystals. These O.C.T cryomoulds were stored at -80 °C until use.

2.25 Cyrosectioning Mouse Eyes

A Cyrotome FSE cryostat was used to take sections of the mouse eyes. The cryostat was set to -23 °C (both chamber and specimen) and allowed to cool down before starting. The O.C.T cryomoulds were attached to a platform by adding more O.C.T to the platform and freezing the cyromould to the platform by placing it in the cryostat. The platform was mounted onto the cryobar and a scalpel blade was anchored in place. 18 μM sections were taken and mounted on poly-L-lysine coated slides. 5-6 sections were taken per slide. Slides were left at room temperature for 24 hours to let the sections bond to the slide. Slides were stored, long-term, at -80 °C.

2.26 Immunohistochemistry (IHC)

Slides were thawed at room temperature for 1 hour. A hyrdrophobic barrier was drawn around the slides with an ImmEdge™ pen. Sections were permeabilised in 1% Tween-20 (diluted in 1xPBS) for 20 minutes at room temperature. Sections were blocked in 1% BSA (diluted in 1xPBS) with 10% serum for 1 hour at room temperature. Sections were incubated in the primary antibodies (diluted in 1xPBS containing 1% BSA and 2% serum) overnight at 4 °C. Slides were placed in a rack and washed in 0.05% Tween-20 (diluted in 1xPBS) for 10 minutes at room temperature. This wash step was repeated for a total of 4 washes. Sections were incubated in the secondary antibodies (diluted in 1xPBS containing 1% BSA and 2% serum) for 2 hours at room temperature (in the dark). Slides were placed in a rack and washed in 0.05% Tween-20 (diluted in 1xPBS)

for 10 minutes at room temperature. This wash step was repeated for a total of 3 washes. Hoecsht was diluted 1:10,000 in 1xPBS and the slides were immersed in this buffer for 10 minutes at room temperature to stain cell nuclei. Prolong Diamond (Thermo Scientific, Cat# P36961) was added to the sections followed by a coverslip. Sections were left at room temperature overnight to cure.

2.27 Confocal Microscopy

Confocal microscopy was performed using a Leica LSM-700 system with Zen software. Z-stacks were set at the limits of nuclei detection. Alexa fluor 488, 568 and 647 were excited using 488 nm argon (emission 494-542 nm) and the 543 and 647 nm HeNe lasers (emission 549-712 nm), as appropriate. Optimal slice size for the z-stack was determined by the Zen software. Images were taken at 1024x1024 pixels. Image analysis was performed using the Zen Lite software.

2.28 Immunocytochemistry (ICC)

For cells in culture, the media was removed and the cells were fixed in 4% PFA for ~15 minutes at room temperature. The cells were washed with 1xPBS and permeabilised in 0.1% Tween-20 (diluted in 1xPBS) at room temperature for 10 minutes. The cells were blocked by incubation in 5% serum (diluted in 0.05% Tween-20) for 30 minutes at room temperature. The blocking solution was removed from the cells and the cells were then incubated in the primary antibody (diluted in 2% serum) for 1 hour at room

temperature. The cells were washed in 0.05% Tween-20 for 5 minutes at room temperature. This was repeated for a total of 3 washes. The cells were incubated in the secondary antibody (diluted in 2% serum) for 30 minutes at room temperature. The cells were washed in 0.05% Tween-20 for 5 minutes at room temperature. This was repeated for a total of 3 washes. A final 10 minute was with Hoechst (diluted 1:10,000 with 1xPBS) was performed to stain the nuclei. Prolong Diamond was added to the sections followed by a coverslip. Sections were left at room temperature overnight to cure.

Target Epitope	Species Raised In	Supplier	Catalogue Number
Human Bestrophin-1	Mouse	Abcam	ab2182
β-actin	Rabbit	Abcam	ab8227
Rhodopsin	Rabbit	Abcam	ab34324
Mouse IgG	Donkey	Abcam	ab98799
Rabbit IgG	Donkey	Abcam	ab98509
Mouse IgG	Donkey	Life Technologies	A-21202
Mouse IgG1	Goat	Life Technologies	A-21124
Rabbit IgG	Donkey	Life Technologies	A-10037

Table 7. List of Antibodies

2.29 Immuno-precipitation

HEK293 cells were transfected and harvested as described in sections 2.16 and 2.24. 200 µl of protein sepharose G beads (Sigma Aldrich, Cat#P3296-1ML) were incubated with 10 µl of primary antibody for 1 hour at room temperature with gentle agitation using a rotor. This bead/antibody slurry was centrifuged at 3000 g for 5 minutes at room temperature and supernatant was removed using a micropipette. Following on from

harvesting in RIPA buffer, 200 µl of sample was added to the beads and incubated at 4 °C overnight, with gentle agitation using a rotor. The beads were centrifuged at 3000xg for 2 minutes at room temperature and the supernatant was removed. The beads were washed by being re-suspended in 0.1% Tween-20 (diluted in 1xPBS) before being centrifuged at 3000xg for 2 minutes at room temperature. The wash steps were repeated for a total of 3 times. The bound protein was eluted by boiling the samples at 95 °C for 10 minutes in 50 µl of Laemmli buffer (Bio-Rad, Cat#1610737). The sample was centrifuged at 3,000xg for 2 minutes at room temperature. The supernatant (containing the eluted protein) was transferred to a fresh 1.5 ml tube. 5 µl of sample was loaded onto an SDS-PAGE gel for western blot analysis (as described in section 2.24) and a further 45 µl of sample was loaded onto an SDS-PAGE gel for staining with EZBlue™ (coomassie blue) as described in section 2.14. Appropriate bands were excised from the SDS-Gel and were taken for LC/LC-MS analysis.

2.30 Gel Digestion for Liquid Chromatography Tandem Mass Spectrometry Analysis

Gel pieces were incubated with 150 µl of 50% ACN, 50 mM TAE at 37 °C until de-stained. The samples were then incubated with 10 mM TCEP for 30 minutes at room temperature. The buffer was removed, the samples were washed with 200 µl of 100% ACN and were left to dry. 200 µl of 50 mM 2-Chloroacetamide (diluted in 100 mM TAE) was added to the samples and left to incubate at room temperature for 30 minutes in the dark. The 50 mM 2-Chloroacetamide was removed and the samples were washed with 200 µl of 100% ACN and were left to dry. 0.25 µg of trypsin (diluted in 50 mM

TAE) was added and the samples were left to incubate at 37 °C overnight. Following the incubation, the supernatants were transferred to fresh tubes and the gel samples were rinsed with 10% FA. The FA was removed and added to the supernatants. The samples were then taken for LC-MS/MS analysis.

2.31 Liquid Chromatography Tandem Mass Spectrometry Analysis

The samples were loaded onto an Ultimate 3000 UHPLC system (Thermo Fischer Scientific) for peptide separation. The peptides were electrosprayed directly into a QExactive Mass Spectrometer (Thermo Fischer Scientific) through an EASY-Spray nano-electrospray ion source (Thermo Fischer Scientific). A C18 PepMap100 pre-column (300 µm i.d. x 5 mm, 100 Å, Thermo Fischer Scientific) was used to trap the peptides with 0.1% formic acid (diluted in RO water) at a pressure of 500 bar. The peptides were separated on an in- house packed analytical column (75 µm i.d. packed with ReproSil-Pur 120 C18-AQ, 1.9 µm, 120 Å, Dr.Maisch GmbH) using a linear gradient (length: 30 minutes, 7% to 28% solvent B (0.1% formic acid in acetonitrile), flow rate: 200 nL/min). The raw data was acquired on the mass spectrometer in a data-dependent mode (DDA). Full scan MS spectra were acquired in the Orbitrap (scan range 350-2000 m/z, resolution 70000, AGC target 3e6, maximum injection time 50 ms). After the MS scans, the 10 most intense peaks were selected for HCD fragmentation at 30% of normalised collision energy. HCD spectra were also acquired in the Orbitrap (resolution 17500, AGC target 5e4, maximum injection time 120 ms) with first fixed mass at 180 m/z. The raw data files generated were processed using MaxQuant 1.5.0.35, integrated with the Andromeda search engine. For protein group identification, peak

lists were searched against human database (UniProt) as well as a list of common contaminants by Andromeda. Trypsin with a maximum number of 2 was chosen. Acetylation and Oxidation were used as variable modifications. Carbaminomethylation was set as a fixed modification. PSM false discovery rate (FDR) was set at 0.01.

2.32 Statistics

Statistics were performed using Graphpad Prism 7.0. Statistical significance was defined as $p<0.05$. Further details of statistical test used are provided in the relevant areas of the manuscript.

Chapter 3. AAV Production and Comparison of Bestrophin-1 Expression *in vitro.*

3.1 Chapter Introduction

AAV2 has been shown to have high tropism for the RPE and has also been used successfully in clinical trials for IRDs caused by mutations in RPE-specific genes (*112, 113*). The chicken β-actin promoter with CMV enhancer (CAG promoter) has been used to drive transgene expression in a recent clinical trial for choroideremia (*110, 111*) which has shown good efficacy after ~3.5 years. The WPRE has been shown to increase the level of transgene expression by increasing the availability of transgene mRNA for translation (*172*). Two vectors were cloned, both expressing the BEST1 transgene under the control of the CAG promoter, but with one vector containing the WPRE element. These vectors were assessed in vitro for their ability to produce Bestrophin-1 as analysed by western blot and immunocytochemistry.

3.2 Chapter-specific Methods

To clone the BEST1 transgene under the control of the CAG promoter, it was decided to use a plasmid backbone expressing REP1 under the control of the CAG promoter and replace the REP1 transgene with the BEST1 transgene. The plasmid diagram for the REP1 plasmid is shown in figure 3.1 with the regions either side of the transgene highlighted. Due to the lack of appropriate restriction sites available, a strategy was designed to insert two appropriate restriction sites that did not cut within the BEST1 transgene or the backbone of the REP1 plasmid. To do this, primers were designed containing the desired restriction sites (NotI and SacI), along with other restriction sites

that allowed the re-insertion of the REP1 transgene back into the original vector following PCR amplification, thus giving a vector containing the desired NotI and SacI restriction sites flanking the REP1 transgene. Following this, the BEST1 transgene (contained in a separate plasmid vector) was amplified using primers containing the NotI and SacI restriction sites. Digestion of the modified REP1 plasmid and amplified BEST1 transgene allowed the ligation of the BEST1 transgene into the plasmid backbone, giving pCAG.hBEST1.WPRE.pA. Removal of the WPRE was done by digestion with ClaI to produce a pCAG.hBEST1.pA vector.

The resulting plasmids were packaged into AAV2 capsids using the method detailed in chapter 2.10-2.13. These were then analysed by SDS-PAGE (for capsid size) and qPCR (for vector genome particles) to determine viral titre.

The rAAV vectors were used to transduce HEK293 cells in vitro and analysed for bestrophin-1 expression. Western blots were used to determine protein size and expression level. Immunocytochemistry (ICC) and confocal microscopy was used to visualise protein localisation.

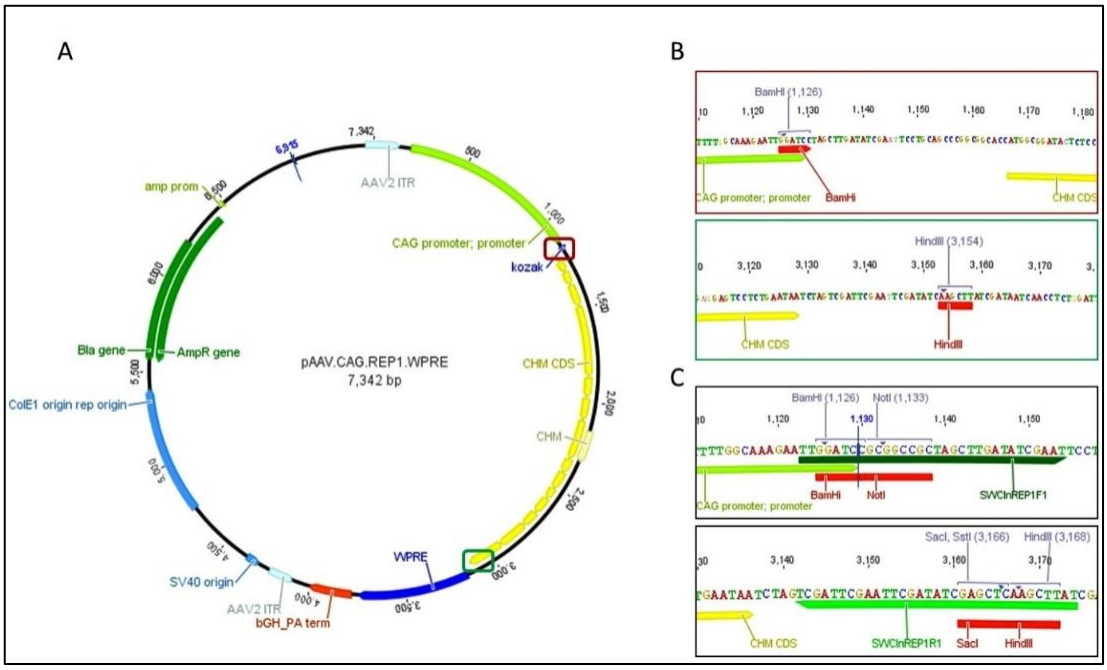

Figure 3.1. Primer Design for Inserting Restriction Sites into pAAV.CAG.REP1.WPRE. The plasmid map for pAAV.CAG.REP1.WPRE is shown in **A**. BamHI and HindIII (5' and 3' of the REP1 CDS respectively) were identified to cut only once in the plasmid (**B**). Both these enzymes cut within the BEST1 CDS so are unsuitable for cloning. (**C**) Primers were designed to include NotI (5' of REP1) and SacI (3' of REP1), both of which do not cut in the BEST1 CDS or the backbone of pAAV.CAG.REP1.WPRE.

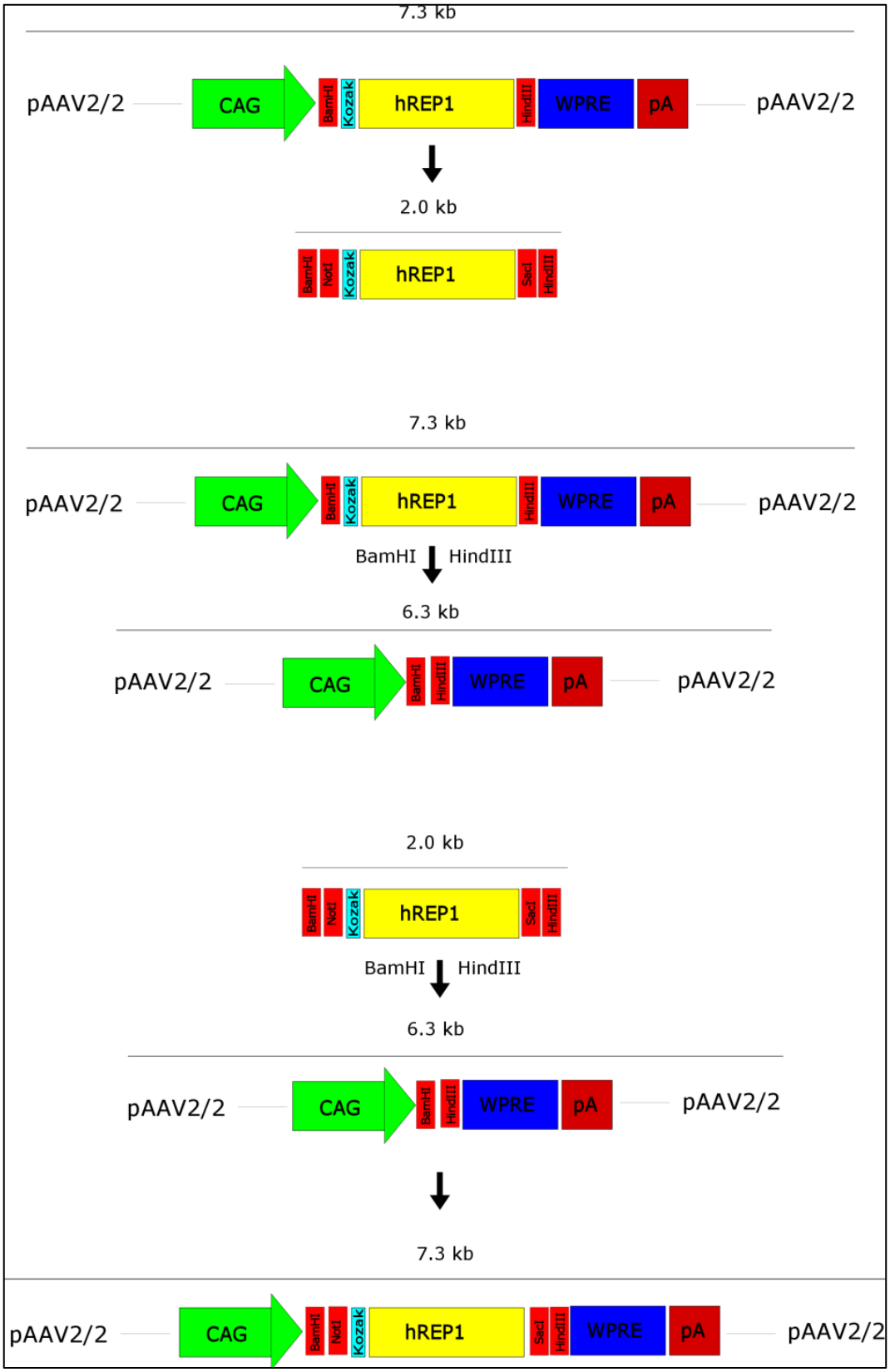

Figure 3.2. Insertion of NotI and SacI Restriction Sites into the pAAV.CAG.hREP1.WPRE Plasmid. A schematic outline of the strategy used to insert the required NotI and SacI restriction sites into the backbone plasmid.

3.3 Results

3.3.1 Cloning *BEST1* into the pAAV2/2 Backbone

Figure 3.3 shows the gels relating to the amplified *REP1* sequence and the cut pAAV2.CAG.*REP1*.WPRE construct. The *REP1* sequence was successfully amplified using the primers designed in figure 3.1. The fragments were gel extracted and pooled. Figure 3.3 shows the *REP1* fragments and the pAAV2.CAG.*REP1*.WPRE vector following digestion with BamHI and HindIII. The fragments highlighted were cut out, ligated and transformed into XL-10 gold ultracompetent cells. Colonies were picked, grown in LB and mini-prepped as described in chapter 2. The resulting plasmids were digested with XmaI, ran on an agarose gel and the results are shown in figure 3.4. The size of DNA fragments on the agarose gel suggested that the ligation reaction had not worked as the bands are the same size as the backbone fragment alone. Sequencing the precursor plasmid, however, revealed that the restriction sites (NotI and SacI) had successfully been incorporated into the vector, despite the *REP1* sequence not being present (figure 3.5). This suggests that the REP1 sequence may have recombined and been lost in the cloning procedure. Since REP1 was not in any case required for the BEST1 vector, this fortuitous event resulted in one less cloning step.

The BEST1 CDS was provided by Dr Forbes Manson and amplified using the primers in table 6 (SWClnVMD2F7 and SWClnVMD2R7). The precursor vector and the isolated *BEST1* fragment were cut with NotI and SacI, ran on an agarose gel and extracted as described previously (figure 3.6). The BEST1 fragment was ligated into the

precursor vector and transformed into XL-10 gold ultracompetent cells. Colonies were picked and processed as mentioned previously. The results of the XmaI digest are shown in figure 3.7. The pCAG.hBEST1.pA and pCAG.hBEST1.WPRE.pA constructs are shown in figure 2.2.

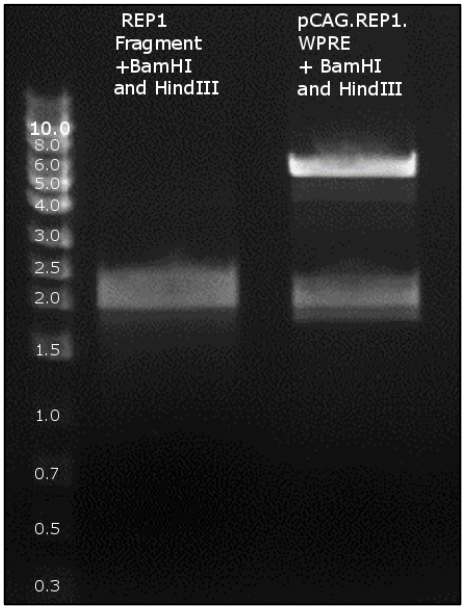

Figure 3.3. Insertion of NotI and SacI Restriction Sites into the pAAV.CAG.REP1.WPRE Plasmid-Gel. Shows the REP1 cDNA amplified from the backbone plasmid via PCR using the primers shown in figure 1 and cut with BamHI and HindIII. The pAAV.CAG.REP1.WPRE plasmid was also cut with BamHI and HindIII. These samples were gel extracted and ligated together.

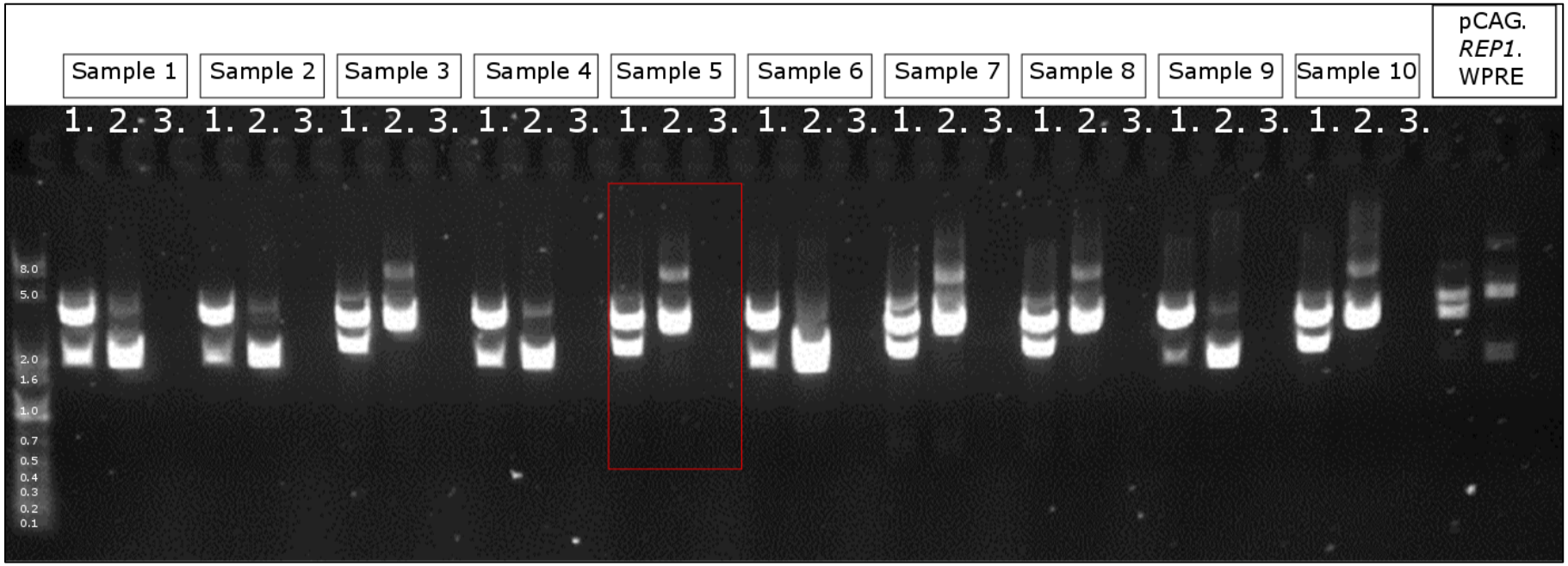

Figure 3.4. Result of Precursor Plasmid ITR Digest. Samples show band sizes that suggest that the modified REP1 fragment hasn't ligated into the backbone. Sample 5 (highlighted) was taken for sequencing as the ITR digest was judged to have been the cleanest.

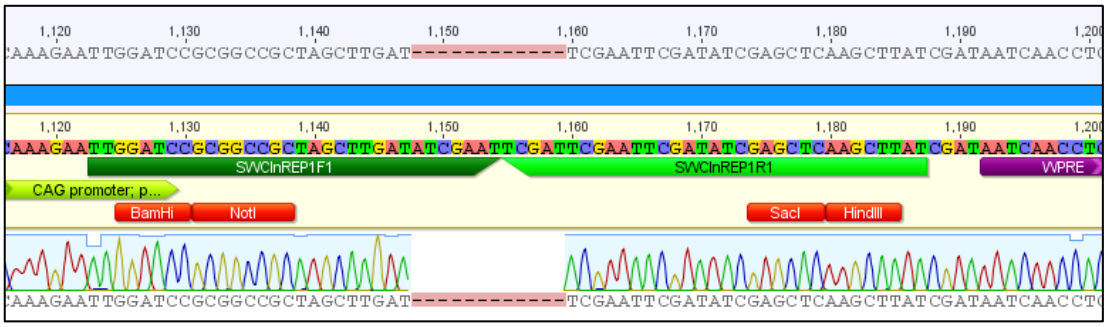

Figure 3.5. Sequencing of the precursor construct seen in figure 3.4. Sanger sequencing identified correct insertion of the required NotI and SacI restriction sites (labelled on the sequence). The expected REP1 transgene is not present, represented by the dashed lines highlighted in pink. The two primers used for the PCR reaction are also highlighted on the sequence. Image was taken using Geneious R7 Software.

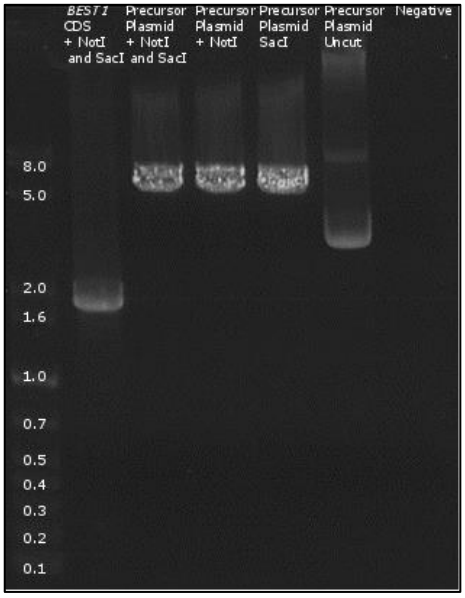

Figure 3.6. Digestion of the Precursor Backbone and PCR-amplified BEST1 CDS with NotI and SacI. Lane 1 shows the expected BEST1 CDS at ~1.7 kb. Lane 2 shows the precursor backbone at the expected ~6.0 kb. Lanes 3 and 4 show the precursor backbone linearised with NotI and SacI respectively. Lane 5 is uncut precursor plasmid showing the classic supercoiled bands. The final lane is a negative control ran with no plasmid template.

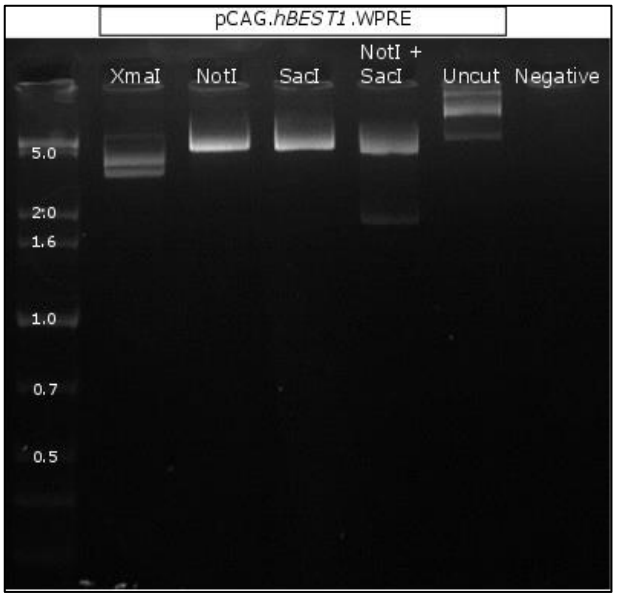

Figure 3.7. Ligated pCAG.hBEST1.WPRE Digested with XmaI and Controls. Lane 1 shows the XmaI digest giving bands at 3.9 kb and 3.1 kb. Lanes 2 and 3 are NotI and SacI digests, respectively, to linearise the plasmid, confirming the presence of both sites and showing the size of the plasmid (7.1 kb). Lane 4 is a NotI and SacI digested sample showing the presence of the *BEST1* CDS (1.7 kb). Lane 5 is an uncut plasmid control and lane 6 is the negative (no plasmid template).

To produce the pAAV.CAG.hBEST1.pA vector, pAAV2.CAG.hBEST1.WPRE.pA was digested with ClaI to remove the 'WPRE' element (see figure 3.8). The resulting construct was extracted from the agarose gel and ligated, transformed into bacteria and processed as described for pAAV.CAG.hBEST1.WPRE.pA. Sequencing of the constructs showed successful incorporation of the BEST1 transgene in both vectors and removal of the WPRE element in the pAAV.CAG.hBEST1.pA vector (Figure 3.9).

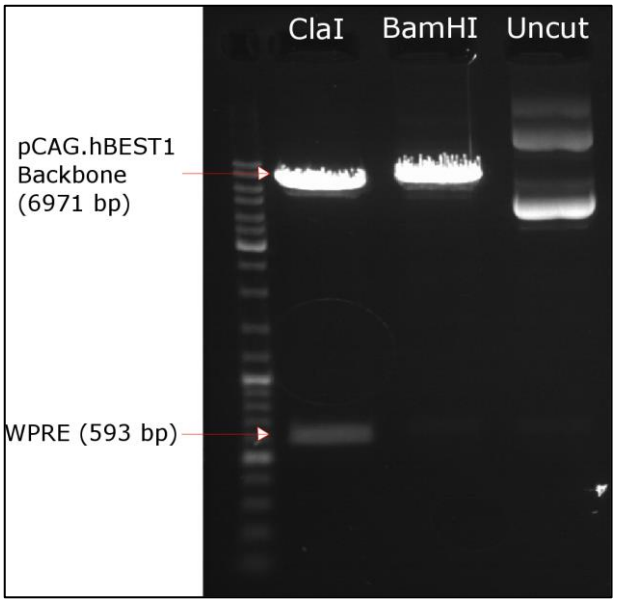

Figure 3.8. ClaI Digest of pCAG.hBEST1.WPRE. Lane 1 (ClaI) shows a ~600 bp fragment corresponding to the WPRE element. BamHI successfully linearises the plasmid (shown in lane 2). Lane 3 contains the uncut plasmid DNA ran as a control, showing the characteristic coiled and supercoiled bands.

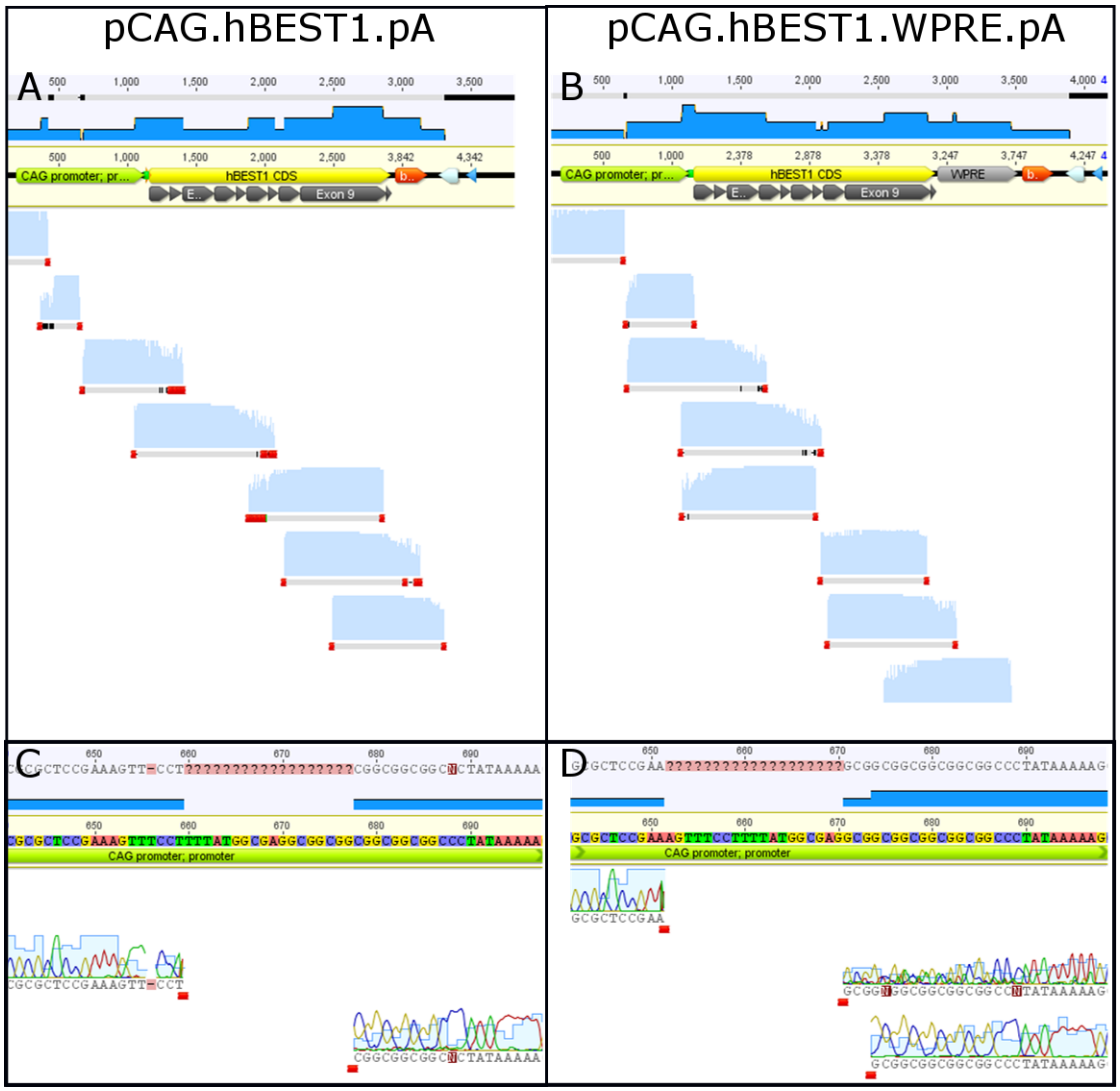

Figure 3.9. Sequencing of the hBEST1 Plasmids Prior to AAV Production. Sequencing primers all show clean reads. Reads were mapped to the reference sequences of pCAG.hBEST1.pA (**A**) and pCAG.hBEST1.WPRE.pA (**B**) and were aligned consecutively using Geneious R7 software. Coverage of both plasmids is indicated by the blue shading at the top of the image and shows that coverage is good with the exception of one region within the promoter (**C** and **D**), containing repetitive sequences. All other regions, such as the hBEST1 CDS and WPRE were covered.

3.3.2 Production of AAV2/2-*BEST1* Vectors

The pAAV2.CAG.*hBEST1*.pA and pAAV2.CAG.*hBEST1*.WPRE.pA constructs were mega-prepped and used to transfect HEK293T cells as described in chapter 2. Figure 3.10 shows the standard curves and melt curve from the qPCR testing of AAV-*BEST1* vector titre. The SDS-Page in figure 3.11 consolidates the results from the qPCR. Titres were ~5.0x10^{11} for AAV2/2.CAG.*hBEST1*.WPRE.pA and ~1.6x10^{12} for AAV2/2.CAG.*hBEST1*.pA.

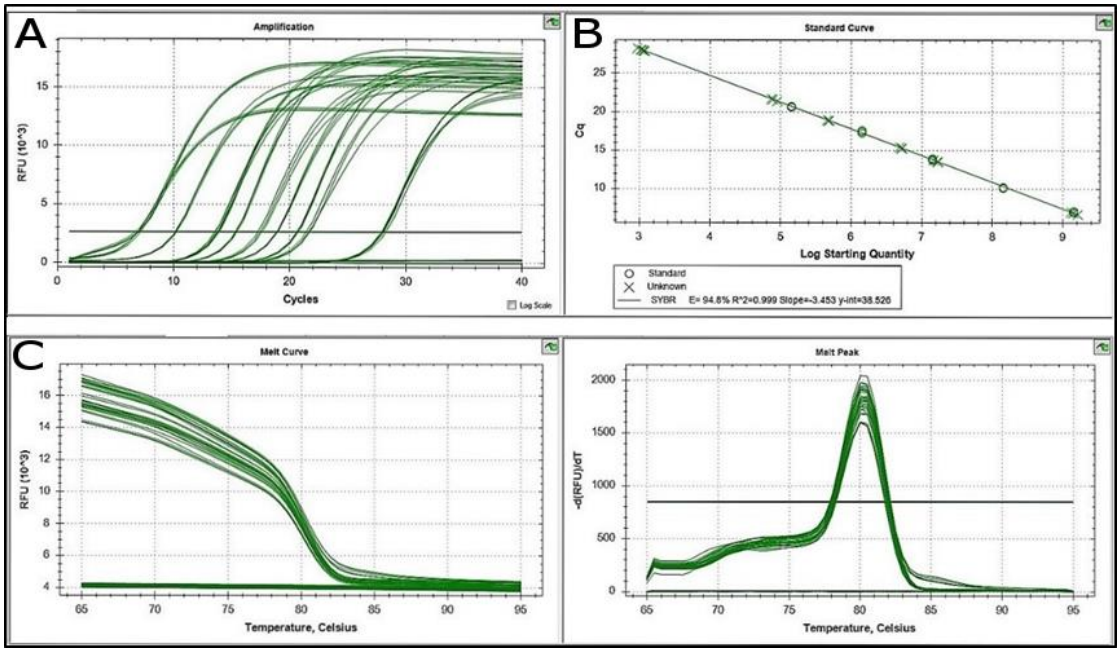

Figure 3.10. Standard Curve and Melt Curve from the qPCR titring of AAV2-BEST1. The amplification plots for the standards and denatured rAAV particles is shown in **A**.Standards ranging from 10 ng-1 pg (5 serial dilutions) were used to generate the standard curve (**B**), which shows a gradient of -3.45 and efficiency of 94.8%**.** The melt curve shows all samples peaking at ~80 °C (**C**) indicating that only one PCR product is being formed in the reaction, confirming that the primers are specific to the region of interest and are not hybridising elsewhere in the DNA construct.

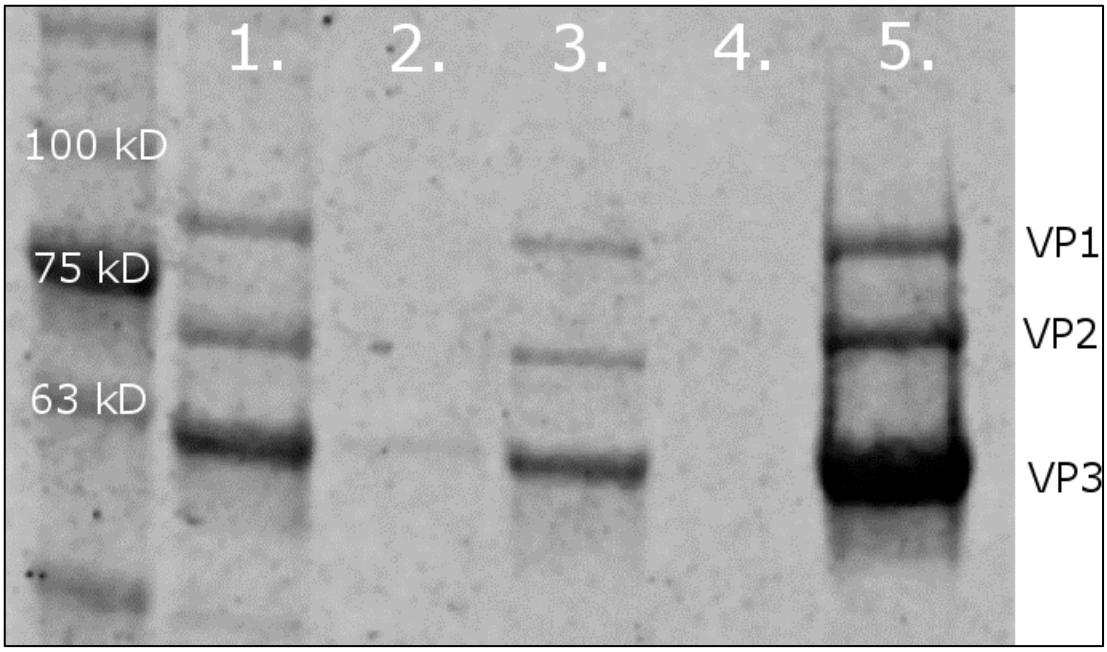

Figure 3.11. Coomassie Blue – stained SDS-PAGE Gel of AAV2-BEST1. Coomassie stained SDS-PAGE gels loaded with: 1 = AAV2/2.CAG.*hBEST1*.pA concentrate, 2 = AAV2/2.CAG.*hBEST1*.pA wash, 3 = AAV2/2.CAG.*hBEST1*.WPRE.pA concentrate, 4 = AAV2/2.CAG.*hBEST1*.WPRE.pA wash and 5 = control AAV sample (estimated at $1.0x10^{14}$). The bands seen correspond to the predicted sizes of the 3 AAV viral capsid proteins, VP1 (82 kD), VP2 (72 kD) and VP3 (62 kD). The intensity of the bands confirm the results of the qPCR titration.

3.3.3 Comparison of BEST1 Expression from AAV Vectors in HEK293 Cells.

To determine the more potent vector, both vectors were used to transduce HEK293 cells *in vitro*. The amount of bestrophin-1 produced by each vector was quantified via western blot with the antibodies listed in table 7. Figure 3.12 shows that both vectors are capable of producing bestrophin-1 in HEK293 cells. Quantification of each band showed that AAV2/2.CAG.hBEST1.WPRE.pA gave ~4-fold greater bestrophin-1 expression than AAV2/2.CAG.hBEST1.pA. A Shapiro-Wilk test for normality indicated that the data was not normally distributed (table 8), therefore the data was

analysed using a Kruskal-Wallis test with Dunn's test for multiple comparisons. This indicated a significant difference in bestrophin-1 expression levels between HEK293 cells transduced with AAV2/2.CAG.hBEST1.WPRE.pA compared to un-transduced controls. However there was no significant difference between AAV2/2.CAG.hBEST1.WPRE.pA transduced cells and those transduced with AAV2/2.CAG.hBEST1.pA (p=0.0529). Given how close this p-value is to the threshold of 0.05, a Mann-Whitley U test was used to compare these two conditions and returned a significant difference ($p<0.01$). Immunocytochemistry (ICC) (Figure 3.14) shows the bestrophin-1 expression (in green) in HEK293 cells following transduction. While some of the protein is present at the cell membrane, there is also a large amount diffuse throughout the cytosol (figure 3.15). This is consistent with plasmid transfections of bestrophin-1 in HEK293 cells (*57*, *105*).

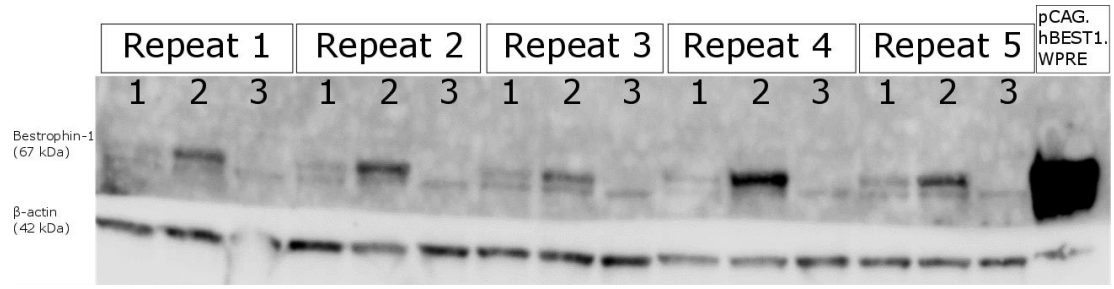

Figure 3.12. Quantification of Bestrophin-1 Expression in HEK293 Cells from Western Blots. Protein lysates were ran on SDS-PAGE gels, transferred to PVDF membranes and probed with mouse anti-hBestrophin-1 primary and donkey anti-mouse IGG secondary antibodies. Sample 1 = AAV2/2.CAG.hBEST1.pA, 2 = AAV2/2.CAG.hBEST1.WPRE.pA and 3 = Negative. Plasmid-transfected HEK293 cells were used as a positive control (+ve). Clear bands can be seen in lysates from cells transduced with the AAV-BEST1 vectors that are not seen in control lysates. A rabbit anti-β-actin primary and donkey anti-rabbit IGG secondary was used as a loading control.

Shapiro-Wilk normality test	AAV2/2.CAG.hBEST1.pA, n=9	AAV2/2.CAG.hBEST1.WPRE.pA, n=9	Un-transduced Control, n=8
W	0.9238	0.8228	0.9761
P value	0.4247	0.0371	0.941
Passed normality test (alpha=0.05)?	Yes	No	Yes
P value summary	Ns	*	ns

Table 8. Shapiro-Wilk Test for Normality for Bestrophin-1 Expression Levels in HEK293 Cells. Some values were shown to not be normally distributed using the Shapiro-Wilk Test. Therefore non-parametric tests were used to analyse the current amplitude data.

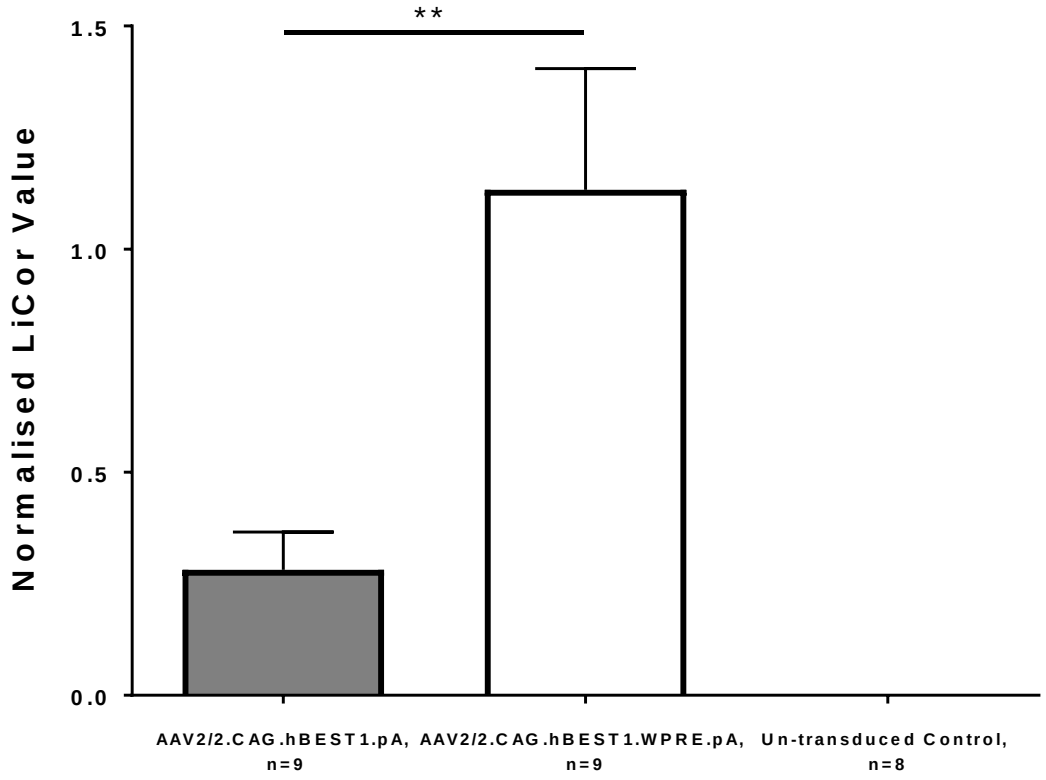

Figure 3.13. Intensity of Bestrophin-1 Expression in HEK293 Cells from Western Blots. Bands intensity was measured using the LiCor Odyssey FC system and Image Studio software. AAV2/2.CAG.hBEST1.WPRE.pA (n=9) showed ~4-fold increase in Bestrophin-1 expression over AAV2/2.CAG.hBEST1.pA (n=9) ($p<0.01$ by Mann Whitley U test)). Although Bestrophin-1 expression is seen in the AAV2/2.CAG.hBEST1.pA cells, this was not statistically significant over un-transduced cells. Error bars = ±SEM. **= $p<0.01$.

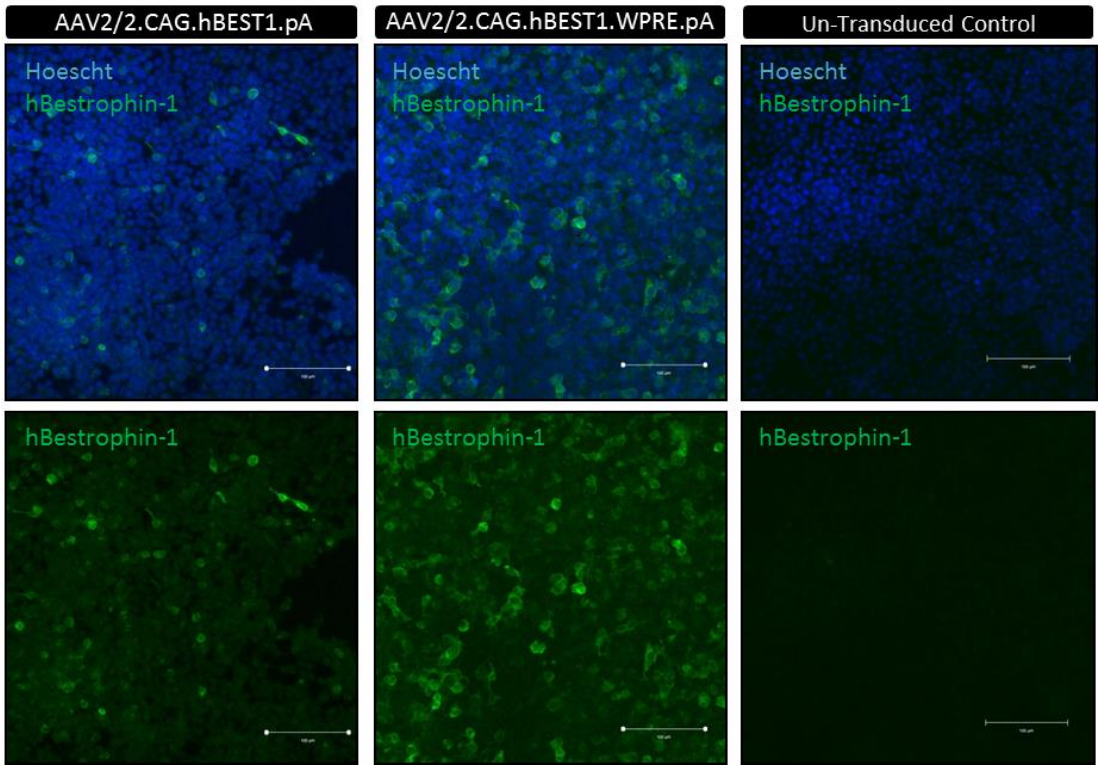

Figure 3.14. Confocal Images of HEK293 Stained for Bestrophin-1 following AAV Transduction. Bestrophin-1 was detected in HEK293 cells transduced with AAV2/2.CAG.hBEST1.pA and AAV2/2.CAG.hBEST1.WPRE.pA, with AAV2/2.CAG.hBEST1.WPRE showing the greater expression. The untransduced control HEK293 cells show no bestrophin-1 expression. Scale bars = 100 µM.

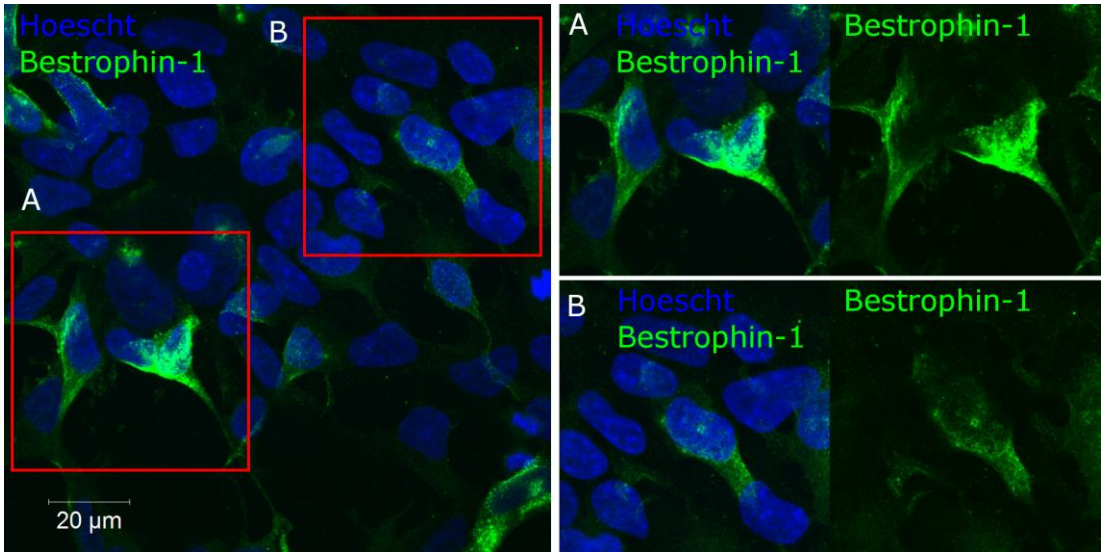

Figure 3.15. Localisation of Bestrophin-1 in HEK293 Following Transduction with AAV-BEST1 Vectors. HEK293 cells were analysed via confocal microscopy to identify the localisation of Bestrophin-1 following AAV transduction. **A** and **B** show images at 3x zoom. Removal of the Hoescht imaging indicates bestrophin-1 expression is cytosolic in **A** with some membrane localisation in **B**. Scale bars = 20 µM.

3.4 Chapter Discussion

AAV-BEST1 titres were lower than what might be expected for AAV2/2 production in HEK293T cells. The reasons for this could be procedural as the AAV production protocol has many potential sources of error. These include the health of the cells used for the production, the optimisation of the transfection procedure, the media used to culture the cells, the efficiency of the lysis procedure, the extraction of the 40% iodixanol fraction and the efficiency of the concentration procedure. It is also possible that qPCR could give inaccurate results based on the efficiency of the digestion of the AAV capsid and the quality of the standards. Another possibility is the toxicity of overexpression of bestrophin-1 in HEK293T cells. As the CAG promoter is ubiquitous, the constructs are likely to express the transgene in the cells. Overexpression of any

protein can show toxicity and, as bestrophin-1 is involved in Cl^- transport, this overexpression could have an effect on cellular ion composition. Evidence for this toxicity is provided by the lower titres of the AAV2/2.CAG.hBEST1.WPRE.pA vector (~3-fold less than AAV2/2.CAG.hBEST1.pA). As seen in this chapter, the inclusion of WPRE in the construct significantly increases the expression of the protein, which, if the bestrophin-1 protein is having a toxic effect on the cells, would increase cell death in culture.

Bestrophin-1 expression was obtained from both AAV2/2.CAG.hBEST1.pA and AAV2/2.CAG.hBEST1.WPRE.pA when these vectors were used to transduce HEK293 cells *in vitro.* The expression of bestrophin-1 was ~4 fold greater in HEK293 cells transduced with AAV2/2.CAG.hBEST1.WPRE.pA than it was in cells transduced with AAV2/2.CAG.hBEST1.pA. Following transduction, it appears that bestrophin-1 expression in HEK293 cells isn't completely localised to the membrane. Although some staining is seen at the membrane (figure 3.14), there is also a lot of staining seen throughout the cytosol. This is likely to be due to the unpolarised nature of HEK293 cells and is consistent with previous plasmid transfection experiments. ARPE19 cells (an RPE cell line) could have been used as a more appropriate model, however these cells do not express key RPE expression markers (such as BEST1 and RPE65) and therefore may not be the best system for modelling the RPE.

Chapter 4. Patch-Clamp Electrophysiology

4.1 Chapter Introduction

Having produced two AAV vectors that successfully express Bestrophin-1, to confirm the function of the protein in chloride conductance across the plasma membrane whole-cell patch-clamping was performed. Whole-cell patch-clamping measures changes in membrane potential across the plasma membrane and is the current gold standard in electrophysiology (*173*). As explained in chapter 1, Bestrophin-1 is known to function as an outwardly-rectifying chloride channel in the RPE, in response to both calcium binding and changes in cell volume (*65*, *73*). The aim of the patch-clamping experiments was, first, to confirm that AAV-mediated transfer of bestrophin-1, *in vitro*, leads to a significant increase in chloride conductance as seen in transient transfections. Second, to determine the optimal vector construct to take into *in vivo* experiments, to reduce the number of animals needed in those studies.

4.2 Chapter Methods

In examining the effect of bestrophin-1 on chloride conductance, HEK293 cells are a commonly used cell line. They are well characterised electrophysiologically (*174*) and are easy to grow, maintain and transduce with AAV. HEK293 cells were transduced at an MOI of 5,000 and patched as described in chapter 2. As bestrophin-1 has been shown to be an outwardly-rectifying channel (*65*), current values generated at +20, +40, +60 and +80 mV were tested for normality with a Shapiro-Wilk test and then compared with either a one-way ANOVA or Kruskal-Wallis test with statistical significance defined as $p<0.05$. Outward chord conductance was calculated by measuring the gradient of the

trend line between 0 and +80 mV for each test group. These were tested for normality and then compared by one-way ANOVA/Kruskal-Wallis test. To confirm that any differences in conductance were due to the movement of Cl^-, sodium gluconate was used to reduce Cl^- concentration in the external solution (as performed in other studies (*73*)), and the cells were patched as described above.

4.3 Results

4.3.1 Transduction with AAV-BEST1 vectors increases conductance in HEK293 cells.

HEK293 cells showed increased chloride conductance when transduced with AAV2/2.CAG.hBEST1.pA (n=10) and AAV2/2.CAG.hBEST1.WPRE.pA (n=10) compared to un-transduced control HEK293 cells (n=10) (figure 4.1). Currents from both vectors reversed at negative potentials, consistent with an anion channel. Normality was confirmed with a Shapiro-Wilk test (table 9) and a one-way ANOVA with Tukey Multiple Comparisons was performed. Increases in current values were statistically significant at all voltage steps (+20, +40, +60 and +80 mV) between AAV2/2.CAG.hBEST1.WPRE.pA and un-transduced controls ($p<0.001$). Current values at +80 mV were statistically significant between AAV2/2.CAG.hBEST1.pA and un-transduced controls ($p<0.05$). Current values at +20, +40 and +60 mV were not significant. There was no statistically significant difference between AAV2/2.CAG.GFP.WPRE (n=11) and un-transduced controls. Equilibrium potential (reversal potential) for the buffers used in these experiments was calculated using the Nernst equation and is an estimated -33 mV. The reversal potential for cells averaged -13 mV for cells transduced with AAV2/2.CAG.hBEST1.pA and -20.3 mV for cells transduced with AAV2/2.CAG.hBEST1.WPRE.pA (compared to -8.34 mV and -14.74 mV for AAV2/2.CAG.GFP.WPRE.pA and UTC respectively).

Outward chord conductance is shown in figure 4.2. Following confirmation of normality with a Shapiro-Wilk test (table 10), differences were found to be statistically significant between un-transduced controls and both AAV2/2.CAG.hBEST1.WPRE.pA ($p<0.001$) and AAV2/2.CAG.hBEST1.pA ($p<0.05$) via one-way ANOVA with Tukey Multiple Comparisons. There was no significant difference in conductance between un-transduced controls and cells transduced with AAV2/2.CAG.GFP.WPRE. Chord conductance was ~1.6-fold greater in HEK293 cells transduced with AAV2/2.CAG.hBEST1.WPRE.pA than in cells transduced with AAV2/2.CAG.hBEST1.pA ($p<0.05$).

Given that the AAV2/2.CAG.hBEST1.WPRE.pA vector gave greater levels of protein expression and higher Cl- conductance than the AAV2/2.CAG.hBEST1.pA vector, the AAV2/2.CAG.hBEST1.WPRE.pA vector was used for further *in vitro* and *in vivo* testing.

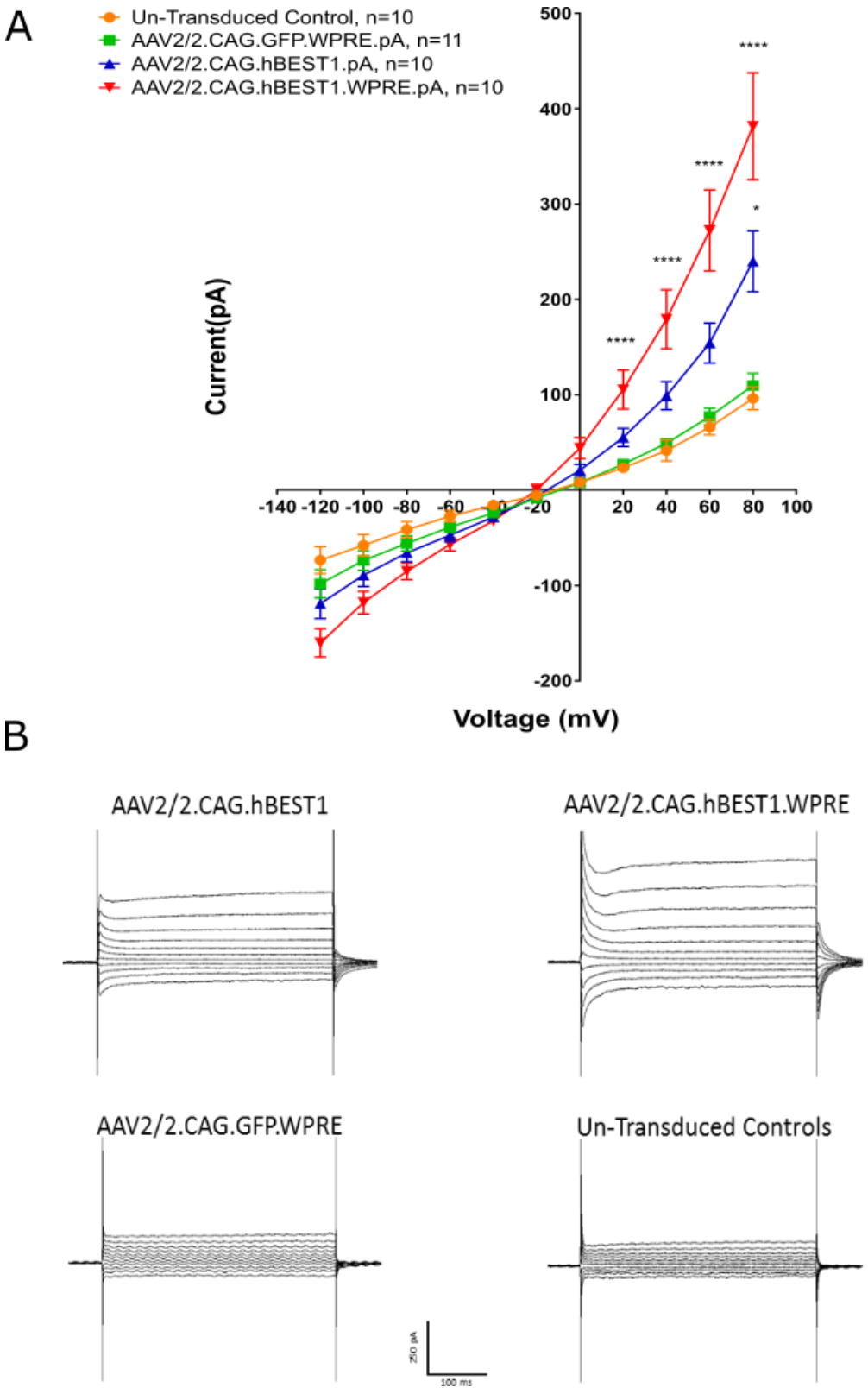

Figure 4.1. Whole-Cell Patch Clamp of HEK293 Cells. '**A**' Current (I) /Voltage (V) plots of HEK293 cells transduced with AAV-BEST1 vectors and controls. The currents produced by the AAV-BEST1 vectors both show significant differences over AAV-GFP and UTC cells at all positive voltage steps.'**B**' Current waveforms. ****=p<0.0001, *=p<0.05.

20 mV	AAV2/2.CAG.hBEST1.pA n=8	AAV2/2.CAG.hBEST1.WPRE.pA n=8	AAV2/2.CAG.GFP.WPRE.pA n=8	Un-transduced Control (UTC) n=10
Shapiro-Wilk normality test				
W	0.9073	0.9651	0.966	0.982
P value	0.3352	0.8573	0.8434	0.9749
Passed normality test (alpha=0.05)?	Yes	Yes	Yes	Yes
P value summary	ns	ns	ns	ns
40 mV				
W	0.9006	0.9594	0.9457	0.9658
P value	0.2924	0.8041	0.5901	0.849
Passed normality test (alpha=0.05)?	Yes	Yes	Yes	Yes
P value summary	ns	ns	ns	ns
60 mV				
W	0.8675	0.8535	0.9596	0.9591
P value	0.0934	0.064	0.7669	0.7752
Passed normality test (alpha=0.05)?	Yes	Yes	Yes	Yes
P value summary	ns	ns	ns	ns
80 mV				
W	0.908	0.8879	0.9653	0.9515
P value	0.2677	0.1604	0.8358	0.6857
Passed normality test (alpha=0.05)?	Yes	Yes	Yes	Yes
P value summary	ns	ns	ns	ns

Table 9. Shapiro-Wilk Test for Normality for Current Amplitudes. All values were shown to be normally distributed using the Shapiro-Wilk Test. Therefore parametric tests were used to analyse the current amplitude data.

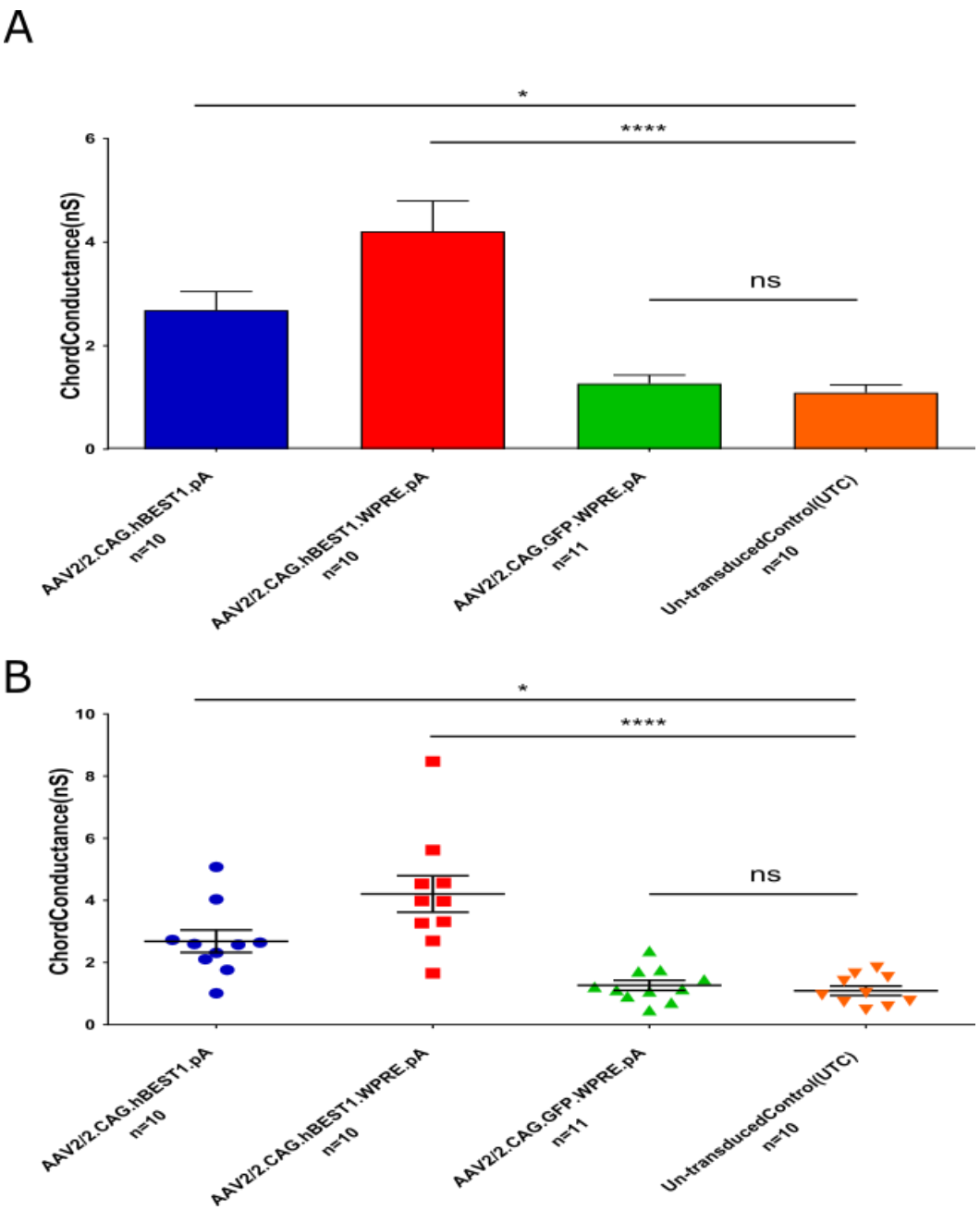

Figure 4.2. Outward Chord Conductance in HEK293 Cells Transduced with AAV-BEST1 vectors and controls. '**A**' Outward chord conductance is significantly greater in HEK293 cells transduced with AAV2/2.CAG.hBEST1.pA (n=10) or AAV2/2.CAG.hBEST1.WPRE.pA (n=10) compared to un-transduced controls (n=10). There was no significant difference between control HEK293 cells, transduced with AAV2/2.CAG.GFP.WPRE.pA (n=11), and un-transduced controls. '**B**' The dot plot of the outward chord conductance shows the spread of values for each condition. ****=$p<0.0001$, *=$p<0.05$.

Shapiro-Wilk normality test	AAV2/2.CAG.hBEST1.pA n=8	AAV2/2.CAG.hBEST1.WPRE.pA n=8	AAV2/2.CAG.GFP.WPRE.pA n=8	Un-transduced Control (UTC) n=10
Chord Conductance				
W	0.9062	0.9065	0.9633	0.9325
P value	0.2557	0.2575	0.812	0.4724
Passed normality test (alpha=0.05)?	Yes	Yes	Yes	Yes
P value summary	ns	ns	ns	ns

Table 10. Shapiro-Wilk Test for Normality for Chord Conductance. All values were shown to be normally distributed using the Shapiro-Wilk Test. Therefore parametric tests were used to analyse the current amplitude data.

4.3.2 Reduction of Cl^- leads to a reduction in current amplitude and conductance in HEK293 cells.

Replacing NaCl with sodium gluconate ($NaC_6H_{11}O_7$) in the external solution reduced Cl^- concentration from 147 mM to 7 mM. This reduction in Cl^- available for transport significantly reduced current amplitudes in HEK293 cells transduced with AAV2/2.CAG.hBEST1.WPRE.pA in the 7 mM Cl^- external solution when compared to transduced HEK293 cells in the 147 mM Cl^- external solution (figure 4.3). Shapiro-Wilk normality testing indicated that the data was not normally distributed (table 11), therefore a Kruskal Wallis with Dunn's multiple comparisons test was performed. There was no significant difference between control HEK293 cells transduced with AAV2/2.CAG.GFP.WPRE.pA patched in either external solution.

Outward chord conductance was also significantly different between HEK293 cells transduced with AAV2/2.CAG.hBEST1.WPRE.pA and controls, in the 147 mM and the 7 mM external solution. Shapiro-Wilk normality testing indicated that the data was not

normally distributed (table 12), therefore a Kruskal Wallis with Dunn's multiple comparisons test was performed. Again, no significant difference was seen between control HEK293 cells transduced with AAV2/2.CAG.GFP.WPRE.pA (figure 4.4).Despite the increases in current amplitude and chord conductance, the reversal potential in these cells was more positive than in previous samples. Values were 6.19 mV and 12.08 mV for cells transduced with AAV2/2.CAG.hBEST1.WPRE.pA in 'high' Cl- and 'low' Cl- respectively. Control transductions with AAV2/2.CAG.GFP.WPRE.pA gave reversal potentials at 39.4 mV and 15.9 mV for 'high' Cl- and 'low' Cl- conditions respectively. This is far more positive than estimated by the Nernst equation.

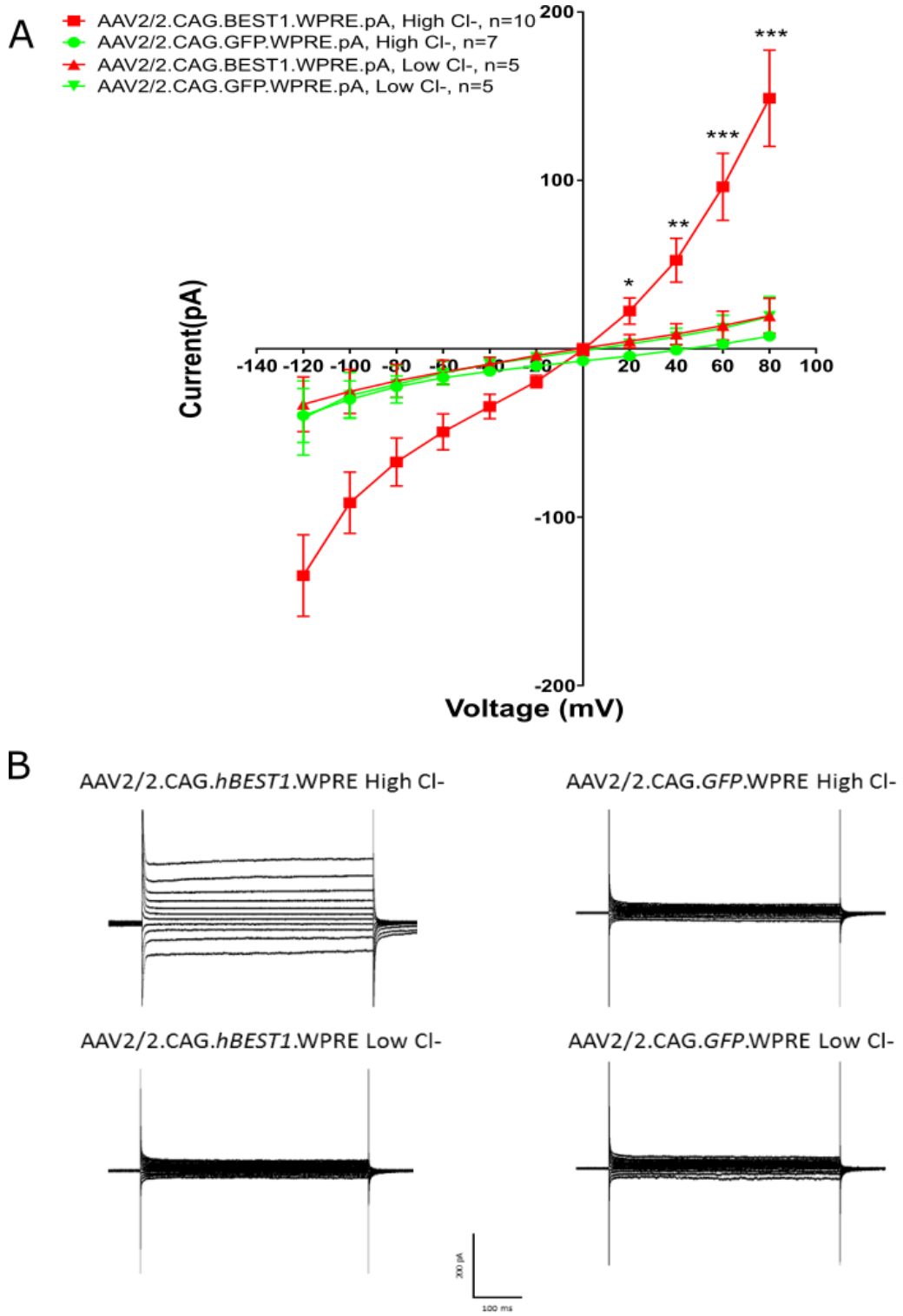

Figure 4.3. Whole-Cell Patch Clamping of HEK293 Cells in Reduced Cl- External Solution. '**A**' Current (I) /Voltage (V) plots show that current amplitude is significantly reduced at all positive voltage steps in HEK293 cells transduced with AAV2/2.CAG.hBEST1.WPRE.pA in the low Cl^- (7mM) external solution and HEK293 cells in the high Cl^- (147mM) external solution. '**B**' Current waveforms. ***=p<0.001, **=p<0.01, *=p<0.05.

Shapiro-Wilk normality test	AAV2/2.CAG.BEST1.WPRE.pA, High Cl-	AAV2/2.CAG.GFP.WPRE.pA, High Cl-	AAV2/2.CAG.BEST1.WPRE.pA, Low Cl-	AAV2/2.CAG.GFP.WPRE.pA, Low Cl-
20 mV				
W	0.876	0.9014	0.6439	0.6533
P value	0.2094	0.227	0.0023	0.0029
Passed normality test (alpha=0.05)?	Yes	Yes	No	No
P value summary	ns	ns	**	**
40 mV				
W	0.9305	0.9634	0.6476	0.6094
P value	0.4524	0.847	0.0025	0.0008
Passed normality test (alpha=0.05)?	Yes	Yes	No	No
P value summary	ns	ns	**	***
60 mV				
W	0.9201	0.9596	0.6489	0.632
P value	0.358	0.8156	0.0026	0.0016
Passed normality test (alpha=0.05)?	Yes	Yes	No	No
P value summary	ns	ns	**	**
80 mV				
W	0.959	0.9247	0.7133	0.6473
P value	0.8103	0.3981	0.0131	0.0025
Passed normality test (alpha=0.05)?	Yes	Yes	No	No
P value summary	ns	ns	*	**

Table 11. Shapiro-Wilk Test for Normality for Current Amplitude in Cl- Reduction Experiments. Shapiro-Wilk tests were performed for the current amplitudes at 20, 40, 60 and 80 mV. Data from the low chloride conditions were shown to not be normally distributed using the Shapiro-Wilk Test. Therefore non-parametric tests were used to analyse the current amplitudes.

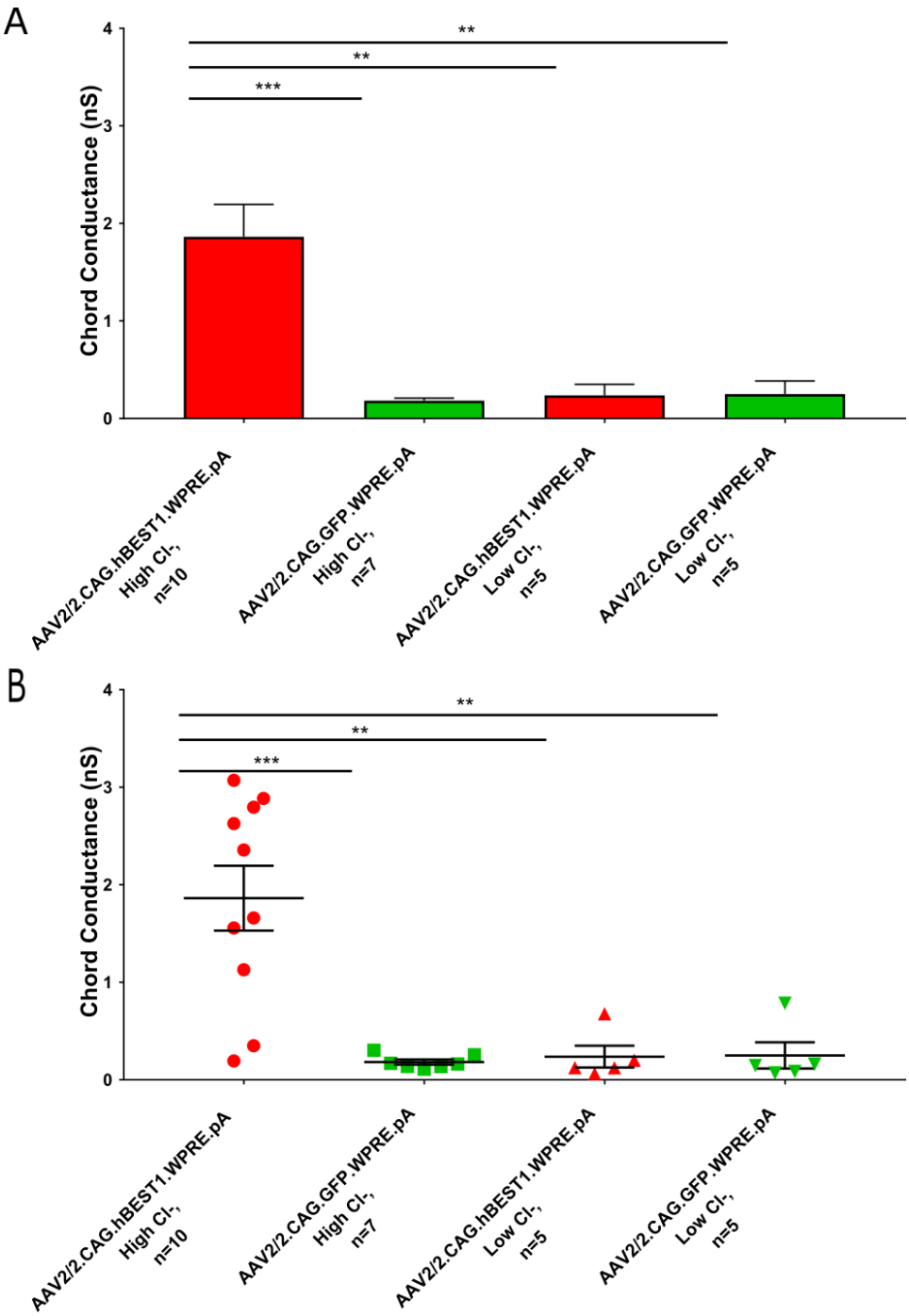

Figure 4.4. Outward Chord Conductance in HEK293 Cells in Reduced Cl- External Solution. '**A**' Outward chord conductance is significantly higher in HEK293 cells transduced with AAV2/2.CAG.hBEST1.WPRE.pA and patched in the high Cl^- buffer than those patched in the low Cl^- (7mM) buffer. No significant difference is seen between AAV2/2.CAG.GFP.WPRE.pA transduced controls. '**B**' A dot plot of outward chord conductance shows the relatively large spread of the data in HEK293 cells transduced with AAV2/2.CAG.hBEST1.WPRE.pA and patched in the high Cl^- (147mM) buffer and all other conditions. *=$p<0.05$.

Shapiro-Wilk normality test	AAV2/2.CAG.BEST1.WPRE.pA, High Cl-	AAV2/2.CAG.GFP.WPRE.pA, High Cl-	AAV2/2.CAG.BEST1.WPRE.pA, Low Cl-	AAV2/2.CAG.GFP.WPRE.pA, Low Cl-
W	0.9052	0.8722	0.7273	0.6668
P value	0.2494	0.194	0.0181	0.0042
Passed normality test (alpha=0.05)?	Yes	Yes	No	No
P value summary	ns	ns	*	**

Table 12. Shapiro-Wilk Test for Normality for Chord Conductance in Cl- Reduction Experiments. Some values were shown to not be normally distributed using the Shapiro-Wilk Test. Therefore non-parametric tests were used to analyse the current amplitude data.

4.3.3 Percentage Transduction Efficiency in Whole-Cell Patch-Clamping Experiments.

The percentage efficiency of the transductions could be estimated from the patch-clamp data, if we take the highest conductance value in the un-transduced controls and make the assumption that any value below that constitutes a cell that is not expressing bestrophin-1, then we can calculate a transduction efficiency in which levels of BEST1 cross the detection threshold of ~80% in HEK293 cells transduced with AAV2/2.CAG.hBEST1.pA and ~90% in HEK293 cells transduced with AAV2/2.CAG.hBEST1.WPRE.pA. This is summarised in figure 4.5. A Chi-squared test was applied and returned a p-value of 0.0004.

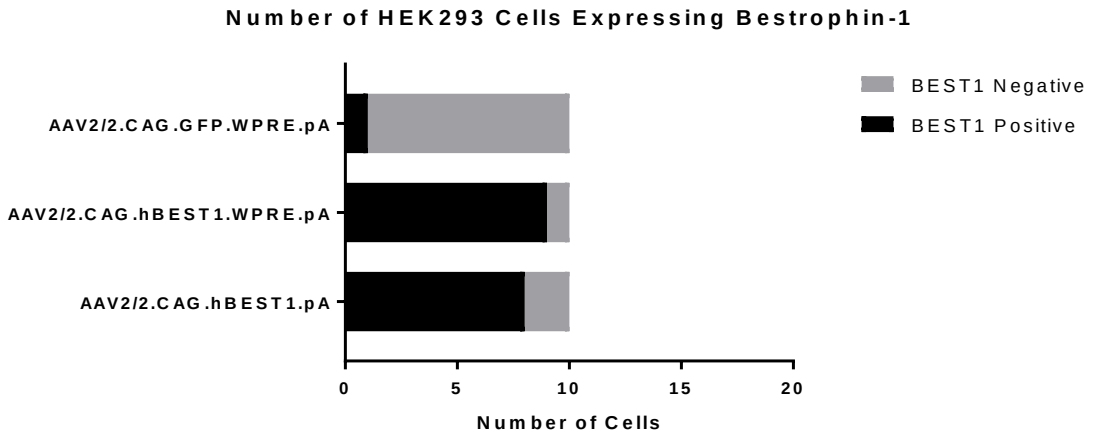

Figure 4.5. Number of Cells Positive for Bestrophin-1 Expression. Cells in each transduced sample group that showed conductance above the level of the highest cell from the UTC group were characterised as being 'BEST1 Positive'. The percentage number of cells positive for Bestrophin-1 was 9.1%, 90% and 80% for AAV2/2.CAG.GFP.WPRE, AAV2/2.CAG,hBEST1.pA and AAV2/2.CAG.hBEST1.WPRE.pA respectively. Chi-squared, $p<0.001$.

4.4 Chapter Discussion

Bestrophin-1 is an outwardly rectifying chloride ion (Cl^-) channel. Chloride conductance in HEK293 cells was significantly increased when transduced with either AAV2/2.CAG.hBEST1.pA or AAV2/2.CAG.hBEST1.WPRE.pA compared to UTC. No increases were seen in control cells transduced with AAV2/2.CAG.GFP.WPRE compared to UTC. This shows that both AAV-BEST1 vectors deliver functional bestrophin-1 protein to cells following transduction. The inclusion of the WPRE element in the vector, not only gives a significant increase in bestrophin-1 expression as measured by western blot and ICC (see chapter 3), but also gives a significant increase in chloride conductance. The results are consistent with plasmid transfections in HEK293 cells; however the amplitudes are lower than what would be expected from plasmid transfections. Reversal potential for cells transduced with AAV2/2.CAG.hBEST1.WPRE.pA were consistent with previous studies of bestrophin-1; however cells transduced with AAV2/2.CAG.hBEST1.pA showed slightly more positive reversal potentials. This could be due to fewer cells expressing detectable bestrophin-1 in these samples, which could increase the average reversal potential as cells not expressing bestrophin-1 would have a more positive reversal potential.

Reducing chloride in the external recording solution from 147 mM to 7 mM, led to a significant reduction in both current amplitude and conductance, confirming that changes in conductance were due to movement of chloride ions as opposed to other ions such as Ca^{2+}. Despite this, the reversal potential for HEK293 cells patched in the second experiment is far more positive than expected (figure 4.3) and also more positive than

they were in the original experiment (figure 4.1). The Cl- reduction experiments were done in a different laboratory than the original experiment and, although the reagents used were identical, differences in the ionic composition of the water used to dilute the reagents and electrostatic variations between the locations could have affected this. Given that the current amplitudes and conductance's show significant differences indicated that the introduction of bestrophin-1 into these cells is facilitating Cl- movement across the membrane. Another way of confirming that the changes in conductance are due to the movement of Cl^- would be to include an inhibitor of Cl^- channels, such as 4,4′ Diisothiocyanatostilbene-2,2'-disulfonic acid (DIDS) or niflumic acid (*73, 175*), in the external buffer.

In the experiments detailed in 4.3.1 and 4.3.2, the variation in the current amplitudes and conductance was much greater in recordings taken from HEK293 cells transduced with either AAV2/2.CAG.hBEST1.pA or AAV2/2.CAG.hBEST1.WPRE.pA than control cells either transduced with AAV2/2.CAG.GFP.WPRE.pA or that were left un-transduced. This is likely to be due to the 'blind-patching' approach taken, meaning that some of the cells that were patched, in the AAV-BEST1 treated samples, may not have successfully taken up the virus, and some will have taken up varying amounts of the virus. This approach is also likely to be the reason that the reversal potentials in transduced HEK293 cells are variable. Analysis of bestrophin-1 expression in figure 4.5 suggests that >90% of cells did successfully take up the vector. However, this is an estimate of the amount of bestrophin-1 relative to an un-transduced control and would be better backed-up with more quantitative measurements from an ELISA. These experiments show that transducing HEK293 cells with either

AAV2/2.CAG.hBEST1.pA or AAV2/2.CAG.hBEST1.WPRE.pA successfully expresses active bestrophin-1 at the plasma membrane, despite a large amount of expression in the cytosol (figure 3.15). The inclusion of the WPRE significantly increases Cl^- conductance over all conditions tested.

Chapter 5. Proteomics

5.1 Chapter Introduction

Due to the packaging capacity of AAV (~4.7 kb), when creating vectors expressing bestrophin-1, it is necessary to use the BEST1 cDNA (~1.7 kb) as opposed to the entire genomic sequence. During normal circumstances, genomic DNA is transcribed and undergoes various post-transcriptional processes before the mature mRNA is translated. In sending the BEST1 cDNA back through the nucleus, it is possible that the sequence would not be transcribed and translated into the wild-type bestrophin-1 protein. To confirm that the cDNA is translated correctly, immuno-precipitation was used to purify bestrophin-1 from cell lysates. LC-MS/MS was then used to sequence the protein to confirm correct processing.

5.2 Chapter Methods

High levels of the bestrophin-1 protein will be needed for analysis. Therefore, plasmid transfection was performed in HEK293 cells, with the plasmid used to create the AAV vector (pAAV.CAG.hBEST1.WPRE). Transfections and cell culture procedures are described in chapter 2. Following transfection, samples were lysed, put through an immuno-precipitation reaction and ran on an SDS-PAGE gel, as described in chapter 2. An SDS-Gel was taken for western blotting (with an antibody specific to bestrophin-1) and another was taken for coomassie staining to look at total protein. Bands corresponding to bestrophin-1 were cut out of the gel with a scalpel and sent to the Advanced Proteomics Facility at the University of Oxford for LC-MS/MS analysis. This process is summarised in figure 5.1.

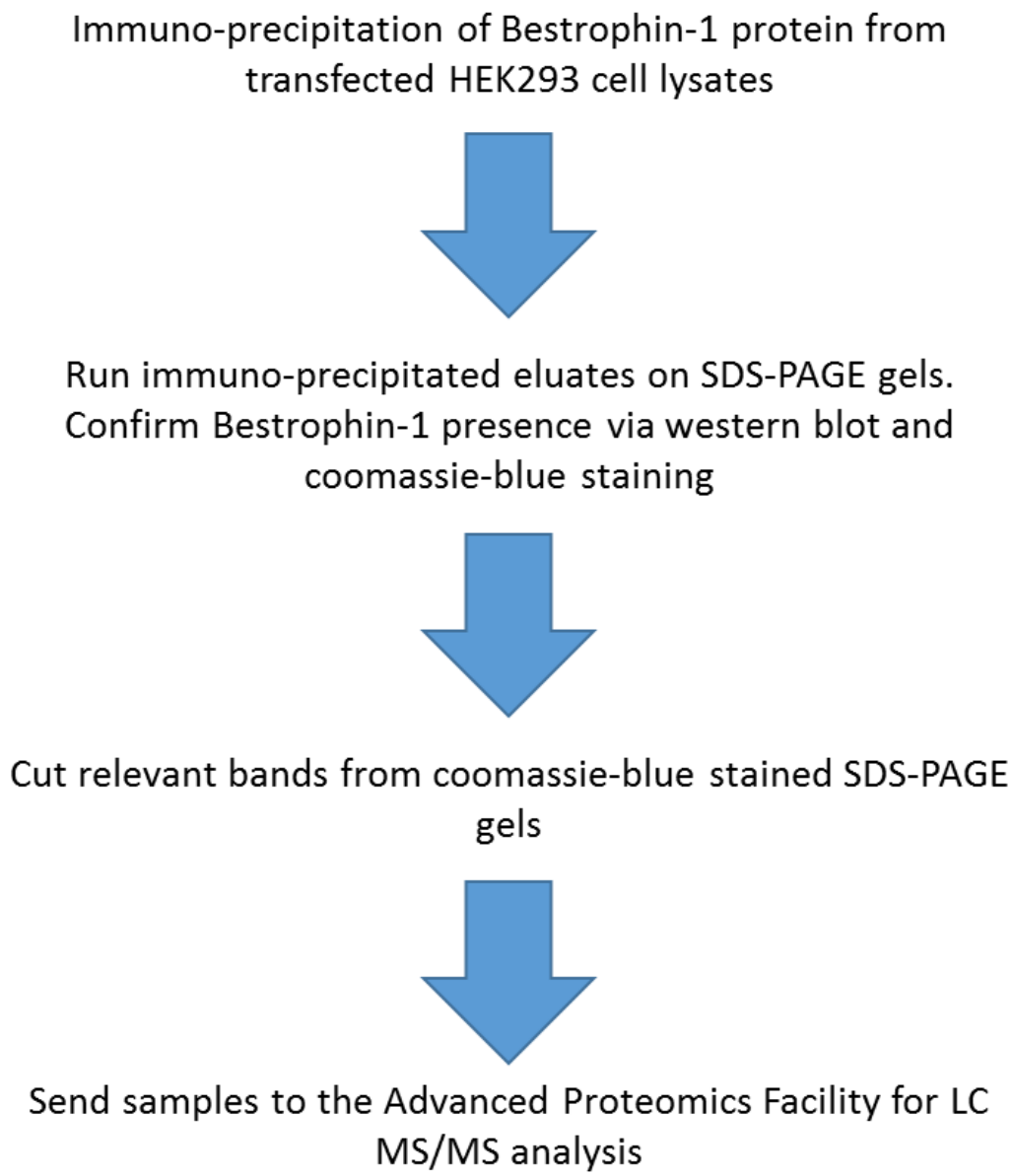

Figure 5.1. Flow Chart of Proteomic Experiment Set-up

5.3.1 Immuno-precipitation of Bestrophin-1 from HEK293 Lysates

Bestrophin-1 was detected in eluted samples following the immuno-precipitation procedure described in chapter 2. Figure 5.2 shows a band corresponding to 67 kDa (Bestophin-1) detected via western blot in eluates from HEK293 cells transfected with pCAG.*hBEST1*.WPRE. Some bestrophin-1 was left in the 'pre-wash' sample, indicating that the binding of the mouse anti-bestrophin-1 primary antibody could be optimised if required. No bestrophin-1 bands can be seen the pCAG.GFP.WPRE.pA transfected HEK293 cell lysates following immuno-precipitation with the mouse anti-hBestrophin-1 antibody.

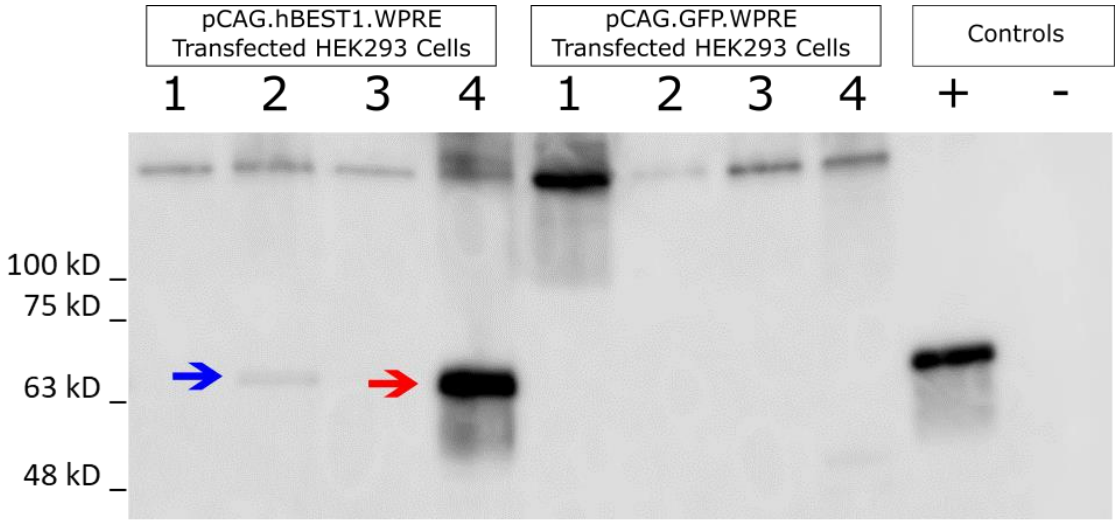

Figure 5.2. Western Blot of Bestrophin-1 Immuno-precipitated from Transfected HEK293 Cells. Lane 1 is the antibody sample, lane 2 is the Pre-wash sample, lane 3 is the wash sample and lane 4 is the eluate. A band, corresponding to Bestrophin-1, can be clearly seen in the eluate from the pCAG.*hBEST1*.WPRE transfected HEK293 cells (indicated by the red arrow). The same band is seen in the pre-washed samples (blue arrow) and indicates that some of the bestrophin-1 is not being bound by the antibody. The bestrophin-1 band is not present in the eluate from the pCAG.*GFP*.WPRE transfected HEK293 cells. Cell lysates from pCAG.*hBEST1*.WPRE (+) and pCAG.*GFP*.WPRE (-) transfected HEK293 cells were used as controls.

Figure 5.3 shows the corresponding coomassie-stained SDS-PAGE gel. The gel shows multiple bands in the pre-wash samples that are not present in the eluate (in both pCAG.hBEST1.WPRE and pCAG.GFP.WPRE-transfected HEK293 cells) which hinder the identification of the bestrophin-1 band present in the pre-wash lane in figure 5.2. There are still several bands in the eluate. These could represent the protein G that was used to immuno-precipitate the Bestrophin-1. At roughly 67kD, a band can be seen in the eluate from pCAG.hBEST1.WPRE-transfected HEK293 cells that cannot be seen in the eluate from the pCAG.GFP.WPRE-transfected control HEK293 cells. This region of the gel was excised with a scalpel and transferred to a 1.5 mL Eppendorf tube for transfer to the Advanced Proteomics Facility.

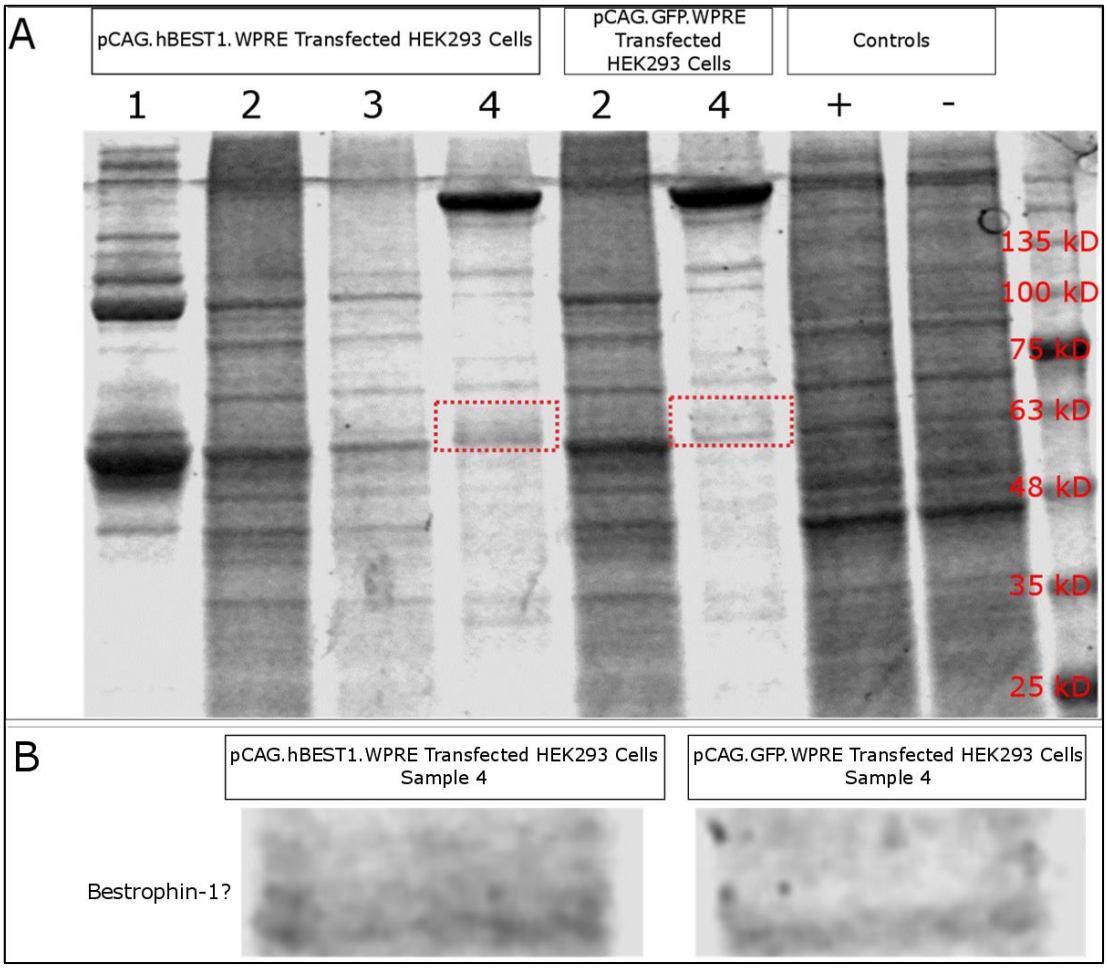

Figure 5.3. Coomassie Stained SDS-PAGE Gel of Bestrophin-1 Immuno-precipitated from Transfected HEK293 Cells. Lane 1 is the antibody sample, lane 2 is the Pre-wash sample, lane 3 is the wash sample and lane 4 is the eluate. A band corresponding to bestrophin-1 is highlighted in immune-precipitated bestrophin-1 lysates ('**A**') that is not seen in control samples (highlighted by the red boxes). '**B**' shows these highlighted areas in more detail, there appears to be a band corresponding to bestrophin-1. Lane 4 also shows a prominent band towards the top of the gel. This is likely to be the IgG from the mouse anti-bestrophin-1 primary antibody as it is not present in any of the other lanes.

5.3.2 LC-MS/MS Analysis of Bestrophin-1

MTITYTSQVANARLGSFSRLLLCWRGSIYKLLYGEFLIFLL
CYYIIRFIYRLALTEEQQLMFEKLTLYCDSYIQLIPISFVL
GFYVTLVVTRWWNQYENLPWPDRLMSLVSGFVEGKDEQGRL
LRRTLIRYANLGNVLILRSVSTAVYKRFPSAQHLVQAGFMT
PAEHKQLEKLSLPHNMFWVPWVWFANLSMKAWLGGRIRDPI
LLQSLLNEMNTLRTQCGHLYAYDWISIPLVYTQVVTVAVYS
FFLTCLVGRQFLNPAKAYPGHELDLVVPVFTFLQFFFYVGW
LKVAEQLINPFGEDDDDFETNWIVDRNLQVSLLAVDEMHQD
LPRMEPDMYWNKPEPQPPYTAASAQFRRASFMGSTFNISLN
KEEMEFQPNQEDEEDAHAGIIGRFLGLQSHDHHPPRANSRT
KLLWPKRESLLHEGLPKNHKAAKQNVRGQEDNKAWKLKAVD
AFKSAPLYQRPGYYSAPQTPLSPTPMFFPLEPSAPSKLHSV
TGIDTKDKSLKTVSSGAKKSFELLSESDGALMEHPEVSQVR
RKTVEFNLTDMPEIPENHLKEPLEQSPTNIHTTLKDHMDPY
WALENRDEAHS

Red = Detected Peptides
Black = Not detected

Figure 5.4. Sequence Coverage of hBestrophin-1 Following LC-MS/MS. Analysis detected 59% of the Bestrophin-1 peptides. Amino acids at both N and C-terminals have been detected. All regions that were successfully sequenced show the expected sequence with no mutations.

LC-MS/MS identified Bestrophin-1 as the top hit in gel slices cut out of the SDS-Gel shown in figure 5.2. 59% of the bestrophin-1 peptides were identified predominantly covering the C-terminus of Bestrophin-1 (figure 5.4).

5.4 Chapter Discussion

LC-MS/MS analysis, although not covering the whole bestrophin-1 protein, gave enough information to conclude that the protein is being translated correctly, particularly as the NH- and C-termini were exactly as predicted. Mass spectrometry is a useful tool to confirm that the final sequence of any recombinant protein, being expressed from a gene therapy vector, is correct. It may be that mass spectrometry will need to be included in any future gene therapy program before going into clinical trial. There is however some limitation, based on the availability of amino acids at digestion sites. For instance, trypsin enzymes cleave proteins at lysine or arginine amino acids, except when either is followed by proline (*176*). It is possible to use other enzymes to cleave the protein, such as chymotrypsin (a serine protease that cleaves at the C-terminal side of tyrosine, phenylalanine and tryptophan residues), LysC (cleaves on the C-terminal side of lysine residues), LysN (cleaves of the N-terminal side of lysine residues), AspN (cleaves on the N-terminal side of aspartate and cysteine residues), GluC (cleaves at the C-terminal side of aspartate and glutamate residues) and ArgC (cleaves at the C-terminal side of arginine residues, even when immediately followed by a proline residue) (*177*). The use of a single enzyme to cleave target proteins prior to analysis can result in issues with sequence coverage due to the production of large fragments and can also lead to difficulties in the detection of phosphorylated residues (*178*). As bestrophin-1 is known to be phosphorylated by protein phosphatase 2A (PP2A), this is an important consideration for future analysis (*90*). The use of a combination of proteases would allow a range of smaller peptides to be produced and could result in better coverage of the protein sequence when analysed using LC-MS/MS

(*179*). Also, bestrophin-1 has five transmembrane regions within the first 291 amino acids. These hydrophobic regions are difficult to digest as they contain few protease cleavage sites, making confirmation of the whole sequence difficult.

Immuno-precipitation, using the mouse anti-Bestrophin-1 E6-6 antibody, allowed the extraction of bestrophin-1 from the transfected HEK293 cell lysate. However, bestrophin-1 was not the only protein band seen on the Coomassie-stained SDS-PAGE gel. The use of other assays may be more successful in isolating bestrophin-1, examples of which could include pull-down assays using 'bait' proteins in the place of antibodies, or high-performance liquid chromatography (HPLC).

Bestrophin-1 was the most abundant protein identified following the digestion and processing of the extracted gel piece. Peptides detected by the LC-MS/MS sequencing covered just 59% of the bestrophin-1 protein, however the detection of the final 51 amino acids indicates that the protein has been translated correctly, with no frameshifts introduced. The coverage from the LC-MS/MS combined with the protein running at the correct size on the SDS-PAGE gel (as confirmed by western blot in chapters 3 and 5) indicates that the protein has not been alternatively spliced and is the correct sequence. Before any vector is taken into the clinic, more mass-spectrometry should be performed to cover the entire bestrophin-1 sequence.

Chapter 6. *In Vivo* Testing of AAV2/2.CAG.*hBEST1*.WPRE.pA

6.1 Chapter Introduction

As the AAV2/2.CAG.hBEST1.WPRE.pA vector gave greater levels of bestrophin-1 expression *in vitro* and was shown to increase chloride conductance over the AAV2/2.CAG.hBEST1.pA vector, it was chosen for *in vivo* assessment. Choosing a suitable model for examining bestrophin-1 transfer i*n vivo* was difficult. Studies have suggested that murine bestrophin-1 is not as highly expressed in RPE as it is in primate RPE (*73, 78*) and, as such, *Best1*$^{-/-}$ mice do not show observable retinal pathology. As a result, we used wild-type C57BL/6J mice to examine transgene expression in the retina following sub-retinal injection.

6.2 Chapter Methods

C57BL/6J mice were purchased from Charles River and were housed as described in chapter 2. Sub-retinal injections were performed (also described in chapter 2) and the mice were sacrificed at 4 weeks post-injection.

For the pilot study, 12 mice were injected. 6 eyes were taken for western blotting and 6 were taken for immunohistochemistry. Of the samples taken for western blot, 3 were lysed as whole eyes and 3 were separated into retina and eye-cup samples. As the majority of the RPE stays on the eye-cup, this was a way of analysing the expression of the recombinant protein in the target cell (RPE) and the retina. Despite the lack of native bestrophin-1 in the mouse retina, western blots and IHC were performed with an anti-human bestrophin-1 antibody which did not detect mouse bestrophin-1 (see figure

6.2). This ensured that any detection of bestrophin-1 would be from the vector as opposed to native.

Following on from the pilot, 24 mice were used for a more in-depth high dose vs low dose comparison to analyse any potential damage to the retina due to expression in retinal cells (such as the photoreceptors). The mice were injected either bilaterally (injected with either a dose of vector or sham in both eyes), unilaterally (one eye injected and one left uninjected) or were left uninjected. Of the total 48 eyes, there were 15 injected with a high dose of vector, 15 injected with low dose of vector, 5 injected with sham (PBS+0.001%PF-68) and 13 eyes were left uninjected. Animals were analysed at 4 weeks post-injection using optical coherence tomography to measure retinal and outer nuclear layer thickness. Scans were centred on the optic nerve (see chapter 2.21) and analysed as shown in figure 6.1. Retinal and ONL thickness was analysed with a Shapiro-Wilk test for normality and, once normality was confrimed, a one-way ANOVA with Tukey multiple comparisons was performed. Where normality was not confirmed, a Kruskal-Wallis with Dunn’s multiple comparisons test was utilised. Eyes were harvested, frozen and cryo-sectioned for IHC.

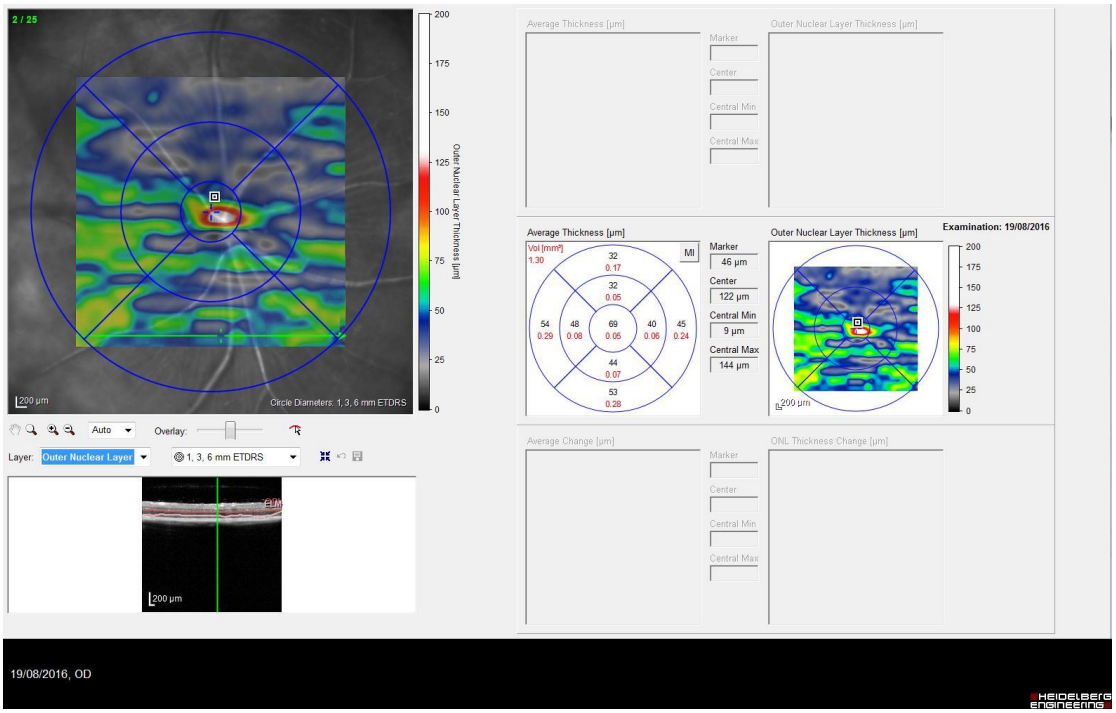

Figure 6.1. Analysis of OCT Images. An ETDRS grid was laid out over the retina and the average thickness for each of the 9 sections was calculated by the Heidelberg software. These numbers were averaged to give the average thickness of the retina or ONL.

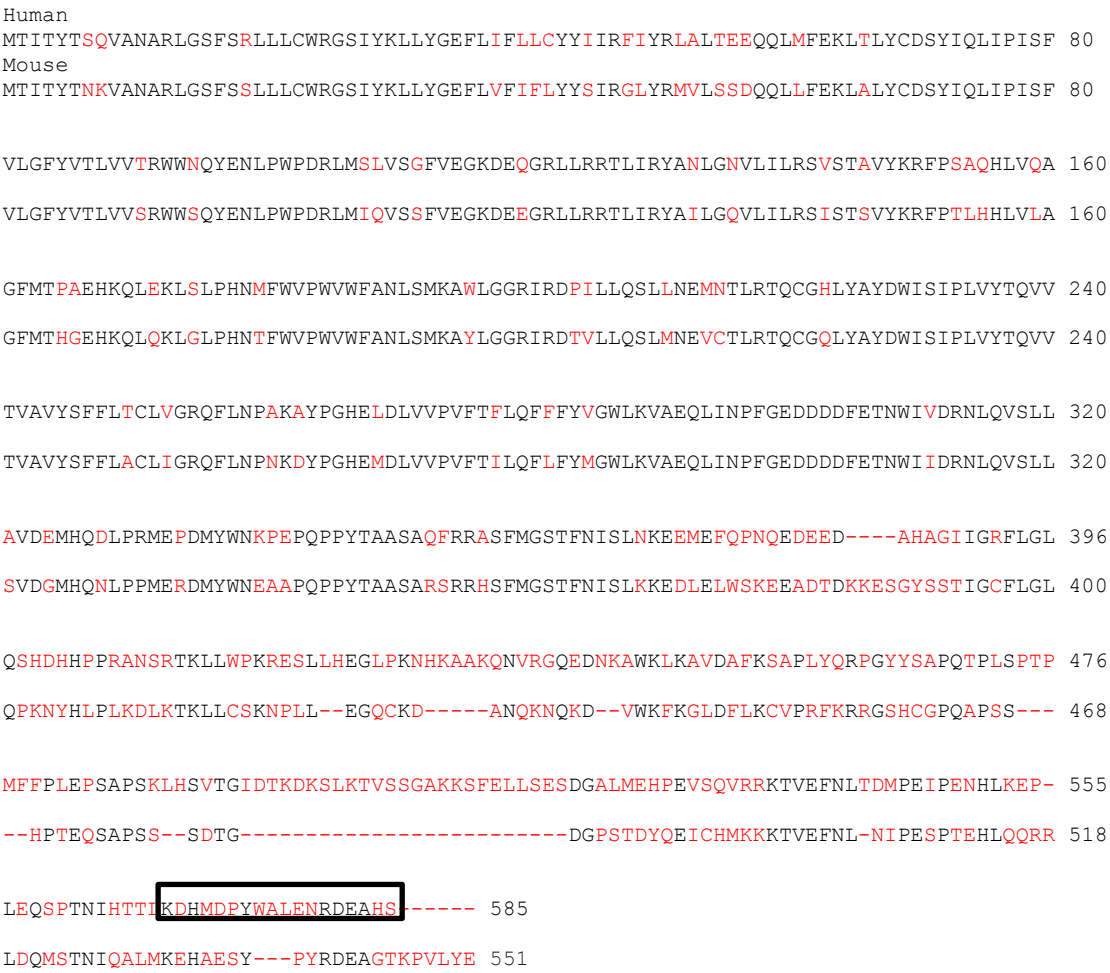

Figure 6.2. Alignment of Human and Mouse Bestrophin-1. Alignments between human and mouse bestrophin-1 show 64% homology between the two species. The binding region of the mouse anti-human bestrophin-1 antibody is highlighted in the last 18 amino acids of human bestrophin-1.

6.3 Results

6.3.1 Pilot Study in Wild Type C57BL/6J Mice

The western blot shown in figure 6.3 shows successful transfer of human bestrophin-1 into the eyes of wild-type C57BL/6J mice. Bestrophin-1 is detected in whole eye samples as well as in both isolated eye-cup and retinal samples. Confocal imaging of cyro-sectioned eyes shows detectable expression of human bestrophin-1 in the RPE of injected wild-type C57BL/6J mice when compared to controls (figure 6.4). The localisation of the bestrophin-1 protein appears to be predominantly at the basolateral membrane as expected. There is, however, some present in the cytosol, possibly due to the overexpression of the protein from the strong promoter and the inclusion of the WPRE. Figure 6.4 also shows some bestrophn-1 staining in the retina, particularly in the outer segments.

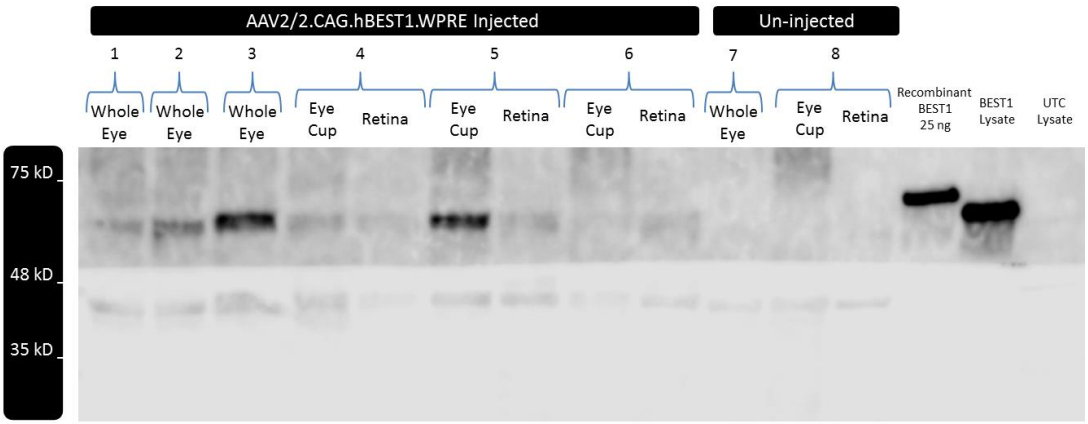

Figure 6.3. Expression of hBestrophin-1 in C57BL/6 WT Mice following Sub-Retinal Injection of AAV2/2.CAG.hBEST1.WPRE. Expression of bestrophin-1 can be detected in all injected samples and is absent in the analysed un-injected samples. Expression of bestrophin-1 appears to be greater in the eye-cup samples when compared to the retinal samples however the number of samples (n=3 per group) is too low to quantify. HEK293 cells transfected with pCAG.hBEST1.WPRE and recombinant, myc-tagged, human bestrophin-1 (Origene, TP314156) were used as positive controls (recombinant bestrophin-1 runs higher due to the extra size of the myc-tag). Antibodies were Mouse anti-Bestrophin-1 (Abcam, ab2182), Rabbit anti-β-actin (Abcam, ab8227), Donkey anti-Mouse HRP (Abcam, ab98799) and Donkey anti-Rabbit HRP (Abcam, ab98503).

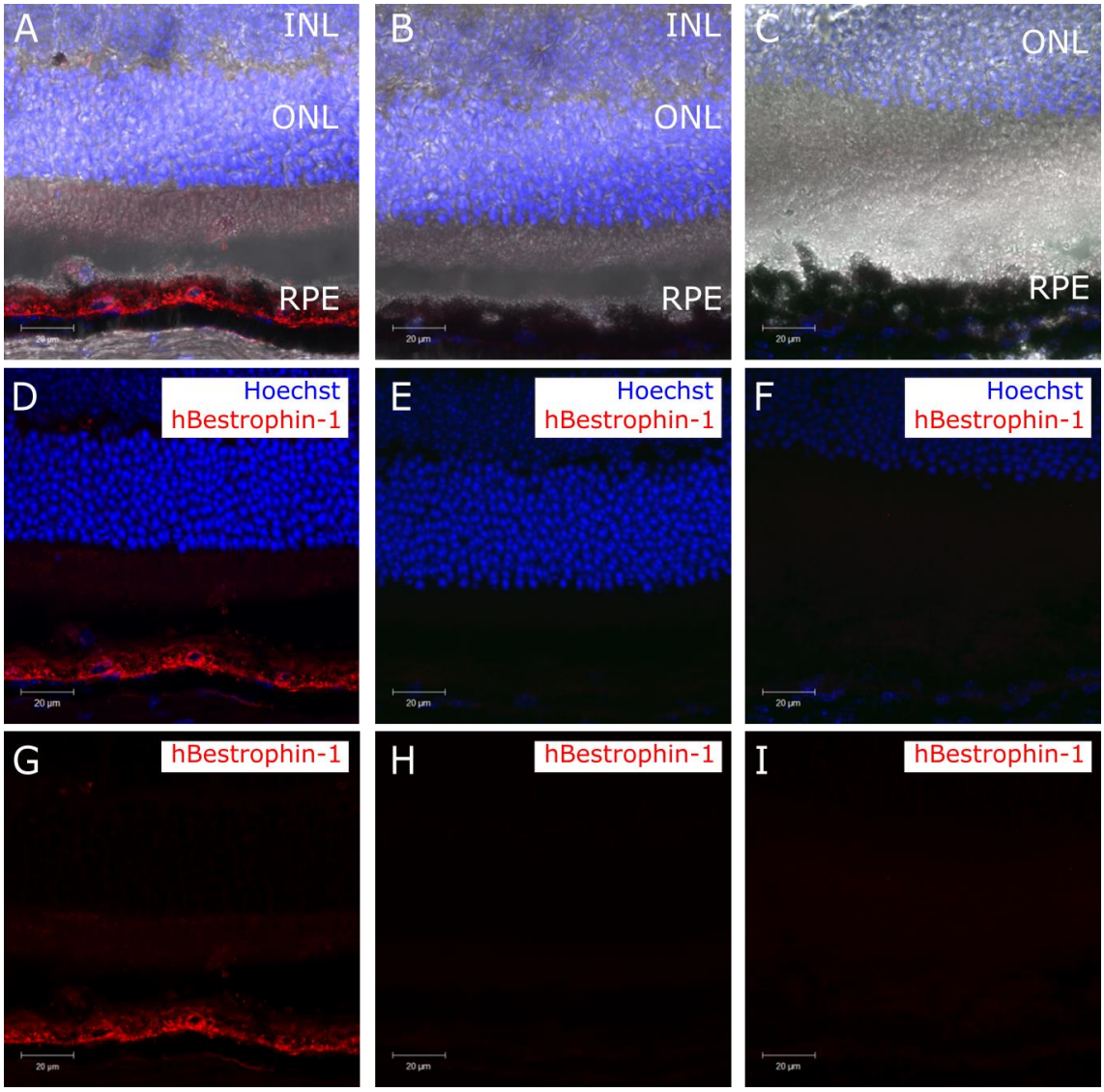

Figure 6.4. Cyrosections of AAV2/2.CAG.hBEST1.WPRE injected C57BL/6 Eyes Immuno-stained for hBestrophin-1. Immunohistochemical analysis shows human bestrophin-1 expression in the RPE of injected mice (A, D and G) which is absent in the RPE of un-injected controls (C, F and I). Secondary-only controls confirmed that expression was not due to auto-fluoresence (B, E and H). There is no detectable expression in the neural retina. Antibodies were: Mouse anti-bestrophin-1 (Abcam, ab2182) and Donkey anti-Mouse Alexa Fluor 647 (Life Technologies, A21236). Scale bars = 20 µM.

6.3.2 Dose Comparison Study in Wild Type C57BL/6J Mice

Figure 6.4 shows examples of images, taken by OCT, of the retinas of mice injected with high, low and sham injections. Figure 6.5 also shows an un-injected eye for comparison. Retinal thickness for each condition was measured and was shown to not be normally distributed by the Shapiro-Wilk test for normality (table 13). As such, the data was subjected to a Kruskal-Wallis, with Dunn's multiple comparisons, test which showed significant thinning of the retina in eyes injected with a high dose of AAV2/2.CAG.hBEST1.WPRE.pA (n=15) compared to sham (n=5, $p<0.05$) and un-injected controls (n=13, $p<0.0001$) (figure 6.6). Eyes that were injected with the low dose of AAV2/2.CAG.hBEST1.WPRE.pA (n=15) showed no significant change when compared to sham-injected controls but did show a significant difference when compared to un-injected eyes ($p<0.01$). There was no significant change detected between high dose and low dose eyes ($p=0.0737$), between low dose and sham injected eyes ($p>0.9999$) and between sham injected and un-injected eyes ($p>0.9999$).

As the retinal expression seen in the pilot study was present in the photoreceptors, ONL thickness was analysed to see if the significant retinal thinning was due to loss of the photoreceptor layer. Like with the retinal thickness, ONL thickness was analysed with a Shapiro-Wilk test for normality (table 13), and was shown to be normally distributed. A one-way ANOVA, with Tukey's Multiple Comparisons, was utilised and indicated significant thinning of the ONL in eyes injected with the high dose compared to low dose ($p<0.001$), sham ($p<0.05$) and un-injected ($p<0.0001$). There was no significant

difference between low dose and sham injected eyes, low dose and un-injected eyes or between sham injected and un-injected eyes.

IHC of cyro-sectioned eyes from high-dose recipients show detectable bestrophin-1 expression in the RPE however no detectable murine rhodopsin expression, indicating loss of the photoreceptors (figure 6.8). The detected bestrophin-1 protein was localised to the basolateral membrane in eyes that received a low dose of vector but was seen throughout the cytosol in eyes that received the high dose (figure 6.9). Rhodopsin was detected in low dose recipient eyes as was human Bestrophin-1.

Shapiro-Wilk normality test	High Dose (n=15)	Low Dose (n=15)	Sham (n=5)	Uninjected (n=13)
Retinal Thickness				
W	0.8034	0.8045	0.9638	0.9648
P value	0.0041	0.0042	0.8344	0.8254
Passed normality test (alpha=0.05)?	No	No	Yes	Yes
P value summary	**	**	Ns	ns
ONL Thickness				
W	0.9368	0.891	0.9865	0.94
P value	0.3443	0.0695	0.966	0.4569
Passed normality test (alpha=0.05)?	Yes	Yes	Yes	Yes
P value summary	ns	Ns	ns	ns

Table 13. Shapiro-Wilk Test for Normality for Retinal and ONL Thickness. All ONL thickness measurements were shown to be normally distributed using the Shapiro-Wilk Test, and were therefore analysed using parametric tests. When plotting retinal thickness, some conditions were shown to not be normally distributed and hence the retinal thickness measurements were analysed using a non-parametric test.

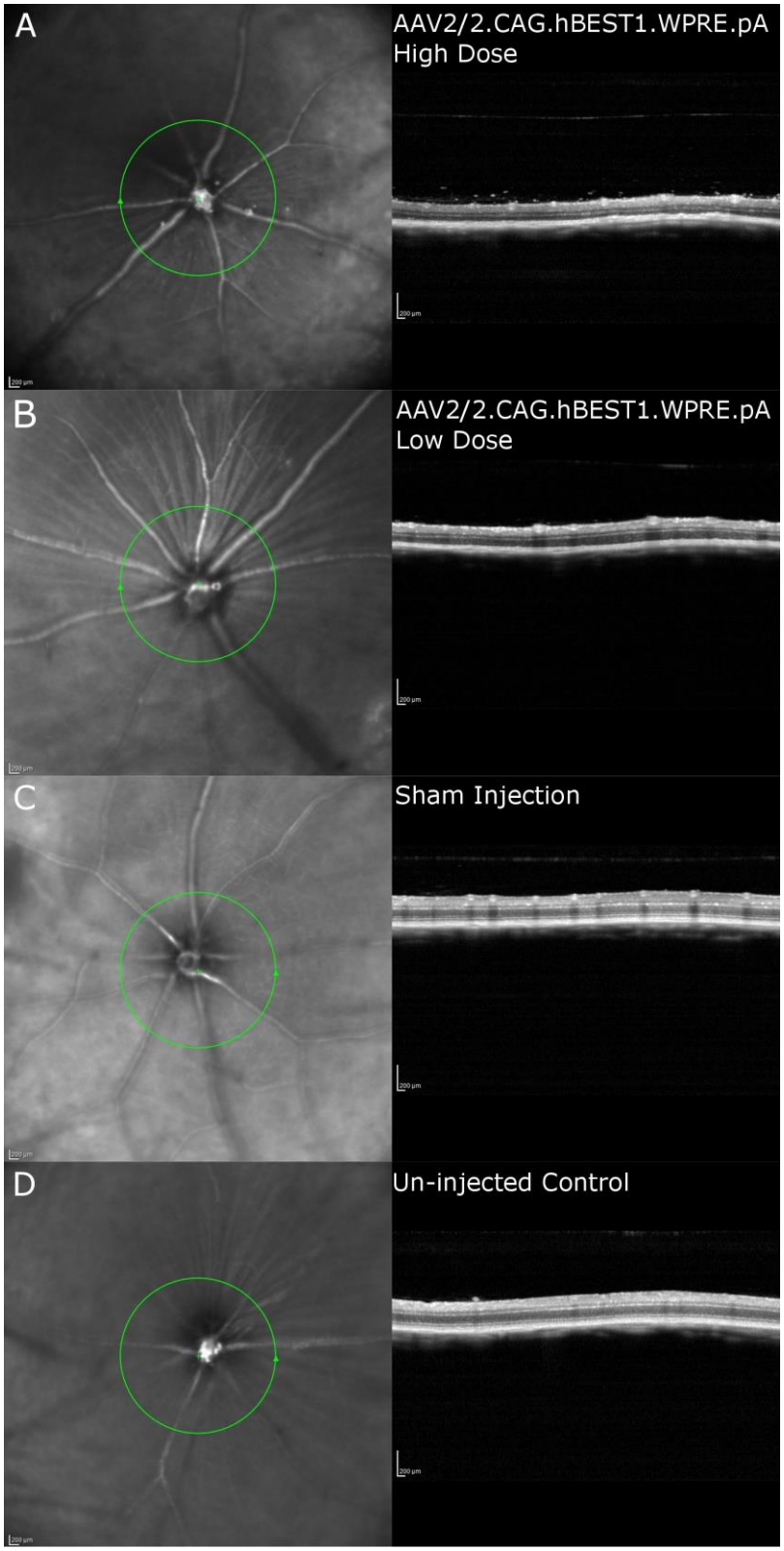

Figure 6.5. Optical Coherence Tomography Images of C57BL/6J Mice Injected AAV2/2.CAG.hBEST1.WPRE.pA. Representative OCT images of the retina from mice injected with high dose AAV2/2.CAG.hBEST1.WPRE.pA (**A**), low dose AAV2/2.CAG.hBEST1.WPRE.pA (**B**) and PBS+0.001%PF-68 (**C**). An uninjected retina is shown for camparison (**D**).

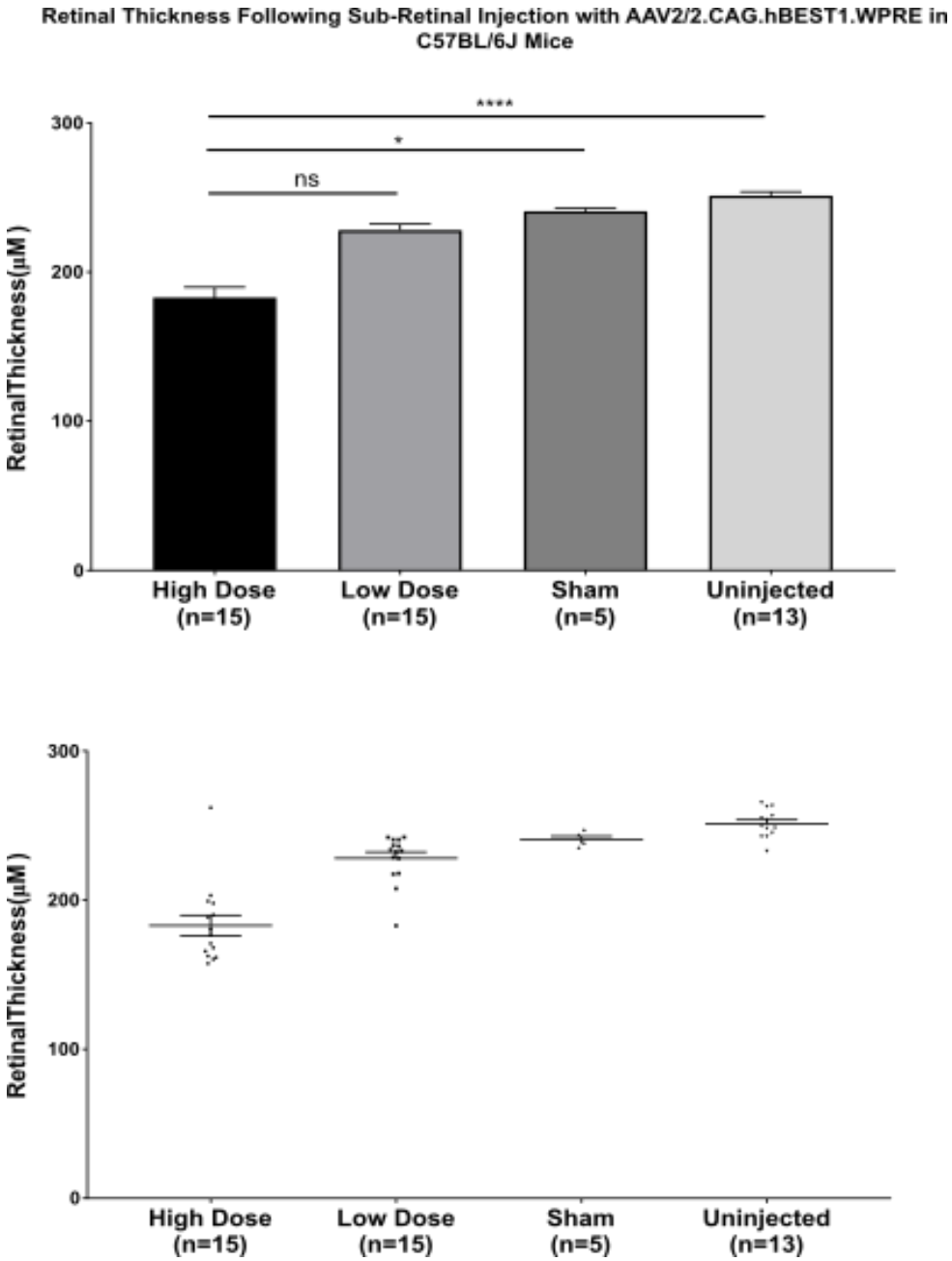

Figure 6.6. Retinal Thickness in C57BL6J Following Sub-Retinal Injection of AAV2/2.CAG.hBEST1.WPRE.pA. Average retinal thickness in eyes injected with a high dose of vector was 183 µm. This was thinner than low dose (average thickness = 228 µm) but not significant. High dose thinning was significant when compared against sham-injected (average thickness = 241 µM) and un-injected (average thickness = 251 µm). The range of the data indicated in B shows very little spread in high dose, low dose, sham and un-injected controls, with few outliers. Error bars indicate SEM. ****=$p<0.0001$, *=$p<0.05$).

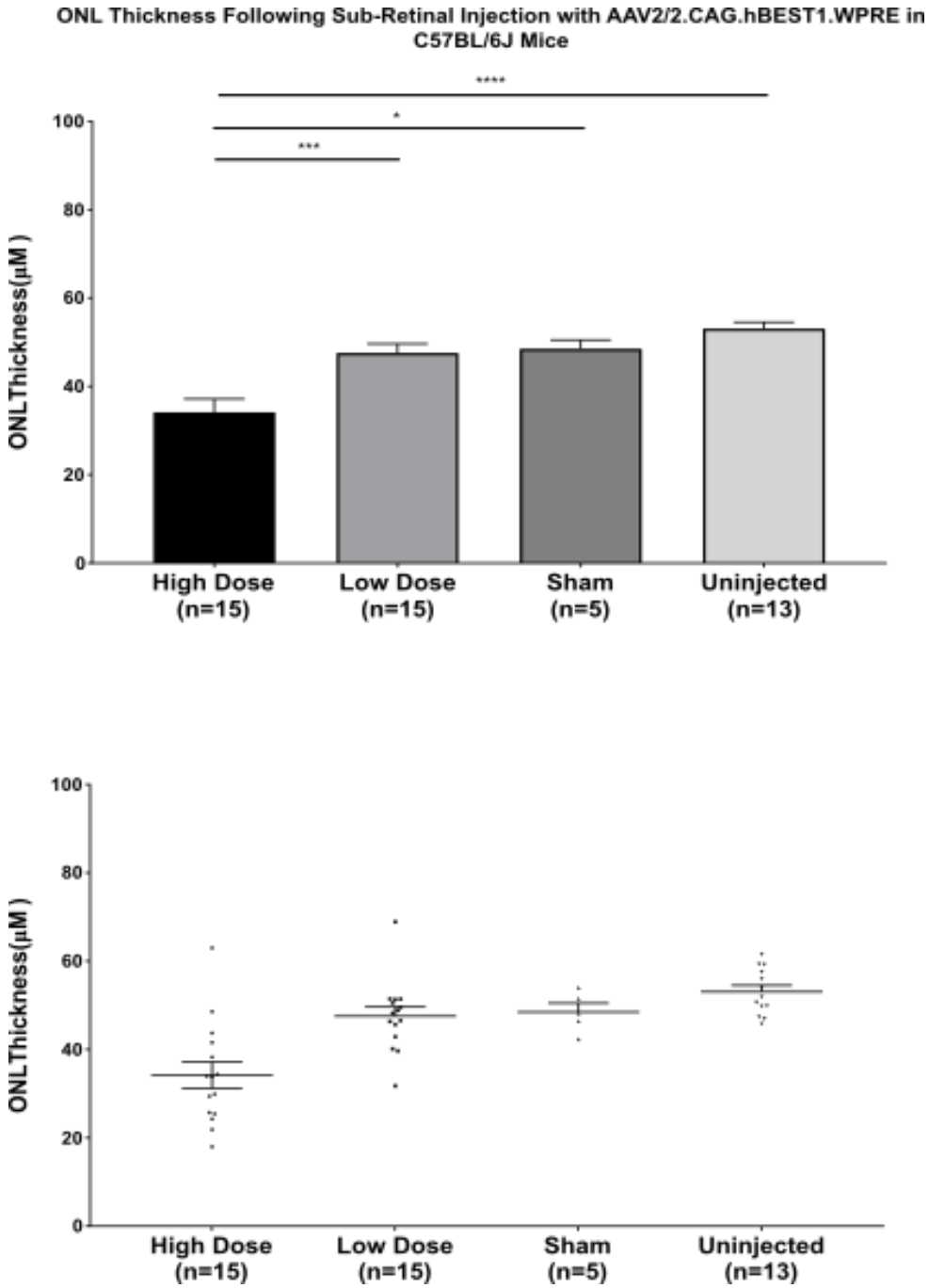

Figure 6.7. ONL Thickness in C57BL6J Following Sub-Retinal Injection of AAV2/2.CAG.hBEST1.WPRE.pA. Average ONL thickness in eyes injected with a high dose of vector was 34 µm. This was significantly thinner than low dose (average thickness = 47.55 µm), sham-injected (average thickness = 48.48 µM) and un-injected (average thickness = 53.08 µm). Error bars indicate SEM. ****=p<0.0001, ***=p<0.001, *=p<0.05).

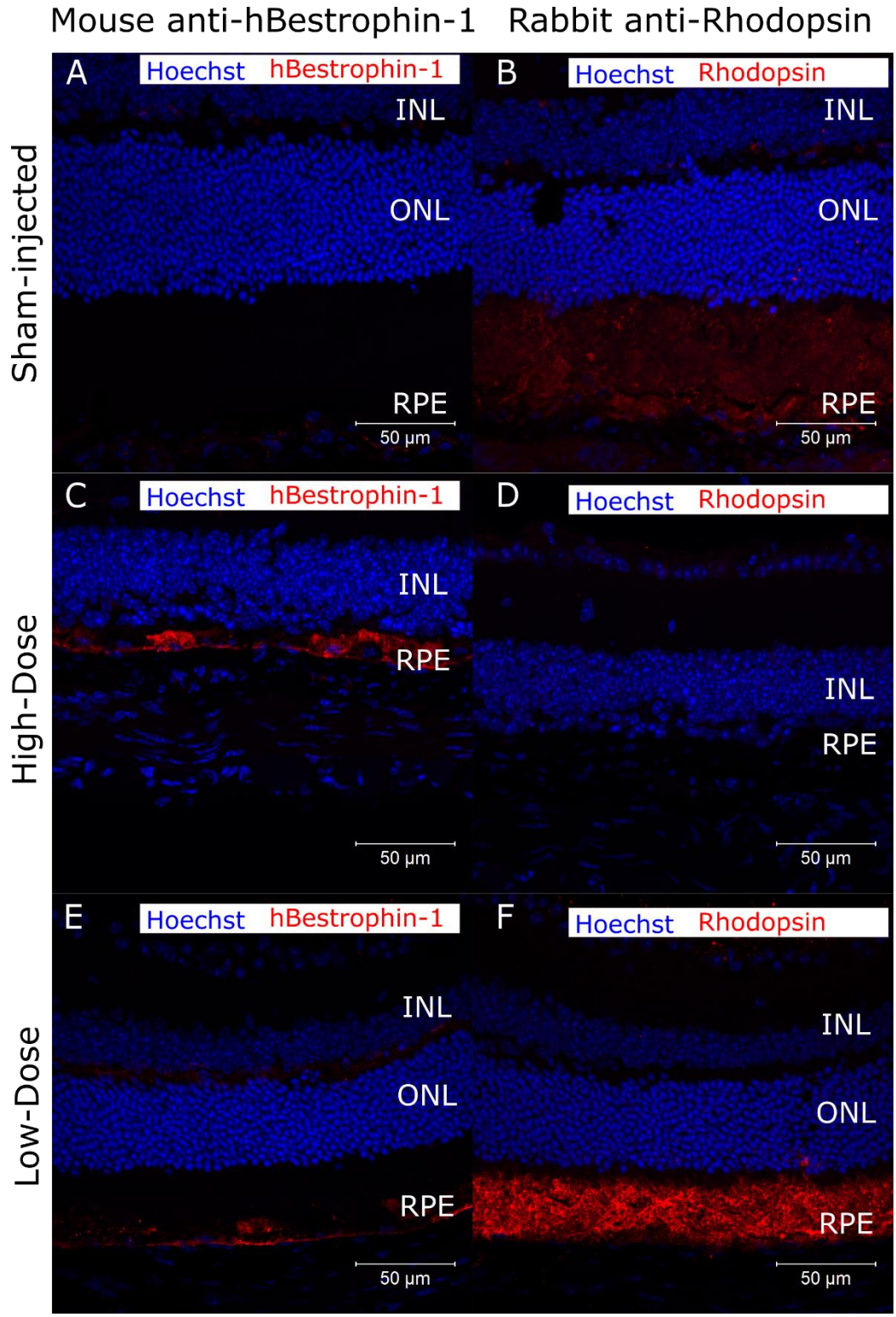
Mouse anti-hBestrophin-1
Rabbit anti-Rhodopsin
Sham-injected
High-Dose
Low-Dose
A
Hoechst hBestrophin-1
B
Hoechst Rhodopsin
C
Hoechst hBestrophin-1
D
Hoechst Rhodopsin
E
Hoechst hBestrophin-1
F
Hoechst Rhodopsin
INL
ONL
RPE
50 µm

Figure 6.8. Human Bestrophin-1 Expression in Murine Retina Following Injection of AAV2/2.CAG.hBEST1.WPRE.pA. Cyrosections from high dose and low dose eyes stained for Bestrophin-1 and Rhodopsin. No human Bestrophin-1 expression is detected in sham injected eyes (**A**) however mouse rhodopsin was detected (**B**). Bestrophin-1 was detected in the RPE of eyes injected with either high dose (**C**) or low doses of vector (**E**). No Rhodopsin is detected in the high dose eyes (**D**), however Rhodopsin is present in the low dose eyes (**F**). This expression is seen at the basolateral membrane in low dose eyes but is more diffuse throughout the cytosol in the high dose eyes. Rhodopsin was seen in the outer segments of animals injected with a low dose of vector but not in the high dose. Scale bars = 50 µM.

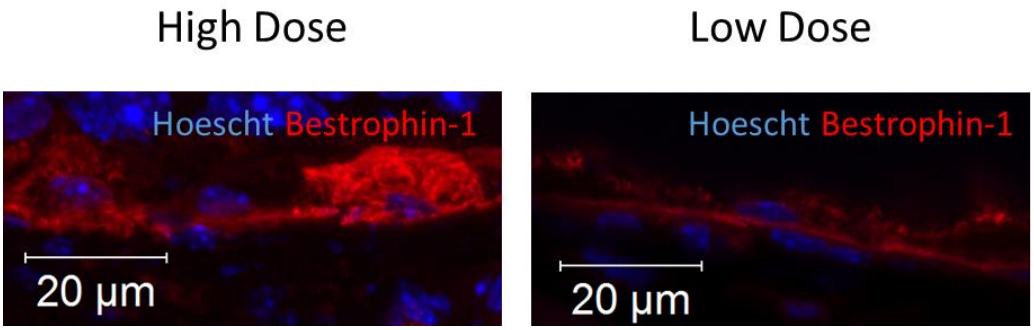

Figure 6.9. High-powered Confocal Images of the RPE in Injected Mice. Human bestrophin-1 is seen diffuse throughout the cytosol in the RPE following a high dose of vector. In low dose eyes, human bestrophin-1 is predominantly localised to the basolateral membrane of the RPE with some expression seen in the cytosol. Scale bars = 20 µM.

6.4 Chapter Discussion

Analysis of human bestrophin-1 in C57BL/6J mice *in vivo*, following sub-retinal injection of AAV2/2.CAG.hBEST1.WPRE.pA, shows detectable bestrophin-1 in the RPE. OCT analysis showed dose-dependent toxicity, with high doses of vector ($1.0x10^9$ vgp) giving significant retinal thinning when compared to sham injected controls. Lower doses of the vector ($1.0x10^8$ vgp) show no significant difference when compared to sham injected controls. In the ONL samples, the p-value for high-dose vs sham is lower than high-dose vs low-dose, which is probably due to a larger range of data points (as seen in figure 6.7) and the lower n-number of the sham group (n=5). Further experiments need to include more sham controls.

There are several possible mechanisms for the toxicity seen in this experiment. As bestrophin-1 functions as a chloride channel, it is possible that the expression of this protein in the wrong cells in the retina has a negative effect on cellular homeostasis. Although the level of bestrophin-1 expression in the neural retina is relatively low (figure 6.3), even low levels of expression could alter Cl^- conductance in the photoreceptors and cause ionic imbalances and abnormal water movement in the retina, leading to the death of the cells. Ca^{2+}-activated Cl^- channels in the photoreptors (including members of the anoctamin family) are known to be expressed at the synaptic terminal where they are thought to be involved in neurotransmitter release (*180*). The expression of bestrophin-1 could lead to abnormal regulation of this neurotransmitter release. As bestrophin-1 function appears to be redundant in mouse RPE (*73*), expressing human bestrophin-1 could provide an additional chloride conductance. This

could also cause perturbations in the homeostasis of the RPE and cause toxicity. If the AAV2/2.CAG.hBEST1.WPRE.pA construct was injected, sub-retinally, in an animal lacking the native chloride conductance associated with bestrophin-1 (e.g. the cmr dog), it is possible that this toxicity would not been seen. There is also the potential for the AAV capsid to cause toxicity, however AAV2/2 gene transfer to the RPE has been shown to be safe (*103*), therefore this is unlikely to be the case.

The toxicity seen raises issues with taking the vector forward to clinical trial and hence, future experiments with this vector should include dose escalation studies to determine the optimum dose that gives detectable bestrophin-1 expression while not causing significant toxicity to the retina. It may also be necessary to change the promoter included in the construct, limiting the expression to the RPE as well as removing the WPRE sequence. Further experiments should also look at the longevity of expression in the mouse eye. In this study, eyes were harvested at 4 weeks due to previous data suggesting that transgene expression from an AAV2/2 capsid could be expected to be high enough for analysis at this time point (*181*).

Chapter 7. Discussion

7.1 AAV-mediated Gene Therapy for ARB

Inherited retinal disorders are a major health concern across the western world, for which there are few available treatments. The prospect of using gene therapy to treat these conditions has gathered pace over the last decade or so. Clinical trials have been started across the world for inherited conditions such as Leber's Congenital Amaurosis (trials in London, UK [NCT00643747] and Philadelphia, USA), MERTK -associated retinitis pigmentosa (Saudi Arabia, Oxford) and Choroideremia (Oxford and London, UK) (*109, 110, 112, 113*). All the trials mentioned utilise an AAV vector, delivered via sub-retinal injection, to deliver the relevant transgene to the retina/RPE.

The bestrophinopathies are a class of inherited retinal disorders that are caused by mutations in the RPE-specific *BEST1* gene. Autosomal recessive bestrophinopathy (ARB) is thought to represent the *BEST1* null phenotype in humans and may be one of the next IRDs to be treated with gene therapy. The recessive nature of the condition lends itself to gene replacement, plus the retinal detachment that is characteristic of the condition may make a sub-retinal injection easier to perform with no need to detach the retina prior to surgery as with other gene therapy procedures (*110*). Furthermore, recent proof-of-principle for AAV-BEST1 transfer to the RPE in ARB has been demonstrated in the CMR dog model, by the Aguirre lab in Philadelphia, USA (*103*).

In this study we investigated the potential for gene therapy for ARB using a strong, ubiquitous ‘CAG’ promoter driving the expression of bestrophin-1, packaged into an AAV serotype 2 capsid. This differs from the approach mentioned above as Guziewicz

et al utilised the *VMD2* promoter to restrict expression to the RPE. Previous evidence suggests that cell-specific promoters elicit far less expression than the ubiquitous CAG promoter and may not be able to deliver enough transgene expression to alleviate the symptoms of ARB. Guziewicz et al do not show any functional correction in their paper, only correctly localised expression following sub-retinal injection. As of the time of writing no ERG or OCT data has been published on the use of BEST1 gene therapy *in vivo*.

In our study, the expression data that was obtained via western blot and immuno-cytochemistry shows that bestrophin-1 is delivered to human cells *in vitro* with AAV2/2.CAG.hBEST1.WPRE.pA and AAV2/2.CAG.hBEST1.pA and mouse RPE *in vivo* using AAV2/2.CAG.hBEST1.WPRE.pA. The inclusion of the WPRE element gives a significant increase in the expression of bestrophin-1, as seen in other studies analysing GFP expression following injection of AAV2/2.CAG.GFP.WPRE.pA (*172*). This, along with the strong expression from the CAG promoter could allow much lower doses of AAV to be delivered to the retina, reduced potential issues with vector-shedding and fewer humoral immune responses.

Whole-cell patch clamping show significant increases in chloride conductance in HEK293 cells transduced with AAV2/2.CAG.hBEST1.pA and AAV2/2.CAG.hBEST1.WPRE.pA compared to controls. Variation can be seen in the dot plots of the conductance which is probably due to the ‘blind’ patching approach that was taken. This could be overcome in future by the use of a reporter gene in the construct, under the control of an element such as an ‘IRES’ or ‘2A’ sequence. Both of

these would allow the separate translation of a reporter gene and the transgene. This approach wasn't undertaken here as the vectors were kept clear of elements that would not make it into the final, clinical grade vector that will go into future clinical trials. The differences in chloride conductance are consistent with previous functional studies of bestrophin-1 undertaken by other groups (*57, 59, 105*). The difference in expression and chloride conductance given by the inclusion of the WPRE meant that the AAV2/2.CAG.hBEST1.WPRE.pA vector was taken forward for further testing. Reduction of chloride in the external solution used to patch HEK293 cells, leads to a reduction in current amplitude and chloride conductance. This is also consistent with previous findings (*73*). To improve this study, it would be better to use RPE or RPE-like cells to show changes in chloride conductance *in vitro*. The most widely used RPE cell line is the ARPE19 line, an immortalized cell line from a 19 year-old male (*182*). These cells form a confluent, cobblestone monolayer when grown on transwell inserts. There are several limitations with this cell line, including a lack of pigmentation and a lack of expression of key RPE markers (such as RPE65 and BEST1) (*183*). Another option would be the use of primary cells harvested from an animal model of ARB. As already discussed in this thesis, the *Best*$^{-/-}$ mouse doesn't show significant retinal pathology and comparisons of primary RPE cultures from these mice versus wild-type mice showed no difference in chloride conductance as measured by whole-cell patch-clamping (*78*). Primary cultures of RPE from the CMR dog model would offer a much better model system, potentially allowing patch-clamping of RPE cultures from dogs injected with the AAV-BEST1 vectors. This would allow functional assessment of retinal function, via ERG, OCT and perhaps Scanning Laser Ophthalmoscope (SLO) coupled with in vitro electrophysiological data obtained via whole-cell patch-clamping.

In terms of clinical translational of these therapies, perhaps the most appropriate model system would be iPS-RPE derived from ARB patients. Recently, several groups have used iPS-RPE to model bestrophin-1 mutations and have shown reductions in chloride conductance when compared to iPS-RPE from unaffected controls (*73*). IPS-RPE derived from ARB patients also showed other deficiencies in POS phagocytosis, which could also be used as a test for the effectiveness of BEST1 gene therapy. The use of patient cells would give the most accurate in vitro model system and could even be used as a screening process to ascertain which patients would benefit from treatment, where patient cells are taken, reprogrammed, differentiated into RPE, transduced with vector and patch-clamped to test if the vector would give an improvement in visual outcome. In a condition that has a varying phenotypic presentation (like Best Disease) it is likely that some patients may benefit from gene replacement more than others. The identification of the optimal in vitro system will be vital if the patch-clamping studies described in this thesis are to be utilised as a GLP-compliant test for BEST1 gene therapy. To further improve the electrophysiology testing, the use of chloride-sensitive dyes to image the movement of chloride could be a powerful tool to confirm the results of the patch-clamping tests.

Sub-retinal injections of AAV2/2.CAG.hBEST1.WPRE.pA in C57BL/6J mice gave human bestrophin-1 expression that was detectable via western blot and IHC (figures 6.3 and 6.4). Expression was seen in RPE, which seemed to localise to the basolateral membrane, with some expression seen in the cytosol. This could be due to overexpression of the protein. Some expression was also detected in the retina, with

IHC suggesting that this could be in the photoreceptors (figure 6.2). A dose-comparison was performed with sub-retinal injections of a high dose ($1.0x10^9$ vgp) and a low dose of vector ($1.0x10^8$), along with a sham-injection of PBS+0.001% PF-68. OCT analysis of mice, 4 weeks post-injection, revealed significant retinal thinning in eyes injected with the high dose of vector. Low doses of the vector showed less retinal thinning and no significant difference with sham-injected controls. As sham injections show no significant retinal thinning compared to un-injected controls, it's unlikely that this toxicity is due to the surgery. All injections were done on the same day by an experienced surgeon in a mixed order, therefore toxicity is unlikely to be due to high dose injections being done earlier (when the surgeon is less practiced) then low dose or sham injections (when the surgeon is more practiced).

The overexpression of bestrophin-1 appears to be having a toxic effect on the retina. Analysis of the ONL thickness in these animals confirms the results of the retinal analysis and shows that it is the ONL that is degrading in mice injected with AAV2/2.CAG.hBEST1.WPRE.pA. This could be due to the expression of bestrophin-1 in the photoreceptors, altering cellular homeostasis and causing the cells to die. To analyse this further, a safety study using high, medium and low doses of the vector could be used with OCT and ERG analysis conducted at set time points over the course of 3-6 months. Due to the degree of retinal thinning seen in this study 4 weeks post-injection, OCT images and ERG recordings should be taken weekly from the day of injection until the end point.

Possible reasons for a degeneration of the retina include the aberrant expression of bestrophin-1 in the photoreceptors altering Cl^- movement and interfering with processes such as synaptic transmitter release. In particular, the Ca^{2+}-activated Cl^- channel anoctamin (also known as TMEM16B) seems to be involved in preventing the excessive release of neurotransmitters in scotopic conditions (*180, 184*). The introduction of a novel Ca^{2+}-activated Cl^- conductance in the rods could interfere with this process, perhaps leading to a complete ablation of transmitter release under scotopic conditions, or potentially reducing signalling upon the capture of a photon of light. This potential mechanism is described in figure 7.1.

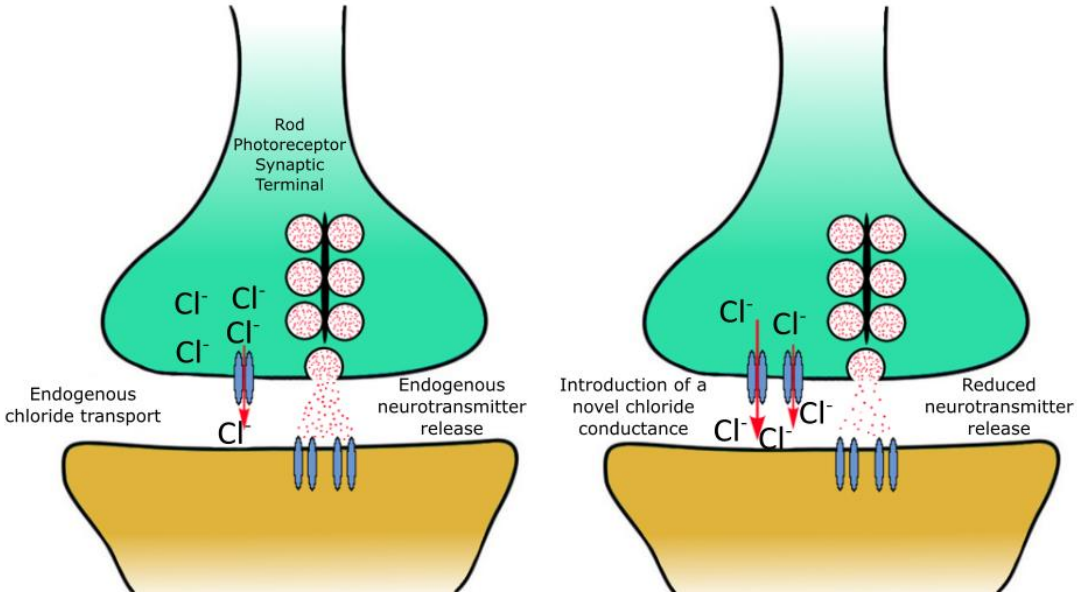

Figure 7.1. Possible mechanism of photoreceptor toxicity following sub-retinal injection of AAV-BEST1. Chloride channels at the synaptic terminal regulate the release of glutamate under scotopic conditions. The introduction of a novel chloride conductance via bestrophin-1 could disrupt this process.

To reduce retinal toxicity, a dose escalation study could be utilised, starting with injections of low doses of the vector and, once safety has been confirmed, increasing the dose to find the optimal level of vector. Another consideration is the AAV2/2.CAG.hBEST1.pA vector which, despite giving less expression than AAV2/2.CAG.hBEST1.WPRE.pA, showed significant increases in bestrophin-1 expression and chloride conductance compared to controls. To avoid retinal expression entirely, future experiments could use a vector that will give RPE-specific bestrophin-1 expression. This could involve using an RPE-specific promoter such as the VMD2 (*BEST1*) promoter (*185*) or the RPE65 promoter (which has been tested in clinical trials for LCA) (*113*). As cell-specific promoters often give less expression than ubiquitous promoters (such as CAG), an alternative approach could be to change the vector's viral capsid. AAV2/2 efficiently transduces the RPE but it also transduces the photoreceptors. AAV2/4 is known to have a higher specificity for the RPE so it may be an attractive alternative to AAV2/2 for *BEST1* gene therapy as it would allow for the use of the CAG promoter (*132*). Aforementioned studies in the *cmr1* dog have utilised the *VMD2* promoter with promising results.

There are, however, other possible explanations for the toxicity seen in this study. Expression of bestrophin-1 in the retina of a wild-type mouse would add an extra chloride conductance to those already present. As $Best^{-/-}$ mice show no changes in chloride conductance across the RPE when compared to $Best^{+/+}$ littermates (*78*), the function that bestrophin-1 performs in human RPE is performed by other channels in mouse RPE. Therefore the addition of a further chloride conductance could alter water movement across the retina and cause the death of the photoreceptors. The

overexpression of bestrophin-1 seen in the high dose eyes (figure 6.8) sees the bestrophin-1 protein diffuse throughout the cytosol rather than specifically localising to the cell membrane. Aberrant expression of bestrophin-1 could be causing the RPE to become unhealthy and lead to the secondary loss of the photoreceptors. If this is the case then the use of either an RPE-specific promoter or an RPE-specific AAV capsid would not reduce the toxicity seen. It is also possible that the natural regulation of bestrophin-1 expression in the RPE is overcome by the use of the CAG promoter. The use of the *VMD2* promoter may allow the RPE to regulate the expression more effectively and reduce toxicity. Toxicity may not have been seen if a more appropriate *Best1* knockout animal model (one that recapitulates the symptoms of ARB) was used.

A further explanation is that the chemicals used in the production of the virus could be present at high quantities in the injected viral suspension. Although the AAV suspensions were diluted to the appropriate quantities in PBS prior to injection, the high dose vector was diluted to a lesser extent than the low dose. Any contaminating reagents would, therefore, be present in greater quantities in the high dose viral suspension than the low dose, potentially explaining the difference in toxicity between the two. If this is the case, the toxicity seen would be limited to the immediate area around the injection site. As 2 µl of suspension was injected, more than half the retina was detached in these animals, therefore to analyse this, less suspension should be injected.

Before any clinical trial is considered, the AAV-BEST1 vectors must be tested in a suitable *in vivo* model. As previously discussed, *Best1*$^{-/-}$ mice show little retinal pathology and is, therefore, a poor model for *in vivo* testing. The *cmr* dogs are the only

in vivo model to date that would be suitable for testing the AAV-BEST1 vectors (*99*). The pathology of CMR mimics human ARB far more closely than the rodent models, including the characteristic retinal detachments and recessive inheritance pattern. ERG and OCT tests in treated and control dogs would allow a demonstration of the efficacy of BEST1 gene therapy. A recent paper describes a number of pathological changes in this dog model that could be used as clinical endpoints to test treatments, including impaired cone-associated microvillar ensheathment and compromised insoluble interphotoreceptor matrix (*104*)

Other potential options to take BEST1 gene therapy forward include the use of other gene transfer modalities, such as lentiviruses and non-viral gene transfer mechanisms as well as the use of self-complementary AAV vectors. Lentiviral vectors are unlikely to be of therapeutic use, due to the poor transfer efficiency in the retina (*40*). Non-viral transfer modalities currently show very poor transfer efficiency however, with improvements in technology, these vectors are consistently improving in this regard. The use of self-complementary AAV vectors could be a way of increasing transgene expression in the retina; however given the results of this study this may not be advisable unless the retinal toxicity is reduced by restricting expression to the RPE.

An interesting question that will need to be addressed in BEST1 gene therapy is when to administer the therapy to the patient. ARB is predominantly a juvenile onset condition, however this can be very variable (*47, 62*). As such, judging when best to intervene with the gene therapy treatment could be difficult. Also, determining which stage of the condition to target could also be difficult. Given the progressive nature of the condition,

the longer treatment is left, the more damage will be incurred to the retina/RPE, which may not be reversible. Early treatment, when the retina is still predominantly healthy and visual acuity is good, would probably be the most optimal approach. Given how difficult it is to diagnose ARB at the earliest stages (VA can be normal until the later stages so patients may not be seen by an ophthalmologist until the later stages of the condition), genetic testing for *BEST1* mutations will need to be performed in families with a history of the condition however, the recessive nature means the condition may not have appeared in the family for many generations and patients may not know that they need testing. Therefore, a large-scale genetic screening programme may need to be set-up to help identify patients, maybe as part of a screen of all genes associated with IRDs.

A final consideration for BEST1 gene therapy is whether or not the gene replacement strategy could help treat the dominant forms of the bestrophinopathies, BVMD, AVMD and ADVIRC. A gene replacement strategy for these conditions will depend on the mechanism of the dominant inheritance. If the disease phenotype is caused by toxic gain-of-function mutations in *BEST1* then it is unlikely that a gene replacement strategy will correct the condition. However, dominant phenotypes can also be caused by haploinsufficiency, where expression of both alleles is required for adequate protein function and therefore a mutation that leads to a reduction of expression in one of the alleles causes the levels of protein to drop below the amount required for function. If this is the case then the addition of a functional copy of *BEST1* could, theoretically, rescue the phenotype. Patch-clamp studies in HEK293 cells have shown no rescue of the dominant BVMD phenotype (*57*) suggesting that rescue cannot occur with gene

replacement. Furthermore, the *Best1*$^{-/-}$ mouse displays no disease phenotype whereas the *Best1*$^{+/W93C}$ mouse (knock-in of the dominant W93C mutation) displays a phenotype remarkably similar to BVMD in humans (*78*). This data suggests that W93C is a gain-of-function mutation and therefore would not be treatable with gene replacement therapy.

7.2 Alternatives to *BEST1* Gene Replacement Therapy

Although gene therapy is an attractive option for the treatment of *BEST1* mutations, there are other potential therapies in the pipeline that could also offer an answer. In recent years the concept of genome editing has gathered pace, particularly since CRISPR/Cas9 was first used to modify prokaryotic and eukaryotic cells in 2012 (*186, 187*). The use of genome editing technologies could, potentially, allow the *in vivo* repair of mutated genes in order to treat inherited disease. This is particularly exciting when we consider the treatment of dominantly inherited conditions, such as BVMD or ADVIRC, where gene replacement could be insufficient to alleviate symptoms (as already discussed).

As already discussed in this thesis, iPS-RPE derived from patients has produced an accurate in vitro model of Best disease; however it also has therapeutic potential itself. Recent clinical trials have looked at the transplantation of patient-derived iPS-RPE as a treatment for retinal degenerations such as AMD (*188*) However was suspended following the identification of mutations in the iPS-RPE lines (*189*) This could be particularly useful at the end stages of ARB and BVMD where it is possible that the

RPE may be too unhealthy to take up rAAV vectors or express the BEST1 transgene. It's possible that iPS-RPE cells from Best disease patients could be generated, the mutation corrected with CRISPR-Cas9 and the cells be transplanted back into patients.

A recent study by Uggenti et al demonstrated successful restoration of bestrophin-1 localisation and function using drugs designed to inhibit the proteasomal degradation of bestrophin-1 (*105*). The study showed that treatment of MDCKII cells, expressing mutant bestrophin-1, with 4-phenylbutyrate and bortezomib restored mutant bestrophin-1 localisation to the basolateral membrane. Whole-cell patch-clamping demonstrated restoration of anion conductance in HEK293 cells expressing bestrophin-1 that were also treated with these compounds. As both of these drugs are approved for use in other conditions they could make an attractive option for treatment; however it is likely that *in vivo* studies would be required to determine the best method of delivery and also whether or not the effects demonstrated are seen in animal models. Bortezomib can also cause severe side-effects when taken systemically, such as peripheral neuropathy and thrombocytopenia (*190, 191*).

7.3 Translation of Gene Therapy from the Lab Bench to the Clinic

Gene therapy has taken many years to go from initial concept through to being a viable treatment option for patients. The road has not always been smooth, initial clinical trials saw a large number of problems, many of which set the field of gene therapy back for decades (*192*). The worst of these included the death of a young male patient following an overdose of an adenoviral vector in a clinical trial in 1999 (*193*). Despite these early

problems, clinical trials in the field of gene therapy have gathered pace in the last few years. This thesis has already described several of these in the field of retinal gene therapy (summarised in table 14), however trials in other disease areas such as heart disease, liver disease, metabolic conditions and immune disorders are also being undertaken (*194-197*). The translation of these therapies requires the negotiation of a number of hurdles.

Condition	Gene	Clinical Trial Number
Leber Congenital Amaurosis (LCA)	*RPE65*	NCT01749957
		NCT00821340
		NCT00481546
		NCT00999609
		NCT00643747
		NCT00516477
		NCT01208389
MERTK-associated Retinitis Pigmentosa	*MERTK*	NCT01482195
X-linked Retinitis Pigmentosa	*RPGR*	NCT03116113
		NCT03252847
Stargardt's Macular Dystrophy	*ABCA4*	NCT01367444
Choroideremia	*CHM*	NCT01461213
		NCT02077361
Usher IB Syndrome	*MYO7A*	NCT01505062
AMD	*PEDF*	NCT00109499
	sFlt-1	NCT01024998
	Endostatin	NCT01301443
X-linked Retinoschisis	*RS1*	NCT02416622

Table 14. Clinical Trials in Retinal Gene Therapy.

One major consideration is the delivery of the chosen vector. In the context of retinal gene therapy, the vast majority of clinical trials have utilised a sub-retinal injection approach, depositing the vector between the photoreceptor layer and the RPE. An

obvious advantage of this is that the virus can be easily taken up into the photoreceptors and RPE, which are where the majority of the IRD's originate (*40*). However, sub-retinal injection requires the surgical detachment of the retina which can cause damage to the retina (*198, 199*) The alternative would be an intravitreal injection, which has the advantage of being less invasive than sub-retinal injection however is more likely to result in a humoral immune response and the presence of neutralising antibodies in the intraocular fluid (*200*). Improvements in the surgical delivery of the vector are currently under evaluation, for example the use of robots in vitreo-retinal surgery, to improve the precision of sub-retinal injections, is currently being trialled at the Oxford Eye Hospital (Clinical trial identifier: NCT03052881). Following injection of the therapy, it would also be useful to visualise the area under the retina in which the vector suspension extends, as well as indicating the presence of leakages which would decrease the amount of virus delivered to the retina. The inclusion of various dyes, which are already approved for clinical use, in the vector suspension could be trialled to achieve this. A recent study showed that including dyes such as Membrane Blue Dual, were well tolerated in the retina of wild-type C57BL/6 mice following sub-retinal injection, and also showed no effect on the ability of AAV2/2 to transduce the retina and RPE (*201*).

Gene therapy also has a number of potential safety concerns that have to be overcome before a viable treatment can be developed. In the context of rAAV-mediated gene therapy for IRDs, immunogenicity could be a potential issue. The eye is described as an 'immune privileged' environment, a scenario maintained by the blood-retina barrier and the presence of soluble immunosuppressive factors (*202*), however there remains a possibility that an immune response to the vector could be triggered if the vector

disseminates to the rest of the body. ‘Vector shedding’ therefore needs to be limited to prevent the production of neutralising antibodies. Sub-retinal injection has been shown to limit the vector to the injected region with very little shedding. A much larger amount of shedding occurs following intravitreal injection (*203*).

The delivery of accompanying drugs/small molecules to increase the effectiveness of AAV-mediated gene delivery and suppress the immune response is another important consideration in the translation of these therapies to the clinic. As already discussed, the eye benefits from ‘immune-privilege’ and, as such, the use of immunosuppressive drugs may not be required. However, given that there is a greater chance of ‘vector-shedding’ following intravitreal delivery of AAV, there is a possibility that the immune suppression would be required when using this strategy. As the AAV capsid is thought to be degraded by the proteasome following cellular entry, the use of proteosomal inhibitors, such as bortezomib and doxorubicin, may be useful to include in the vector suspension. This could allow for a lower dose of virus to be delivered that could avoid the issues seen in chapter 6 with regards to retinal toxicity. Modifications to the AAV capsids to improve transduction efficiency, such as tyrosine-mutants (*167*) could also allow a reduction in virus dose. Some studies also suggest that the use of exosomes in conjunction with AAV can improve gene transfer to the retina. The intravitreal injection of AAV2/2-GFP with and without the use of exosomes showed up to 4-fold increase in GFP expression as measured by fundus autofluoresence and mRNA analysis (*204*).

A major limitation in the field of gene therapy is the manufacturing of GMP-compliant viral vectors for use in clinical trials. At the time of writing, gene therapy is

predominantly University-led, with very few laboratories boasting the capability to produce GMP-compliant vector. In 2012, Innovate UK established the Cell and Gene Therapy Catapult in London to address this issue however, in 2017, academic laboratories, based in the UK, still have to rely on industrial partners to produce GMP vector (which can be expensive) or sourcing vector from overseas (from the EU and the USA, can be expensive and time-consuming).

7.4 Conclusions

The data presented here shows that AAV2/2-mediated transfer of *BEST1* gives detectable bestrophin-1 expression *in vitro* and *in vivo*. Chloride conductance is significantly increased in HEK293 cells *in vitro* compared to control cells, as measured by whole-cell patch-clamping. The inclusion of the WPRE significantly increases both protein expression and chloride conductance. *In vivo* studies showed that sub-retinal injection of AAV2/2.CAG.hBEST1.WPRE.pA in wild-type C57BL/6J mice gave detectable human bestrophin-1 in the RPE. However, there is also detectable human bestrophin-1 in the retina of injected mice. At high doses, the AAV2/2.CAG.hBEST1.WPRE.pA vector causes significant retinal thinning as seen on OCT. From this study we cannot conclude that the treatment of patients suffering from mutations in *BEST1* with an AAV-BEST1 vector will benefit those patients, however we demonstrate important first steps in that journey. There is, therefore, work left to do to prove the safety and efficacy of BEST1 gene therapy before this is a viable treatment option for patients suffering from ARB.

Chapter 8. References

1. **H. Kolb, in *Webvision: The Organization of the Retina and Visual System,* H. Kolb, E. Fernandez, R. Nelson, Eds. (University of Utah Health Sciences Center, Salt Lake City (UT), 1995).**
2. **C. S. McCaa, The eye and visual nervous system: anatomy, physiology and toxicology. *Environ Health Perspect* 44, 1 (Apr, 1982).**
3. **P. N. Bishop, Structural macromolecules and supramolecular organisation of the vitreous gel. *Prog Retin Eye Res* 19, 323 (May, 2000).**
4. **M. M. Le Goff, P. N. Bishop, Adult vitreous structure and postnatal changes. *Eye (Lond)* 22, 1214 (Oct, 2008).**
5. **P. D. Kiser, M. Golczak, A. Maeda, K. Palczewski, Key enzymes of the retinoid (visual) cycle in vertebrate retina. *Biochim Biophys Acta* 1821, 137 (Jan, 2012).**
6. **J. Nathans, The evolution and physiology of human color vision: insights from molecular genetic studies of visual pigments. *Neuron* 24, 299 (Oct, 1999).**
7. **H. Kolb, in *Webvision: The Organization of the Retina and Visual System,* H. Kolb, E. Fernandez, R. Nelson, Eds. (University of Utah Health Sciences Center, Salt Lake City (UT), 1995).**
8. **S. Beatty, H. Koh, M. Phil, D. Henson, M. Boulton, The role of oxidative stress in the pathogenesis of age-related macular degeneration. *Surv Ophthalmol* 45, 115 (2000 Sep-Oct, 2000).**
9. **S. C. Finnemann, R. L. Silverstein, Differential roles of CD36 and alphavbeta5 integrin in photoreceptor phagocytosis by the retinal pigment epithelium. *J Exp Med* 194, 1289 (Nov, 2001).**
10. **S. W. Ryeom, J. R. Sparrow, R. L. Silverstein, CD36 participates in the phagocytosis of rod outer segments by retinal pigment epithelium. *J Cell Sci* 109 (Pt 2), 387 (Feb, 1996).**
11. **S. C. Finnemann, V. L. Bonilha, A. D. Marmorstein, E. Rodriguez-Boulan, Phagocytosis of rod outer segments by retinal pigment epithelial cells requires alpha(v)beta5 integrin for binding but not for internalization. *Proc Natl Acad Sci U S A* 94, 12932 (Nov, 1997).**
12. **W. Feng, D. Yasumura, M. T. Matthes, M. M. LaVail, D. Vollrath, Mertk triggers uptake of photoreceptor outer segments during phagocytosis by cultured retinal pigment epithelial cells. *J Biol Chem* 277, 17016 (May, 2002).**

13. **A. Gal *et al.*, Mutations in MERTK, the human orthologue of the RCS rat retinal dystrophy gene, cause retinitis pigmentosa. *Nat Genet* 26, 270 (Nov, 2000).**

14. **E. F. Nandrot *et al.*, Loss of synchronized retinal phagocytosis and age-related blindness in mice lacking alphavbeta5 integrin. *J Exp Med* 200, 1539 (Dec, 2004).**

15. **M. Houssier *et al.*, CD36 deficiency leads to choroidal involution via COX2 down-regulation in rodents. *PLoS Med* 5, e39 (Feb, 2008).**

16. **R. Wen *et al.*, Injury-induced upregulation of bFGF and CNTF mRNAS in the rat retina. *J Neurosci* 15, 7377 (Nov, 1995).**

17. **W. Cao, R. Wen, F. Li, M. M. Lavail, R. H. Steinberg, Mechanical injury increases bFGF and CNTF mRNA expression in the mouse retina. *Exp Eye Res* 65, 241 (Aug, 1997).**

18. **W. Cao *et al.*, In vivo protection of photoreceptors from light damage by pigment epithelium-derived factor. *Invest Ophthalmol Vis Sci* 42, 1646 (Jun, 2001).**

19. **M. S. Burns, M. J. Hartz, The retinal pigment epithelium induces fenestration of endothelial cells in vivo. *Curr Eye Res* 11, 863 (Sep, 1992).**

20. **J. P. Alexander, J. M. Bradley, J. D. Gabourel, T. S. Acott, Expression of matrix metalloproteinases and inhibitor by human retinal pigment epithelium. *Invest Ophthalmol Vis Sci* 31, 2520 (Dec, 1990).**

21. **P. Ahuja *et al.*, Lens epithelium-derived growth factor (LEDGF) delays photoreceptor degeneration in explants of rd/rd mouse retina. *Neuroreport* 12, 2951 (Sep, 2001).**

22. **L. J. Relvas *et al.*, Extracellular nucleotides and interleukin-8 production by ARPE cells: potential role of danger signals in blood-retinal barrier activation. *Invest Ophthalmol Vis Sci* 50, 1241 (Mar, 2009).**

23. **Y. H. Kim *et al.*, Regulated secretion of complement factor H by RPE and its role in RPE migration. *Graefes Arch Clin Exp Ophthalmol* 247, 651 (May, 2009).**

24. **B. A. Austin, B. Liu, Z. Li, R. B. Nussenblatt, Biologically active fibronectin fragments stimulate release of MCP-1 and catabolic cytokines from murine retinal pigment epithelium. *Invest Ophthalmol Vis Sci* 50, 2896 (Jun, 2009).**

25. **O. Strauss, The retinal pigment epithelium in visual function. *Physiol Rev* 85, 845 (Jul, 2005).**

26. **Y. Ban, L. J. Rizzolo, Regulation of glucose transporters during development of the retinal pigment epithelium. *Brain Res Dev Brain Res* 121, 89 (May, 2000).**

27. **N. G. Bazan, W. C. Gordon, E. B. Rodriguez de Turco, Docosahexaenoic acid uptake and metabolism in photoreceptors: retinal conservation by an efficient retinal pigment epithelial cell-mediated recycling process. *Adv Exp Med Biol* 318, 295 (1992).**

28. **B. A. Pfeffer, V. M. Clark, J. G. Flannery, D. Bok, Membrane receptors for retinol-binding protein in cultured human retinal pigment epithelium. *Invest Ophthalmol Vis Sci* 27, 1031 (Jul, 1986).**

29. **M. F. Marmor, Control of subretinal fluid: experimental and clinical studies. *Eye (Lond)* 4 (Pt 2), 340 (1990).**

30. **A. D. Marmorstein, The polarity of the retinal pigment epithelium. *Traffic* 2, 867 (Dec, 2001).**

31. **J. S. Adorante, S. S. Miller, Potassium-dependent volume regulation in retinal pigment epithelium is mediated by Na,K,Cl cotransport. *J Gen Physiol* 96, 1153 (Dec, 1990).**

32. **M. R. Bösl *et al.*, Male germ cells and photoreceptors, both dependent on close cell-cell interactions, degenerate upon ClC-2 Cl(-) channel disruption. *EMBO J* 20, 1289 (Mar, 2001).**

33. **S. Blaug, R. Quinn, J. Quong, S. Jalickee, S. S. Miller, Retinal pigment epithelial function: a role for CFTR? *Doc Ophthalmol* 106, 43 (Jan, 2003).**

34. **H. C. Hartzell, Z. Qu, K. Yu, Q. Xiao, L. T. Chien, Molecular physiology of bestrophins: multifunctional membrane proteins linked to best disease and other retinopathies. *Physiol Rev* 88, 639 (Apr, 2008).**

35. **J. Adijanto, T. Banzon, S. Jalickee, N. S. Wang, S. S. Miller, CO2-induced ion and fluid transport in human retinal pigment epithelium. *J Gen Physiol* 133, 603 (Jun, 2009).**

36. **R. H. Steinberg, Interactions between the retinal pigment epithelium and the neural retina. *Doc Ophthalmol* 60, 327 (Oct, 1985).**

37. **R. H. Steinberg, R. A. Linsenmeier, E. R. Griff, Three light-evoked responses of the retinal pigment epithelium. *Vision Res* 23, 1315 (1983).**

38. **B. Huang, C. J. Karwoski, Light-evoked expansion of subretinal space volume in the retina of the frog. *J Neurosci* 12, 4243 (Nov, 1992).**

39. **E. Kenyon, A. Maminishkis, D. P. Joseph, S. S. Miller, Apical and basolateral membrane mechanisms that regulate pHi in bovine retinal pigment epithelium. *Am J Physiol* 273, C456 (Aug, 1997).**

40. **M. E. McClements, R. E. MacLaren, Gene therapy for retinal disease. *Transl Res* 161, 241 (Apr, 2013).**

41. **S. Veleri *et al.*, Biology and therapy of inherited retinal degenerative disease: insights from mouse models. *Dis Model Mech* 8, 109 (Feb, 2015).**

42. **A. Rattner, H. Sun, J. Nathans, Molecular genetics of human retinal disease. *Annu Rev Genet* 33, 89 (1999).**

43. **M. M. Hims, S. P. Diager, C. F. Inglehearn, Retinitis pigmentosa: genes, proteins and prospects. *Dev Ophthalmol* 37, 109 (2003).**

44. **B. M. Nash, D. C. Wright, J. R. Grigg, B. Bennetts, R. V. Jamieson, Retinal dystrophies, genomic applications in diagnosis and prospects for therapy. *Transl Pediatr* 4, 139 (Apr, 2015).**

45. **A. Marquardt *et al.*, Mutations in a novel gene, VMD2, encoding a protein of unknown properties cause juvenile-onset vitelliform macular dystrophy (Best's disease). *Human Molecular Genetics* 7, 1517 (Sep, 1998).**

46. **K. Petrukhin *et al.*, Identification of the gene responsible for Best macular dystrophy. *Nat Genet* 19, 241 (Jul, 1998).**

47. **C. J. Boon *et al.*, The spectrum of ocular phenotypes caused by mutations in the BEST1 gene. *Prog Retin Eye Res* 28, 187 (May, 2009).**

48. **R. Clemett, Vitelliform dystrophy: long-term observations on New Zealand pedigrees. *Australian and New Zealand journal of ophthalmology* 19, 221 (Aug, 1991).**

49. **R. Arora *et al.*, Unilateral BEST1-Associated Retinopathy. *Am J Ophthalmol* 169, 24 (Sep, 2016).**

50. **S. J. Kaufman *et al.*, Autosomal dominant vitreoretinochoroidopathy. *Arch Ophthalmol* 100, 272 (Feb, 1982).**

51. **J. Yardley *et al.*, Mutations of VMD2 splicing regulators cause nanophthalmos and autosomal dominant vitreoretinochoroidopathy (ADVIRC). *Invest Ophthalmol Vis Sci* 45, 3683 (Oct, 2004).**

52. **A. Vincent, C. McAlister, C. Vandenhoven, E. Héon, BEST1-related autosomal dominant vitreoretinochoroidopathy: a degenerative disease with a range of developmental ocular anomalies.** ***Eye (Lond)*** **25, 113 (Jan, 2011).**

53. **R. Burgess *et al.*, ADVIRC is caused by distinct mutations in BEST1 that alter pre-mRNA splicing.** ***J Med Genet*** **46, 620 (Sep, 2009).**

54. **D. A. Carter *et al.*, Mislocalisation of BEST1 in iPSC-derived retinal pigment epithelial cells from a family with autosomal dominant vitreoretinochoroidopathy (ADVIRC).** ***Sci Rep*** **6, 33792 (Sep, 2016).**

55. **U. Kellner, C. Jandeck, H. Kraus, M. H. Foerster, Autosomal dominant vitreoretinochoroidopathy with normal electrooculogram in a German family.** ***Graefes Arch Clin Exp Ophthalmol*** **236, 109 (Feb, 1998).**

56. **R. F. Mullins, M. H. Kuehn, E. A. Faidley, N. A. Syed, E. M. Stone, Differential macular and peripheral expression of bestrophin in human eyes and its implication for best disease.** ***Invest Ophthalmol Vis Sci*** **48, 3372 (Jul, 2007).**

57. **R. Burgess *et al.*, Biallelic mutation of BEST1 causes a distinct retinopathy in humans.** ***American Journal of Human Genetics*** **82, 19 (Jan, 2008).**

58. **R. N. Hussain, F. L. Shahid, T. Empeslidis, S. W. Ch'ng, Use of Intravitreal Bevacizumab in a 9-Year-Old Child with Choroidal Neovascularization Associated with Autosomal Recessive Bestrophinopathy.** ***Ophthalmic genetics*** **36, 265 (2015).**

59. **A. E. Davidson *et al.*, Functional Characterization of Bestrophin-1 Missense Mutations Associated with Autosomal Recessive Bestrophinopathy.** ***Investigative Ophthalmology & Visual Science*** **52, 3730 (May, 2011).**

60. **A. E. Davidson *et al.*, A synonymous codon variant in two patients with autosomal recessive bestrophinopathy alters in vitro splicing of BEST1.** ***Mol Vis*** **16, 2916 (Dec, 2010).**

61. **C. J. Boon *et al.*, Autosomal recessive bestrophinopathy: differential diagnosis and treatment options.** ***Ophthalmology*** **120, 809 (Apr, 2013).**

62. **A. A. Johnson *et al.*, Bestrophin 1 and retinal disease.** ***Prog Retin Eye Res*****, (Jan, 2017).**

63. **A. E. Davidson *et al.*, Missense mutations in a retinal pigment epithelium protein, bestrophin-1, cause retinitis pigmentosa.** ***Am J Hum Genet*** **85, 581 (Nov, 2009).**

64. **L. A. Dalvin *et al.*, Retinitis pigmentosa associated with a mutation in BEST1. *American journal of ophthalmology case reports* 2, 11 (Jul, 2016).**

65. **H. Sun, T. Tsunenari, K. W. Yau, J. Nathans, The vitelliform macular dystrophy protein defines a new family of chloride channels. *Proceedings of the National Academy of Sciences of the United States of America* 99, 4008 (Mar, 2002).**

66. **V. M. Milenkovic, T. Langmann, R. Schreiber, K. Kunzelmann, B. H. Weber, Molecular evolution and functional divergence of the bestrophin protein family. *BMC Evol Biol* 8, 72 (Feb, 2008).**

67. **V. Kane Dickson, L. Pedi, S. B. Long, Structure and insights into the function of a Ca(2+)-activated Cl(-) channel. *Nature* 516, 213 (Dec, 2014).**

68. **T. Yang *et al.*, Structure and selectivity in bestrophin ion channels. *Science* 346, 355 (Oct, 2014).**

69. **V. Kane Dickson, Phasing and structure of bestrophin-1: a case study in the use of heavy-atom cluster compounds with multi-subunit transmembrane proteins. *Acta crystallographica. Section D, Structural biology* 72, 319 (Mar, 2016).**

70. **H. Stöhr, A. Marquardt, I. Nanda, M. Schmid, B. H. Weber, Three novel human VMD2-like genes are members of the evolutionary highly conserved RFP-TM family. *Eur J Hum Genet* 10, 281 (Apr, 2002).**

71. **K. Mladenova *et al.*, Effects of Ca2+ ions on bestrophin-1 surface films. *Colloids and surfaces. B, Biointerfaces* 149, 226 (Jan 01, 2017).**

72. **J. B. Stanton, A. F. Goldberg, G. Hoppe, L. Y. Marmorstein, A. D. Marmorstein, Hydrodynamic properties of porcine bestrophin-1 in Triton X-100. *Biochim Biophys Acta* 1758, 241 (Feb, 2006).**

73. **A. Milenkovic *et al.*, Bestrophin 1 is indispensable for volume regulation in human retinal pigment epithelium cells. *Proc Natl Acad Sci U S A* 112, E2630 (May, 2015).**

74. **Y. Moshfegh *et al.*, BESTROPHIN1 mutations cause defective chloride conductance in patient stem cell-derived RPE. *Hum Mol Genet* 25, 2672 (Jul, 2016).**

75. **A. D. Marmorstein *et al.*, Bestrophin-1 influences transepithelial electrical properties and Ca2+ signaling in human retinal pigment epithelium. *Mol Vis* 21, 347 (2015).**

76. **K. Yu, Q. Xiao, G. Cui, A. Lee, H. C. Hartzell, The best disease-linked Cl- channel hBest1 regulates Ca V 1 (L-type) Ca2+ channels via src-homology-binding domains. *J Neurosci* 28, 5660 (May, 2008).**

77. **N. Reichhart, V. M. Milenkovic, C. A. Halsband, S. Cordeiro, O. Strauss, Effect of bestrophin-1 on L-type Ca2+ channel activity depends on the Ca2+ channel beta-subunit. *Exp Eye Res* 91, 630 (Nov, 2010).**

78. **L. Y. Marmorstein *et al.*, The light peak of the electroretinogram is dependent on voltage-gated calcium channels and antagonized by bestrophin (best-1). *J Gen Physiol* 127, 577 (May, 2006).**

79. **Y. Zhang *et al.*, Suppression of Ca2+ signaling in a mouse model of Best disease. *Hum Mol Genet* 19, 1108 (Mar, 2010).**

80. **R. Singh *et al.*, iPS cell modeling of Best disease: insights into the pathophysiology of an inherited macular degeneration. *Hum Mol Genet* 22, 593 (Feb, 2013).**

81. **V. M. Milenkovic, A. Rivera, F. Horling, B. H. Weber, Insertion and topology of normal and mutant bestrophin-1 in the endoplasmic reticulum membrane. *J Biol Chem* 282, 1313 (Jan, 2007).**

82. **K. Yu, Z. Qu, Y. Cui, H. C. Hartzell, Chloride channel activity of bestrophin mutants associated with mild or late-onset macular degeneration. *Invest Ophthalmol Vis Sci* 48, 4694 (Oct, 2007).**

83. **R. Rosenthal *et al.*, Expression of bestrophin-1, the product of the VMD2 gene, modulates voltage-dependent Ca2+ channels in retinal pigment epithelial cells. *FASEB J* 20, 178 (Jan, 2006).**

84. **D. Marchant *et al.*, New VMD2 gene mutations identified in patients affected by Best vitelliform macular dystrophy. *J Med Genet* 44, e70 (Mar, 2007).**

85. **D. Marchant *et al.*, Identification of novel VMD2 gene mutations in patients with best vitelliform macular dystrophy. *Hum Mutat* 17, 235 (Mar, 2001).**

86. **V. M. Milenkovic, E. Rohrl, B. H. Weber, O. Strauss, Disease-associated missense mutations in bestrophin-1 affect cellular trafficking and anion conductance. *J Cell Sci* 124, 2988 (Sep 1, 2011).**

87. **A. A. Johnson *et al.*, Differential effects of Best disease causing missense mutations on bestrophin-1 trafficking. *Hum Mol Genet* 22, 4688 (Dec 1, 2013).**

88. **A. A. Johnson *et al.*, Disease-causing mutations associated with four bestrophinopathies exhibit disparate effects on the localization, but not the oligomerization, of Bestrophin-1. *Exp Eye Res* 121, 74 (Apr, 2014).**

89. **A. A. Johnson *et al.*, Autosomal Recessive Bestrophinopathy Is Not Associated With the Loss of Bestrophin-1 Anion Channel Function in a Patient With a Novel BEST1 Mutation. *Invest Ophthalmol Vis Sci* 56, 4619 (Jul, 2015).**

90. **L. Y. Marmorstein *et al.*, Bestrophin interacts physically and functionally with protein phosphatase 2A. *J Biol Chem* 277, 30591 (Aug, 2002).**

91. **S. Lee *et al.*, Channel-mediated tonic GABA release from glia. *Science* 330, 790 (Nov, 2010).**

92. **D. H. Woo *et al.*, TREK-1 and Best1 channels mediate fast and slow glutamate release in astrocytes upon GPCR activation. *Cell* 151, 25 (Sep 28, 2012).**

93. **H. Park *et al.*, Bestrophin-1 encodes for the Ca2+-activated anion channel in hippocampal astrocytes. *J Neurosci* 29, 13063 (Oct, 2009).**

94. **S. Jo *et al.*, GABA from reactive astrocytes impairs memory in mouse models of Alzheimer's disease. *Nat Med* 20, 886 (Aug, 2014).**

95. **M. Boudes *et al.*, Best1 is a gene regulated by nerve injury and required for Ca2+-activated Cl- current expression in axotomized sensory neurons. *J Neurosci* 29, 10063 (Aug, 2009).**

96. **M. Boudes, F. Scamps, Calcium-activated chloride current expression in axotomized sensory neurons: what for? *Front Mol Neurosci* 5, 35 (2012).**

97. **B. Bakall *et al.*, Expression and localization of bestrophin during normal mouse development. *Invest Ophthalmol Vis Sci* 44, 3622 (Aug, 2003).**

98. **A. D. Marmorstein *et al.*, A model of best vitelliform macular dystrophy in rats. *Invest Ophthalmol Vis Sci* 45, 3733 (Oct, 2004).**

99. **K. E. Guziewicz *et al.*, Bestrophin gene mutations cause canine multifocal retinopathy: a novel animal model for best disease. *Invest Ophthalmol Vis Sci* 48, 1959 (May, 2007).**

100. **B. Zangerl *et al.*, Assessment of canine BEST1 variations identifies new mutations and establishes an independent bestrophinopathy model (cmr3). *Mol Vis* 16, 2791 (2010).**

101. **I. Hoffmann, K. E. Guziewicz, B. Zangerl, G. D. Aguirre, C. Y. Mardin, Canine multifocal retinopathy in the Australian Shepherd: a case report. *Vet Ophthalmol* 15 Suppl 2, 134 (Sep, 2012).**

102. **W. A. Beltran *et al.*, Canine retina has a primate fovea-like bouquet of cone photoreceptors which is affected by inherited macular degenerations. *PLoS One* 9, e90390 (2014).**

103. **K. E. Guziewicz *et al.*, Recombinant AAV-mediated BEST1 transfer to the retinal pigment epithelium: analysis of serotype-dependent retinal effects. *PLoS One* 8, e75666 (2013).**

104. **K. E. Guziewicz *et al.*, Bestrophinopathy: An RPE-photoreceptor interface disease. *Prog Retin Eye Res* 58, 70 (May, 2017).**

105. **C. Uggenti *et al.*, Restoration of mutant bestrophin-1 expression, localisation and function in a polarised epithelial cell model. *Dis Model Mech* 9, 1317 (Nov, 2016).**

106. **R. Singh *et al.*, Pharmacological Modulation of Photoreceptor Outer Segment Degradation in a Human iPS Cell Model of Inherited Macular Degeneration. *Mol Ther* 23, 1700 (Nov, 2015).**

107. **R. G. Knowlton *et al.*, A polymorphic DNA marker linked to cystic fibrosis is located on chromosome 7. *Nature* 318, 380 (1985 Nov 28-Dec 4, 1985).**

108. **J. M. Rommens *et al.*, Identification of the cystic fibrosis gene: chromosome walking and jumping. *Science* 245, 1059 (Sep, 1989).**

109. **A. M. Maguire *et al.*, Safety and efficacy of gene transfer for Leber's congenital amaurosis. *N Engl J Med* 358, 2240 (May, 2008).**

110. **R. E. Maclaren *et al.*, Retinal gene therapy in patients with choroideremia: initial findings from a phase 1/2 clinical trial. *Lancet*, (Jan, 2014).**

111. **T. L. Edwards *et al.*, Visual Acuity after Retinal Gene Therapy for Choroideremia. *N Engl J Med* 374, 1996 (May, 2016).**

112. **N. G. Ghazi *et al.*, Treatment of retinitis pigmentosa due to MERTK mutations by ocular subretinal injection of adeno-associated virus gene vector: results of a phase I trial. *Hum Genet* 135, 327 (Mar, 2016).**

113. **J. W. Bainbridge *et al.*, Long-term effect of gene therapy on Leber's congenital amaurosis. *N Engl J Med* 372, 1887 (May, 2015).**

114. **A. Georgiadis *et al.*, Development of an optimized AAV2/5 gene therapy vector for Leber congenital amaurosis owing to defects in RPE65. *Gene Ther* 23, 857 (Dec, 2016).**

115. **R. G. Weleber *et al.*, Results at 2 Years after Gene Therapy for RPE65-Deficient Leber Congenital Amaurosis and Severe Early-Childhood-Onset Retinal Dystrophy. *Ophthalmology* 123, 1606 (Jul, 2016).**

116. **F. Simonelli *et al.*, Gene therapy for Leber's congenital amaurosis is safe and effective through 1.5 years after vector administration. *Mol Ther* 18, 643 (Mar, 2010).**

117. **J. Bennett *et al.*, Safety and durability of effect of contralateral-eye administration of AAV2 gene therapy in patients with childhood-onset blindness caused by RPE65 mutations: a follow-on phase 1 trial. *Lancet* 388, 661 (Aug, 2016).**

118. **M. D. Fischer *et al.*, Codon-Optimized RPGR Improves Stability and Efficacy of AAV8 Gene Therapy in Two Mouse Models of X-Linked Retinitis Pigmentosa. *Mol Ther* 25, 1854 (Aug, 2017).**

119. **W. A. Beltran *et al.*, Optimization of Retinal Gene Therapy for X-Linked Retinitis Pigmentosa Due to RPGR Mutations. *Mol Ther* 25, 1866 (Aug 2, 2017).**

120. **I. J. Constable *et al.*, Phase 2a Randomized Clinical Trial: Safety and Post Hoc Analysis of Subretinal rAAV.sFLT-1 for Wet Age-related Macular Degeneration. *EBioMedicine* 14, 168 (Dec, 2016).**

121. **R. R. Ali *et al.*, Gene transfer into the mouse retina mediated by an adeno-associated viral vector. *Hum Mol Genet* 5, 591 (May, 1996).**

122. **R. W. ATCHISON, B. C. CASTO, W. M. HAMMON, ADENOVIRUS-ASSOCIATED DEFECTIVE VIRUS PARTICLES. *Science* 149, 754 (Aug, 1965).**

123. **M. A. Goncalves, Adeno-associated virus: from defective virus to effective vector. *Virology journal* 2, 43 (May 06, 2005).**

124. **A. Pfeifer, I. M. Verma, Gene therapy: promises and problems. *Annual review of genomics and human genetics* 2, 177 (2001).**

125. **C. McClure, K. L. Cole, P. Wulff, M. Klugmann, A. J. Murray, Production and titering of recombinant adeno-associated viral vectors. *Journal of visualized experiments : JoVE*, e3348 (Nov 27, 2011).**

126. **E. M. Surace, A. Auricchio, Versatility of AAV vectors for retinal gene transfer. *Vision Res* 48, 353 (Feb, 2008).**

127. **L. Y. Huang, S. Halder, M. Agbandje-McKenna, Parvovirus glycan interactions. *Curr Opin Virol* 7, 108 (Aug, 2014).**

128. **J. S. Bartlett, R. Wilcher, R. J. Samulski, Infectious entry pathway of adeno-associated virus and adeno-associated virus vectors. *J Virol* 74, 2777 (Mar, 2000).**

129. **M. Nonnenmacher, T. Weber, Adeno-associated virus 2 infection requires endocytosis through the CLIC/GEEC pathway. *Cell Host Microbe* 10, 563 (Dec, 2011).**

130. **S. Pillay *et al.*, An essential receptor for adeno-associated virus infection. *Nature* 530, 108 (Feb, 2016).**

131. **C. Lebherz, A. Maguire, W. Tang, J. Bennett, J. M. Wilson, Novel AAV serotypes for improved ocular gene transfer. *J Gene Med* 10, 375 (Apr, 2008).**

132. **M. Weber *et al.*, Recombinant adeno-associated virus serotype 4 mediates unique and exclusive long-term transduction of retinal pigmented epithelium in rat, dog, and nonhuman primate after subretinal delivery. *Mol Ther* 7, 774 (Jun, 2003).**

133. **G. S. Yang *et al.*, Virus-mediated transduction of murine retina with adeno-associated virus: effects of viral capsid and genome size. *J Virol* 76, 7651 (Aug, 2002).**

134. **M. Agbandje-McKenna, J. Kleinschmidt, AAV capsid structure and cell interactions. *Methods Mol Biol* 807, 47 (2011).**

135. **H. Petrs-Silva *et al.*, High-efficiency transduction of the mouse retina by tyrosine-mutant AAV serotype vectors. *Mol Ther* 17, 463 (Mar, 2009).**

136. **M. M. Doroudchi *et al.*, Virally delivered channelrhodopsin-2 safely and effectively restores visual function in multiple mouse models of blindness. *Mol Ther* 19, 1220 (Jul, 2011).**

137. **L. Zhong *et al.*, Next generation of adeno-associated virus 2 vectors: point mutations in tyrosines lead to high-efficiency transduction at lower doses. *Proc Natl Acad Sci U S A* 105, 7827 (Jun, 2008).**

138. **S. R. De Silva *et al.*, Single residue AAV capsid mutation improves transduction of photoreceptors in the Abca4(-/-) mouse and bipolar cells in the rd1 mouse and human retina ex vivo. *Gene Ther* 23, 767 (Nov, 2016).**

139. **K. J. Fisher *et al.*, Transduction with recombinant adeno-associated virus for gene therapy is limited by leading-strand synthesis. *J Virol* 70, 520 (Jan, 1996).**

140. **K. Yokoi *et al.*, Ocular gene transfer with self-complementary AAV vectors. *Invest Ophthalmol Vis Sci* 48, 3324 (Jul, 2007).**

141. **M. Natkunarajah *et al.*, Assessment of ocular transduction using single-stranded and self-complementary recombinant adeno-associated virus serotype 2/8. *Gene Ther* 15, 463 (Mar, 2008).**

142. **G. C. Pien *et al.*, Capsid antigen presentation flags human hepatocytes for destruction after transduction by adeno-associated viral vectors. *J Clin Invest* 119, 1688 (Jun, 2009).**

143. **J. Zhu, X. Huang, Y. Yang, The TLR9-MyD88 pathway is critical for adaptive immune responses to adeno-associated virus gene therapy vectors in mice. *J Clin Invest* 119, 2388 (Aug, 2009).**

144. **G. L. Rogers *et al.*, Innate Immune Responses to AAV Vectors. *Front Microbiol* 2, 194 (2011).**

145. **M. Inaba, E. Toninelli, G. Vanmeter, J. R. Bender, M. S. Conte, Retroviral gene transfer: Effects on endothelial cell phenotype. *Journal of Surgical Research* 78, 31 (Jul, 1998).**

146. **D. Trono, Lentiviral vectors: turning a deadly foe into a therapeutic agent. *Gene Therapy* 7, 20 (Jan, 2000).**

147. **J. Kong *et al.*, Correction of the disease phenotype in the mouse model of Stargardt disease by lentiviral gene therapy. *Gene Ther* 15, 1311 (Oct, 2008).**

148. **W. P. ROWE, R. J. HUEBNER, L. K. GILMORE, R. H. PARROTT, T. G. WARD, Isolation of a cytopathogenic agent from human adenoids undergoing spontaneous degeneration in tissue culture. *Proc Soc Exp Biol Med* 84, 570 (Dec, 1953).**

149. **M. J. Havenga *et al.*, Exploiting the natural diversity in adenovirus tropism for therapy and prevention of disease. *J Virol* 76, 4612 (May, 2002).**

150. **F. Kreppel, T. T. Luther, I. Semkova, U. Schraermeyer, S. Kochanek, Long-term transgene expression in the RPE after gene transfer with a high-capacity adenoviral vector. *Invest Ophthalmol Vis Sci* 43, 1965 (Jun, 2002).**

151. **A. Puppo *et al.*, Retinal transduction profiles by high-capacity viral vectors. *Gene Ther* 21, 855 (Oct, 2014).**

152. **R. Hendrickx *et al.*, Innate immunity to adenovirus. *Hum Gene Ther* 25, 265 (Apr, 2014).**

153. **S. A. Harvey, E. G. Romanowski, K. A. Yates, Y. J. Gordon, Adenovirus-directed ocular innate immunity: the role of conjunctival defensin-like chemokines (IP-10, I-TAC) and phagocytic human defensin-alpha. *Invest Ophthalmol Vis Sci* 46, 3657 (Oct, 2005).**

154. **S. M. Cashman, J. Gracias, M. Adhi, R. Kumar-Singh, Adenovirus-mediated delivery of Factor H attenuates complement C3 induced pathology in the murine retina: a potential gene therapy for age-related macular degeneration. *J Gene Med* 17, 229 (Oct-Dec, 2015).**

155. **Y. S. Bee *et al.*, Gene Delivery of Calreticulin Anti-Angiogenic Domain Attenuates the Development of Choroidal Neovascularization in Rats. *Hum Gene Ther* 28, 403 (May, 2017).**

156. **S. Kachi *et al.*, Nonviral ocular gene transfer. *Gene Ther* 12, 843 (May, 2005).**

157. **H. W. Liao, K. W. Yau, In vivo gene delivery in the retina using polyethylenimine. *Biotechniques* 42, 285 (Mar, 2007).**

158. **T. Matsuda, C. L. Cepko, Analysis of gene function in the retina. *Methods Mol Biol* 423, 259 (2008).**

159. **A. V. Oliveira, A. M. Rosa da Costa, G. A. Silva, Non-viral strategies for ocular gene delivery. *Mater Sci Eng C Mater Biol Appl* 77, 1275 (Aug, 2017).**

160. **A. Sharma *et al.*, Polyethylenimine-conjugated gold nanoparticles: Gene transfer potential and low toxicity in the cornea. *Nanomedicine* 7, 505 (Aug, 2011).**

161. **C. A. Grant, S. Ponnazhagan, X. S. Wang, A. Srivastava, T. Li, Evaluation of recombinant adeno-associated virus as a gene transfer vector for the retina. *Curr Eye Res* 16, 949 (Sep, 1997).**

162. **J. A. Sawicki, R. J. Morris, B. Monks, K. Sakai, J. Miyazaki, A composite CMV-IE enhancer/beta-actin promoter is ubiquitously expressed in mouse cutaneous epithelium. *Exp Cell Res* 244, 367 (Oct, 1998).**

163. **J. E. Olsson *et al.*, Transgenic mice with a rhodopsin mutation (Pro23His): a mouse model of autosomal dominant retinitis pigmentosa. *Neuron* 9, 815 (Nov, 1992).**

164. **S. E. Boye *et al.*, The human rhodopsin kinase promoter in an AAV5 vector confers rod- and cone-specific expression in the primate retina. *Hum Gene Ther* 23, 1101 (Oct, 2012).**

165. **Q. Li, A. M. Timmers, J. Guy, J. Pang, W. W. Hauswirth, Cone-specific expression using a human red opsin promoter in recombinant AAV. *Vision Res* 48, 332 (Feb, 2008).**

166. **G. Le Meur *et al.*, Restoration of vision in RPE65-deficient Briard dogs using an AAV serotype 4 vector that specifically targets the retinal pigmented epithelium. *Gene Ther* 14, 292 (Feb, 2007).**

167. **R. C. Ryals, S. L. Boye, A. Dinculescu, W. W. Hauswirth, S. E. Boye, Quantifying transduction efficiencies of unmodified and tyrosine capsid mutant AAV vectors in vitro using two ocular cell lines. *Mol Vis* 17, 1090 (Apr, 2011).**

168. **M. H. Tan *et al.*, Gene therapy for retinitis pigmentosa and Leber congenital amaurosis caused by defects in AIPL1: effective rescue of mouse models of partial and complete Aipl1 deficiency using AAV2/2 and AAV2/8 vectors. *Hum Mol Genet* 18, 2099 (Jun, 2009).**

169. **X. Sun *et al.*, Gene therapy with a promoter targeting both rods and cones rescues retinal degeneration caused by AIPL1 mutations. *Gene Ther* 17, 117 (Jan, 2010).**

170. **S. E. Boye *et al.*, Functional and behavioral restoration of vision by gene therapy in the guanylate cyclase-1 (GC1) knockout mouse. *PLoS One* 5, e11306 (Jun, 2010).**

171. **B. S. Pawlyk *et al.*, Replacement gene therapy with a human RPGRIP1 sequence slows photoreceptor degeneration in a murine model of Leber congenital amaurosis. *Hum Gene Ther* 21, 993 (Aug, 2010).**

172. **M. I. Patrício, A. R. Barnard, H. O. Orlans, M. E. McClements, R. E. MacLaren, Inclusion of the Woodchuck Hepatitis Virus Posttranscriptional Regulatory Element Enhances AAV2-Driven Transduction of Mouse and Human Retina. *Mol Ther Nucleic Acids* 6, 198 (Mar, 2017).**

173. **N. Fertig, R. H. Blick, J. C. Behrends, Whole cell patch clamp recording performed on a planar glass chip. *Biophysical journal* 82, 3056 (Jun, 2002).**

174. **P. Thomas, T. G. Smart, HEK293 cell line: a vehicle for the expression of recombinant proteins. *J Pharmacol Toxicol Methods* 51, 187 (2005 May-Jun, 2005).**

175. **M. M. White, M. Aylwin, Niflumic and flufenamic acids are potent reversible blockers of Ca2(+)-activated Cl- channels in Xenopus oocytes. *Molecular pharmacology* 37, 720 (May, 1990).**

176. **M. Manea, G. Mezo, F. Hudecz, M. Przybylski, Mass spectrometric identification of the trypsin cleavage pathway in lysyl-proline containing oligotuftsin peptides. *J Pept Sci* 13, 227 (Apr, 2007).**

177. **L. Tsiatsiani, A. J. Heck, Proteomics beyond trypsin. *FEBS J* 282, 2612 (Jul, 2015).**

178. **Y. Bian *et al.*, Improve the coverage for the analysis of phosphoproteome of HeLa cells by a tandem digestion approach. *J Proteome Res* 11, 2828 (May, 2012).**

179. **P. Giansanti, L. Tsiatsiani, T. Y. Low, A. J. Heck, Six alternative proteases for mass spectrometry-based proteomics beyond trypsin. *Nat Protoc* 11, 993 (May, 2016).**

180. **K. Dauner, C. Möbus, S. Frings, F. Möhrlen, Targeted expression of anoctamin calcium-activated chloride channels in rod photoreceptor terminals of the rodent retina. *Invest Ophthalmol Vis Sci* 54, 3126 (May, 2013).**

181. **M. I. Patricio, A. R. Barnard, H. O. Orlans, M. E. McClements, R. E. MacLaren, Inclusion of the Woodchuck Hepatitis Virus Posttranscriptional Regulatory Element Enhances AAV2-Driven Transduction of Mouse and Human Retina. *Mol Ther Nucleic Acids* 6, 198 (Mar 17, 2017).**

182. **K. C. Dunn, A. E. Aotaki-Keen, F. R. Putkey, L. M. Hjelmeland, ARPE-19, a human retinal pigment epithelial cell line with differentiated properties. *Exp Eye Res* 62, 155 (Feb, 1996).**

183. **A. Ahmado *et al.*, Induction of differentiation by pyruvate and DMEM in the human retinal pigment epithelium cell line ARPE-19. *Invest Ophthalmol Vis Sci* 52, 7148 (2011).**

184. **W. B. Thoreson, E. J. Bryson, K. Rabl, Reciprocal interactions between calcium and chloride in rod photoreceptors. *J Neurophysiol* 90, 1747 (Sep, 2003).**

185. **N. Esumi, Y. Oshima, Y. Y. Li, P. A. Campochiaro, D. J. Zack, Analysis of the VMD2 promoter and implication of E-box binding factors in its regulation. *Journal of Biological Chemistry* 279, 19064 (Apr, 2004).**

186. **M. Jinek *et al.*, A programmable dual-RNA-guided DNA endonuclease in adaptive bacterial immunity. *Science* 337, 816 (Aug, 2012).**

187. **L. Cong *et al.*, Multiplex genome engineering using CRISPR/Cas systems. *Science* 339, 819 (Feb, 2013).**

188. **M. Yoshihara, Y. Hayashizaki, Y. Murakawa, Genomic Instability of iPSCs: Challenges Towards Their Clinical Applications. *Stem Cell Rev* 13, 7 (Feb, 2017).**

189. **K. Garber, RIKEN suspends first clinical trial involving induced pluripotent stem cells. *Nat Biotechnol* 33, 890 (Sep, 2015).**

190. **A. A. Argyriou, G. Iconomou, H. P. Kalofonos, Bortezomib-induced peripheral neuropathy in multiple myeloma: a comprehensive review of the literature. *Blood* 112, 1593 (Sep, 2008).**

191. **K. Murai *et al.*, Bortezomib induces thrombocytopenia by the inhibition of proplatelet formation of megakaryocytes. *Eur J Haematol* 93, 290 (Oct, 2014).**

192. **M. A. Kotterman, T. W. Chalberg, D. V. Schaffer, Viral Vectors for Gene Therapy: Translational and Clinical Outlook. *Annual review of biomedical engineering* 17, 63 (2015).**

193. **J. M. Wilson, Lessons learned from the gene therapy trial for ornithine transcarbamylase deficiency. *Molecular genetics and metabolism* 96, 151 (Apr, 2009).**

194. **M. Jessup *et al.*, Calcium Upregulation by Percutaneous Administration of Gene Therapy in Cardiac Disease (CUPID) A Phase 2 Trial of Intracoronary Gene Therapy of Sarcoplasmic Reticulum Ca2+-ATPase in Patients With Advanced Heart Failure. *Circulation* 124, 304 (Jul, 2011).**

195. **A. Biffi *et al.*, Lentiviral hematopoietic stem cell gene therapy benefits metachromatic leukodystrophy. *Science* 341, 1233158 (Aug 23, 2013).**

196. **L. M. Kattenhorn *et al.*, Adeno-Associated Virus Gene Therapy for Liver Disease. *Hum Gene Ther* 27, 947 (Dec, 2016).**

197. **H. B. Gaspar *et al.*, Hematopoietic stem cell gene therapy for adenosine deaminase-deficient severe combined immunodeficiency leads to long-term immunological recovery and metabolic correction. *Sci Transl Med* 3, 97ra80 (Aug, 2011).**

198. **B. Cook, G. P. Lewis, S. K. Fisher, R. Adler, Apoptotic photoreceptor degeneration in experimental retinal detachment. *Invest Ophthalmol Vis Sci* 36, 990 (May, 1995).**

199. **T. Igarashi *et al.*, Direct comparison of administration routes for AAV8-mediated ocular gene therapy. *Curr Eye Res* 38, 569 (May, 2013).**

200. **Q. Li *et al.*, Intraocular route of AAV2 vector administration defines humoral immune response and therapeutic potential. *Mol Vis* 14, 1760 (Sep, 2008).**

201. **A. P. Salvetti *et al.*, Impact of Vital Dyes on Cell Viability and Transduction Efficiency of AAV Vectors Used in Retinal Gene Therapy Surgery: An In Vitro and In Vivo Analysis. *Translational vision science & technology* 6, 4 (Jul, 2017).**

202. **R. Zhou, R. R. Caspi, Ocular immune privilege. *F1000 Biol Rep* 2, (Jan, 2010).**

203. **G. A. Ochakovski, K. U. Bartz-Schmidt, M. D. Fischer, Retinal Gene Therapy: Surgical Vector Delivery in the Translation to Clinical Trials. *Front Neurosci* 11, 174 (2017).**

204. **B. Gyorgy, C. A. Maguire, Extracellular vesicles: nature's nanoparticles for improving gene transfer with adeno-associated virus vectors. *Wiley interdisciplinary reviews. Nanomedicine and nanobiotechnology*, (Aug 11, 2017).**